Study of QGP and Its Properties Using Correlation and Fluctuation Phenomena in Ultra-Relativistic High Energy Collision

Joyati Mondal

Thesis submitted for the award of

Degree of Doctor of Philosophy (Science)

Jadavpur University, 2025

Nuclear and Particle Physics Research Centre

CERTIFICATE FROM THE SUPERVISORS

This is to certify that the thesis entitled "**Study of QGP and Its Properties Using Correlation and Fluctuation Phenomena in Ultra-Relativistic High Energy Collision**" submitted by **Joyati Mondal** who got her name registered on February 5, 2018 for the award of Ph.D. (Science) degree of Jadavpur University, is absolutely based upon her own work under the supervision of **Prof. Mitali Mondal**, Professor, Department of Physics, Jadavpur University and **Dr. Premomoy Ghosh**, Former Scientific Officer, Variable Energy Cyclotron Centre, Kolkata and that neither this thesis nor any part of it has been submitted for either any degree/diploma or any other academic award anywhere before.

PROFESSOR MITALI MONDAL
Department of Physics
Jadavpur University
Kolkata – 700 032

1..... 10.07.2025

2..... 10.07.2025

DEPARTMENT OF PHYSICS JADAVPUR UNIVERSITY KOLKATA INDIA
PHONE: 033-2457 2538 email: npprc@jadavpuruniversity.in

To my beloved son Arinjay

and in loving memory of my grandfather

Gouranga Prasad Singha

There are two possible outcomes: if the result confirms the hypothesis, then you've made a measurement. If the result is contrary to the hypothesis, then you've made a discovery.

--- Enrico Fermi

Acknowledgements

I would like to express my deepest gratitude to my supervisor Prof. Mitali Mondal for her constant guidance and encouragement throughout the course of my research. Her timely responses, thoughtful feedback and steady mentorship have played a vital role in shaping the progress and quality of my work. She has always been approachable and supportive; even beyond academic guidance, she motivated me during difficult times and helped me to become a better version of myself. I truly consider it a privilege to have worked under her supervision. I would like to express my deepest respect to my supervisor Dr. Premomoy Ghosh. He has provided me proper guidance and training throughout my research work. He has been very meticulous and critical about my progress of work and specially presentations. It not only improved the quality of my research but also sharpened my scientific communication skill.

I am profoundly grateful to Prof. Argha Deb, whose valuable discussions have enriched my research work. His consistent encouragement and kind guidance have been with me from the very beginning of this journey. I deeply appreciate his involvement and the positive impact he has had on both my academic and personal growth. I would like to express my sincere respect to Prof. Dipak Ghosh. As the senior-most member of our group, his vast experience and thoughtful perspective have consistently inspired me to pursue quality research.

I would like to convey my earnest and wholehearted thanks to Mr. Prasanta Kundu**,** whose academic guidance inspired and greatly influenced my early understanding of science. I am especially grateful to late Dr. Soumya Sundar Bhattacharya, who holds a special place in my life as an elder brother, teacher and philosopher. He was the one who first inspired me to join research work. In his short life, his words and presence always gave me the mental strength I needed, and his absence is deeply felt. I would also like to express respect and gratitude to all my school and college teachers for their guidance, which has enabled me to reach this stage.

I sincerely thank the members of my Research Advisory Committee, the faculty members and staff who have supported me throughout my Ph.D. journey.

I gratefully acknowledge the Department of Science and Technology (DST), India for providing the fellowship under the INSPIRE scheme.

I would like to acknowledge the support of my seniors Dr. Soma Ghosh, Dr. Javed Akhtar, Dr. Arindam Mondal, Dr. Somnath Kar, Mr. Mahasin Gazi and my juniors Shreya, Jessica, Abhijeet. I would also like to thank my senior Dr. Subikash Choudhury for his timely and positive assistance during the final phase of my work. I heartily appreciate the enthusiastic cooperation of my junior Mr. Hirak Kumar Koley throughout this journey. I would like to thank all my research colleagues, seniors, and juniors for making this journey both insightful and enjoyable. I also extend my warm thanks to my research colleague Dr. Saheli Chowdhury, whose encouragement and help in the early years had a significant impact on my journey.

I would like to thank my optimistic childhood friends, Mrs. Priti Bidyanta and Mrs. Poushali Kundu, whose encouraging words uplifted me especially during the unfavorable times of my PhD tenure. A special thanks to Rintu Kundu, my neighbor and more than a sister, whose unwavering presence and constant care have made her an irreplaceable part of my life. I feel truly blessed to have had so many wonderful people by my side. Though I cannot mention everyone here, I deeply appreciate all the well-wishers, seniors, friends, and relatives who supported me throughout this journey.

I must mention Mrs. Tulika Das, my neighbor and the constant caregiver of my son, whose steady support was an immense help, especially during the final phase of this journey. The genuine love and affection she and her family have shown toward my son mean a lot to me. Without their help, it would have been difficult to reach the point where I could complete this thesis and acknowledge all those who have supported me along the way. I would like to thank them from the bottom of my heart and will always remember their kindness whenever I revisit this work.

I would like to express my deepest love and gratitude to my parents, Mr. Jagadish Chandra Mondal and Mrs. Arpita Mondal, for everything. My heartfelt thanks to my niece Debashruti, whose smile always lifted my spirits. I would especially like to remember my late grandfather, Mr. Gouranga Prasad Singha, who always believed in me and gave me strength. Sadly, he is not here to witness this milestone and appreciate my achievement. I would also like to express my gratitude to my parents-in-law.

I would like to express my heartfelt thanks to my dear husband Dr. Arindam Kumar Naskar for his constant reassurance, patience and understanding throughout this period. I am truly grateful for his financial support during the final two years of my thesis work.

I am immensely grateful to my little son, Arinjay, who has been a constant source of joy in my life. Even before he turned two, he would cheer me on with the words, 'Maa, boi likho, ami babar kache ghumabo' (Mother, write the book, I will sleep beside Baba). Though after an hour or two, he would still need me by his side to fall asleep, I deeply cherish and acknowledge his innocent yet meaningful sacrifice.

Lastly, I extend my heartfelt gratitude to nature, whose serene beauty and quiet strength nurtured my well-being and offered solace during the most challenging moments of this journey.

Joyati Mondal
10.07.2025

JULY, 2025

JOYATI MONDAL

List of Publications

Publications in Peer-reviewed Journal

1. "Chaos in multiparticle production in ^{16}O-AgBr interactions at 60 A GeV and its target excitation dependence"
   Authors: **Joyati Mondal**, H. K. Koley, J. Ghatak, A. Deb and M. Mondal
   Published journal: The European Physical Journal Plus, **139**, 960 (2024).

2. "Forward-backward multiplicity and momentum correlations in pp and pPb collisions at the LHC energies"
   Authors: **Joyati Mondal**, H. Koley, S. Kar, P. Ghosh, A. Deb and M. Mondal
   Published journal: Physical Review D **107**, 114016 (2023).

3. "Forward-backward multiplicity and momentum correlations in pp collisions at LHC energies"
   Authors: Mitali Mondal, **Joyati Mondal**, S. Kar, A. Deb and P. Ghosh
   Published journal: Physical Review D **102**, 014033 (2020).

4. "Evidence of centrality dependent fractal behaviour in high energy heavy ion interactions: Hint of two different sources"
   Authors: M. Mondal, A. Mondal, **Joyati Mondal**, K. Patra, A. Deb, D. Ghosh
   Published journal: Chaos Solitons and Fractals **113**, 230-237 (2018).

Publication in Conference Proceedings

1. "Study of Forward-Backward Correlations in Small Collision Systems at the LHC Energies Using a Strongly Intensive Observable"
   Authors: **Joyati Mondal**, H. Koley, S. Kar, A. Deb and M. Mondal
   Proceedings of the DAE Symp. on Nucl. Phys. 66 (2022) 1020-1021
   Contribution to: 66th DAE Symposium on nuclear physics, 1-5 Dec 2022, Guwahati, India

Conference Presentations

1. "Forward-backward multiplicity and momentum correlations in proton-lead collisions at the LHC energy: A model based study"
   Authors: **Joyati Mondal**, H. Koley, S. Kar, A. Deb and M. Mondal
   Poster presentation at Contemporary and Emerging Topics in High Energy Nuclear Physics (CETHENP-2022), 15-17 November 2022, Variable Energy Cyclotron Centre, Kolkata, West Bengal, India

2. "Forward-backward correlations in proton-proton collisions at the LHC energy: A model based study"
   Authors: **Joyati Mondal**, S. Kar, H. Koley, S. Mukherjee, A. Deb and M. Mondal
   Poster presentation at 50th International Symposium on Multiparticle Dynamics (ISMD2021), 12-16 July 2021, Virtual Conference

3. "Rapidity and Transverse Momentum Dependent Forward-Backward Correlation in pp Events at $\sqrt{s}$ = 0.9 , 2.76 7 : A Study Using EPOS3 Model"
   Authors: M. Mondal., **Joyati Mondal**, S. Kar, P. Ganguly, S. Bhadra, A. Deb
   Poster presentation at International Conference on Nuclear, Particle and Accelerator Physics (ICNPAP-2018), October 23-26, 2018, Central University of Jharkhand, Brambe, Ranchi-835205, India

4. "Analysis of Correlations and Fluctuations in High Energy Interactions"
   Authors: **Joyati Mondal**, H. K. Koley, S. Mukherjee, A. Mondal , G. Bhoumick, S. Kar, A. Deb, M. Mondal
   Poster presentation at the departmental conference, Jadavpur University, February 25, 2020

5. "Radon Danger in Ground Water: An Experimental Study in Ajodhya Hill and Nearby Areas of West Bengal"
   Authors: A. K. Naskar, M. Gazi, J. Akhter, **Joyati Mondal**, A. Mondal, S. Maity, M. Mondal, and A. Deb
   Poster presentation at Environmental Radiation: Impact on Society and its Implications (ERISI), November, 15-16, 2019, Jadavpur University, Kolkata, West Bengal
   (Not included in the thesis)

6. "Erratic Fluctuations in *pPb* Collisions at LHC energy: A Monte Carlo Study"
   Authors: **Joyati Mondal**, M. Mondal, A. Mondal, S. Biswas Ghosh, A. Deb
   Poster presentation at Recent Trend in Frontier Research in Physics (RTFRT 2018), One day Seminar, March 6, 2018, Jadavpur University, Kolkata, West Bengal

List of Tables

List of Figures

Table of Contents

Chapter 1

Introduction

1.1 Prologue

The quest to uncover the smallest building blocks of matter and the fundamental forces that govern their interactions has long inspired human curiosity, and high energy physics continues this journey at the most fundamental level. The discovery of the electron by J.J. Thomson in 1897 marked the first step toward exploring the subatomic world. This was followed by Rutherford's alpha particle scattering experiment in 1911, which revealed that the nucleus is composed of protons and neutrons, together referred to as nucleons.

The search for even deeper structure continued, and in 1968, deep inelastic scattering experiments at the Stanford Linear Accelerator Center (SLAC), USA showed that protons themselves are made of smaller constituents known as quarks. Later experiments using muons and neutrinos helped to probe the internal structure of hadrons in detail. It is now well established that protons and neutrons are composed of quarks, which are held together by gluons. These fundamental constituents, quarks and gluons, are collectively referred to as partons. The existence of the gluon was confirmed in 1979 at the PETRA electron-positron collider at DESY, Germany [1]. Although quarks and gluons have not been observed as free particles, their behavior and properties are well described by the theory of strong interaction known as Quantum Chromodynamics (QCD). This theory, one of the pillars of the Standard Model (SM), explains the phenomenon of confinement where partons remain permanently bound inside hadrons such as protons and neutrons. Hadrons are categorized into two types: baryons and mesons. Baryons (and antibaryons) are composed of three quarks (or three antiquarks) and mesons are formed from a quark-antiquark pair.

The Standard Model is a well-established theoretical framework in particle physics that describes the fundamental particles and the forces acting among them, excluding gravitational interaction. It is the culmination of various independently developed theoretical models and experimental discoveries that together form our current understanding of particle physics [2]. In this section, only the main features of SM relevant to the present work are briefly outlined.

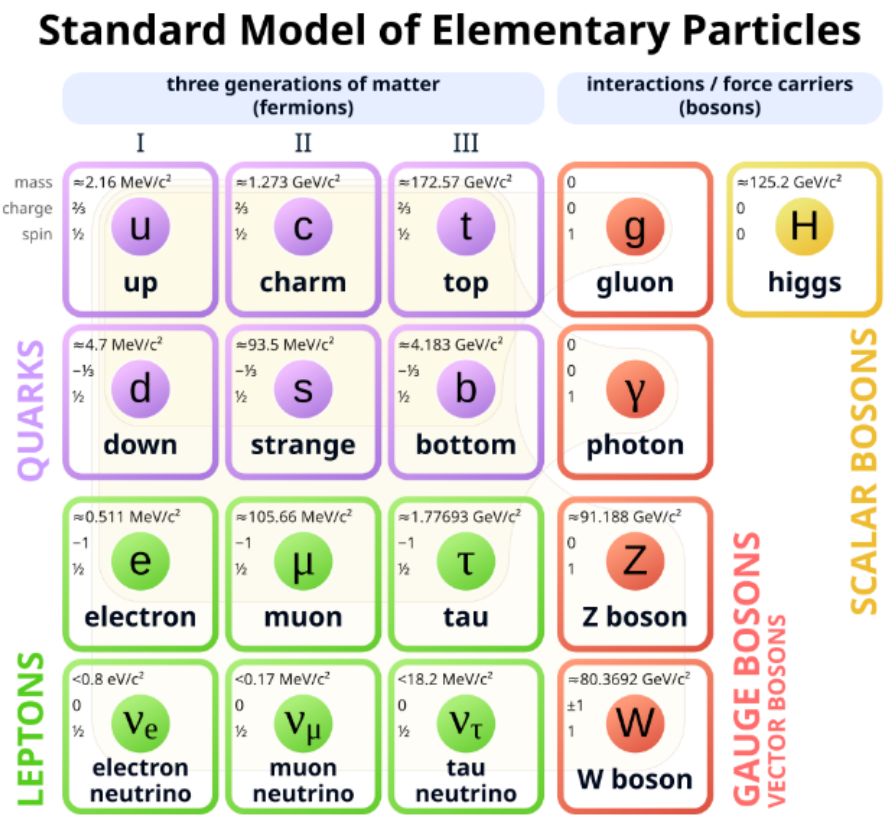

Fig. 1.1: Illustration of the Standard Model of particle physics. The figure is adapted from Ref. [3].

The SM classifies all known elementary particles into two main categories: fermions and bosons. Fermions, which are spin-half particles, constitute matter and are further divided into quarks and leptons. There are six types of quarks (u, d, c, s, t, b) and six types of leptons (e, μ, τ, ν_e, ν_μ, ν_τ) along with their corresponding antiparticles, grouped into three generations based on increasing mass. Each generation consists of two quarks and two leptons. The fundamental forces between these particles are mediated by bosons which are integer-spin particles. Photon is the mediator of electromagnetic interactions, gluons mediate the strong interactions and $W^{\pm}$ and Z^0 bosons are responsible for weak interactions. Additionally, the model incorporates the Higgs boson, a spin-zero particle that plays a crucial role in giving mass to fundamental particles through the Higgs mechanism. The discovery of the Higgs boson in 2012 by the ATLAS and the CMS collaborations at CERN provided strong experimental confirmation of this mechanism [4-5]. These elementary particles and force carriers are shown in Fig. 1.1 along with their properties (mass, charge and spin).

Quantum Chromodynamics, the theory that describes the strong interaction between quarks and gluons, exhibits two essential features:

- Color Confinement: Quarks and gluons carrying color charge cannot exist freely. Instead, they are always confined within hadrons by the strong force mediated by gluons.

- Asymptotic Freedom: When quarks are separated by very short distances, on scales smaller than that of a nucleon, the strong force between them weakens and decreases logarithmically. In this condition quarks and gluons behave as quasi-free particles. This phenomenon is known as asymptotic freedom.

However, as the distance between quarks increases, the force between them becomes stronger. If enough energy is supplied in an attempt to separate them, it does not isolate individual quarks but instead leads to the creation of new quark-antiquark pairs, resulting in the formation of new colourless hadrons. This phenomenon ensures that quarks remain confined. The interplay between strong coupling at large distances (confinement) and weak coupling at short distances (asymptotic freedom) is indeed a defining characteristic of QCD.

In 1975, J.C. Collins and M.J. Perry [6] pointed out that quarks become effectively free at sufficiently high density. Later studies have suggested that this behavior occurs only beyond certain critical values of nuclear density and temperature [7]. In relativistic heavy-ion collisions, a tiny, short-lived system with extremely high temperature and density is created. Under such extreme conditions, when quarks are brought very close together, the strong coupling constant decreases (asymptotic freedom) causing them to interact very weakly. As a result, quarks and gluons can move freely over distances larger than those confined within hadrons, effectively forming a new state of matter where they are no longer bound in the traditional sense. This phenomenon is known as deconfinement. The state of matter consisting of such deconfined quarks and gluons is called the Quark-Gluon Plasma (QGP) [8].

Quark-Gluon Plasma is a locally thermally equilibrated state of matter, consisting of deconfined quarks and gluons free to move over nuclear volumes rather than being confined within hadrons.

QGP is expected to achieve local thermal and chemical equilibrium. In this phase, the effective degrees of freedom change from hadrons to quarks and gluons with color deconfinement extending over nuclear (rather than hadronic) volumes. The essential features of QGP are: (i) the matter consists of quarks and gluons as the primary degrees of freedom, indicating a phase transition from hadronic matter to partonic matter, and (ii) the system attains local thermal equilibrium, reflecting collective behavior in a dense and strongly interacting medium. As a result, quarks and gluons become the dominant carriers of energy, momentum and quantum numbers, replacing confined nucleons.

Incidentally, QGP is believed to have dominated the universe for the first few microseconds after the Big Bang. Our universe originated approximately 13.8 billion years ago from a point-like singularity and underwent a rapid expansion. In the very first moments, between approximately 10^{-36} and 10^{-32} seconds, it experienced a brief period of exponential expansion, known as cosmic inflation. Until a few microseconds after its beginning ($t = 0$), this extremely hot and dense matter existed in the form of QGP composed of deconfined quarks and gluons [9-10]. Around one microsecond after the Big Bang, as the universe continued to cool, these quarks combined to form hadrons, marking the transition from a quark-gluon plasma to the hadronic matter that makes up the visible universe today. Moreover, while the early universe QGP existed at extremely high temperatures and nearly zero baryo-chemical potential, theoretical studies suggest that a similar state of deconfined quarks and gluons at high net-baryon density might exist in the cores of neutron stars [11], where nuclear matter is compressed to extreme densities.

Understanding the evolution of our universe during its earliest stages requires the recreation and study of quark-gluon plasma (QGP) under laboratory conditions. The human curiosity to explore matter with quark-level degrees of freedom in the laboratory has given rise to an entirely new field of research: the search and detailed study of the QGP. These efforts not only help us to uncover the properties of strongly interacting matter under extreme conditions but also offer valuable insights into the conditions that existed microseconds after the Big Bang [12].

1.2 Relativistic Heavy-ion Collisions and QGP Formation

1.2.1 QGP in the laboratory

The QGP state, as described by QCD, can be created in the laboratory through ultra-relativistic heavy-ion collisions, often referred to as “Little Bangs”. These collisions generate extremely high temperatures and energy densities, leading to conditions suitable for QGP formation. Although the system expands rapidly, preventing the establishment of global thermodynamic equilibrium, the strong particle interactions in a small, dense volume lead to local thermodynamic equilibrium. This condition allows the application of relativistic hydrodynamics to describe space-time evolution of the system.

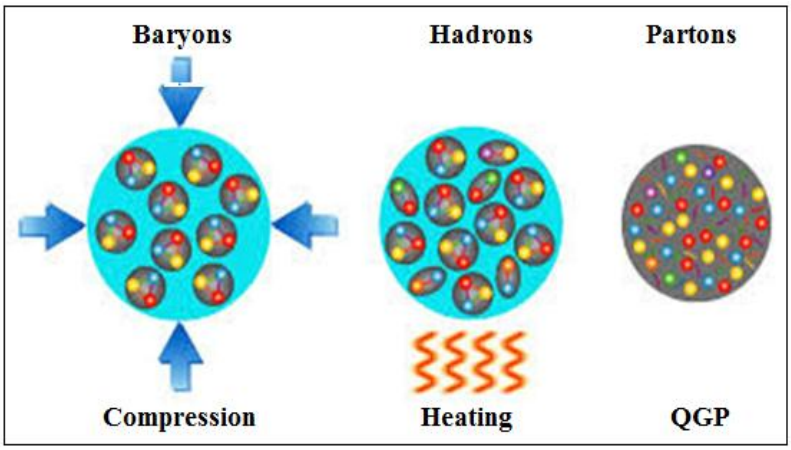

Fig. 1.2: Schematic representation of QGP formation through compression and heating.

QGP formation in heavy-ion collisions can occur via two distinct mechanisms. At relatively lower collision energies, the colliding nuclei undergo compression or stopping that produces a baryon-rich dense medium. In contrast, at higher collision energies, the nuclei become transparent to each other, resulting in heating and leaving behind a gluon-dominated, hot partonic matter in the reaction zone. Fig. 1.2 schematically represents the transition from confined matter to QGP under extreme conditions, which involves three main phases. These phases are: compression of baryons leading to a dense state, subsequent heating that results in pion production and hadron formation, and finally, the formation of a deconfined partonic phase, i.e., QGP.

The main objective of ultra-relativistic heavy-ion collision experiments is to create and explore the properties of QGP in the laboratory, thereby enhancing our understanding of the behavior of strongly interacting matter under such extreme conditions.

1.2.2 Discovery of quark-gluon plasma

The experimental search for QGP began with heavy-ion collision programs at major accelerator facilities. Early indications of a new state of matter were observed in lead-lead ($PbPb$) collisions at CERN's Super Proton Synchrotron (SPS) with center-of-mass energies per nucleon pair up to $\sqrt{s_{NN}}$ = 17.3 GeV [13]. Although initial results suggested the formation of QGP, conclusive evidence was still awaited. However, clear evidence emerged only in 2005, when experiments at the Relativistic Heavy Ion Collider (RHIC) at Brookhaven National Laboratory (BNL) confirmed the formation of QGP in gold-gold ($AuAu$) collisions at $\sqrt{s_{NN}}$ = 200 GeV. These results were announced after five years of detailed measurements by four international collaborations [10, 14-16].

Over time, several dedicated heavy-ion collision facilities have contributed to this exploration, including AGS (Alternating Gradient Synchrotron) at BNL, SPS at CERN and more recently, the Large Hadron Collider (LHC) at CERN. Early experiments at AGS and SPS focused on lower energy regimes, characterized by high baryon densities. Later collider-based experiments at RHIC and LHC explored much higher collision energies, allowing the study of QGP in conditions of near-zero baryon chemical potential. This transition from the stopping regime to the transparency regime has enabled a deeper understanding of the behavior of strongly interacting matter under extreme conditions.

1.2.3 Geometry and dynamics of heavy-ion collisions

The geometry of colliding nuclei is essential for interpreting results in heavy-ion collision experiments. These geometrical properties are typically estimated using the Glauber Model [17], which uses nuclear charge density (ρ_0) and inelastic nucleon-nucleon cross-section (σ_{inel}^{NN}) as key inputs.

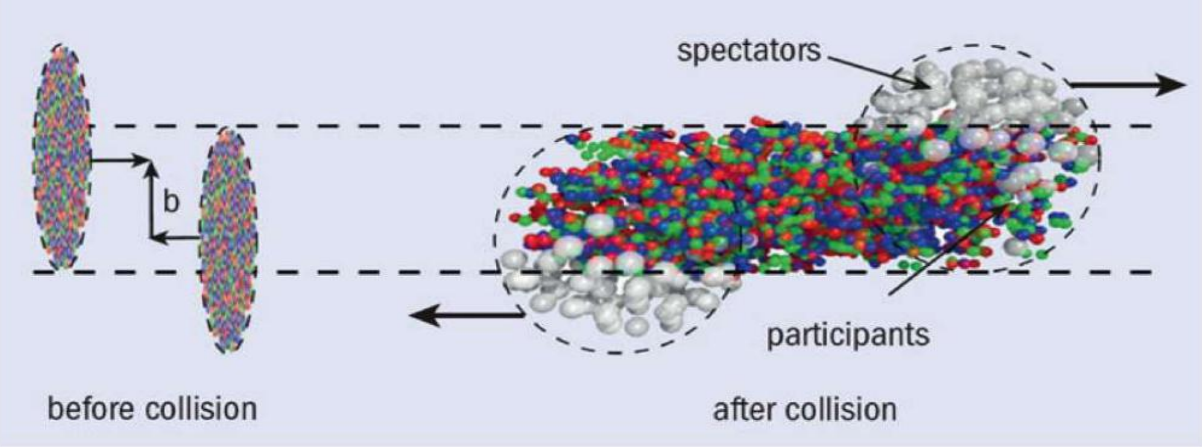

Fig. 1.3: Illustration of a typical nucleus-nucleus collision before and after interaction [18].

At relativistic speeds, both projectile and target nuclei undergo Lorentz contraction along the beam direction, appearing as flattened, pancake-like shapes. In the initial stage of the collision, partons from both nuclei undergo hard scatterings with large momentum transfers. This momentum transfer depends on the centrality of the collision, which is characterized by the impact parameter *b* defined as the perpendicular distance between the centers of the two colliding nuclei.

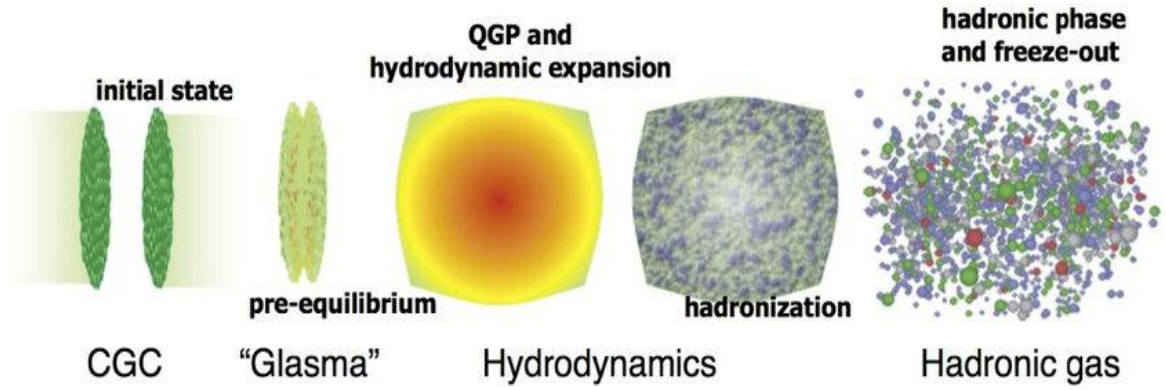

Fig. 1.4: Schematic representation of the evolution of a relativistic heavy-ion collision [19].

Fig. 1.3 illustrates a typical nucleus-nucleus collision highlighting the role of the impact parameter in defining the collision geometry. The overlap region between the nuclei, determined by the value of *b*, dictates which nucleons become participants

(those that interact) and which remain spectators (nucleons that pass through unaffected). A small impact parameter corresponds to central collisions with significant overlap and a large number of participants, whereas a large impact parameter leads to peripheral collisions involving fewer participants and more spectators. Since the impact parameter cannot be directly measured in experiments, centrality is estimated using alternative methods based on the number of participants and spectators. As the collision progresses, partons undergo multiple scatterings leading to the formation of a hot and dense fireball, which eventually thermalizes into the QGP.

Figure 1.4 schematically depicts the dynamical evolution of the system created in heavy-ion collisions, starting from the initial impact, through QGP formation and ending with final-state particle production.

1.2.4 Space-time evolution of heavy-ion collisions

The different phases of a heavy-ion collision evolving over space and time are described by the following steps:

i. **Initial state:** Figure 1.5 illustrates the space-time evolution of a heavy-ion collision. Two Lorentz contracted nuclei A and B collide at the space-time coordinate (z, t) = (0, 0). The curves shown in the figure represent hyperbolas corresponding to constant proper time ($\tau = \sqrt{t^2 - z^2}$). As a result of the collision, a large amount of energy is deposited and concentrated around the collision zone. This deposited energy is extremely high and its subsequent development may result in two possible outcomes. If the energy density and temperature remain below the threshold required for the formation of the QGP, the system will instead evolve into a hadronic gas. In this case, the high energy particles produced during the collision eventually hadronize resulting in a system composed entirely of hadrons, as illustrated on the left side of Fig. 1.5. On the other hand, if the energy density and temperature exceed the critical values, the system undergoes a phase transition that leads to the creation of a fireball of deconfined quarks and gluons. This evolution pathway is shown on the right side of Fig. 1.5

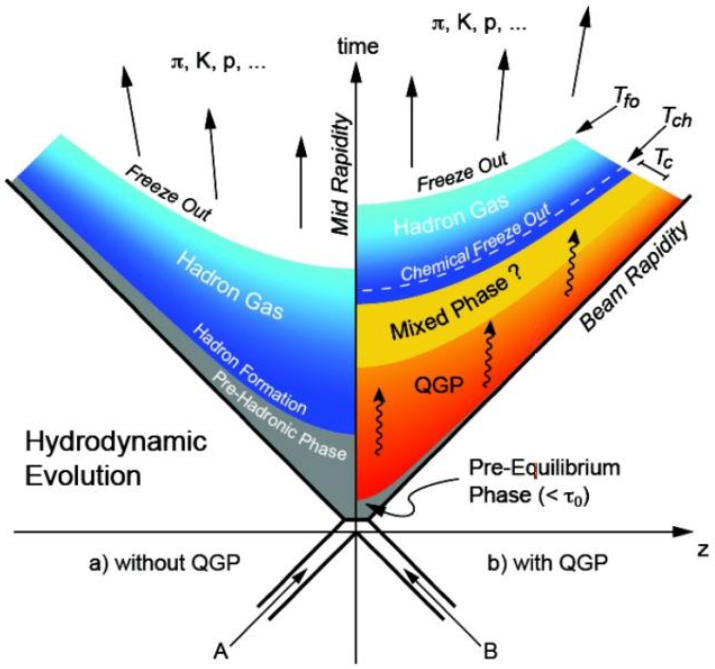

Fig. 1.5: Space-time evolution of a central heavy-ion collision [20].

ii. **Pre-equilibrium Phase ($0 < \tau <$ 1-2 fm/c):** The system enters the pre-equilibrium phase immediately after the collision at $\tau = 0$. Initially, the generated fireball of partons is not in thermal equilibrium, but the partons begin to interact intensely with each other. In this early non-equilibrium environment, semi-hard particle (generally particles with transverse momentum, $p_T > 1$ GeV/c) production dominates. The initial state of the system may be described using theoretical frameworks such as the Color Glass Condensate (CGC) [21-22] and the Glasma [23]. The CGC models the nuclei prior to collision as dense color fields known as color glass condensates. The Glasma represents the complex state that forms immediately after the collision.

iii. **Equilibrium quark-gluon plasma and hydrodynamic expansion (1-2 fm/c $< \tau <$ 6 fm/c):** When the system reaches sufficiently high energy density, the produced partons undergo multiple interactions, leading the system toward local thermal equilibrium. This thermalization typically occurs within a timescale of approximately 1 fm/c. At this stage, the system enters the QGP phase. The QGP then begins to expand due to pressure gradients and consequently cools down. During this phase, its evolution can be effectively described by viscous hydrodynamics, taking into account partonic degrees of freedom.

iv. **Hadronization ($6\ \mathrm{fm/c} < \tau < 10\ \mathrm{fm/c}$):** As the quark-gluon plasma expands and cools, it reaches a point where the temperature drops to a certain critical value, T_c. Quarks and gluons then start to combine and form hadrons. If the phase transition is of first-order, a mixed phase develops in which partons and hadrons coexist. The system expands isothermally during this stage and latent heat is consumed in converting quarks and gluons into hadrons. Two principal processes govern hadronization: fragmentation, dominant at high transverse momentum where partons with high-p_T break into low-p_T hadrons; and coalescence, more significant at low-p_T where partons with low-p_T merge to form high-p_T hadrons. Once hadronization is complete, the system transforms into a hadron gas that continues to expand with both elastic and inelastic collisions.

v. **Freeze-out ($\tau > 10\ \mathrm{fm/c}$):** Finally, when hadron interactions cease, the system freezes out. The system undergoes two freeze-out stages: chemical and kinetic freeze-out. When the temperature drops to T_{ch}, inelastic collisions among hadrons stop and the relative abundances of hadron species become fixed with no further changes in particle composition. As the system continues to expand and cool, only elastic collisions occur until it reaches the kinetic freeze-out temperature T_{f0}. At this point, hadrons stop interacting and move freely toward the detectors, carrying final-state information from the collision.

It is now clear that, as the lifetime of the QGP phase is extremely short, on the order of ~ 3 fm/c ($\sim 10^{-23}$ second), direct observation of deconfined quarks and gluons is not possible. Instead, detectors can only measure the final-state particles emerging from these collisions. Experimentalists infer the formation of the QGP and extract information about the initial conditions of the collision by analyzing these particles. Some of the experimental observables used to study and characterize the QGP are discussed in Section 1.4 of this chapter.

In addition to experimental efforts, the QGP phase is extensively studied through theoretical models and simulations. Simulations are essential to complement experimental data and provide deeper insight into the properties and evolution of the QGP. Models such as EPOS3 [24], a hybrid event generator that combines initial-state parton dynamics, hydrodynamic evolution and hadronic cascades, are used to simulate

the entire evolution of high energy collisions and reproduce key experimental observables. Similarly, the Ultra-Relativistic Quantum Molecular Dynamics (UrQMD) model [25] is used to describe the hadronic interactions and the late-stage evolution of the system, connecting the deconfined and hadronic phases. Both the EPOS3 and UrQMD models are described in detail in Chapter 2B**.** Additionally, lattice QCD and hydrodynamic models like ECHO-QGP [26] play a vital role in understanding QGP properties and interpreting experimental results under extreme conditions.

1.3 Kinematic Variables

It is necessary to use kinematic variables that are either invariant under Lorentz transformations or can be consistently interpreted across different frames of reference in the study of relativistic heavy-ion collisions. In this context, we briefly discuss some of the relevant kinematic variables used in this thesis.

1.3.1 Collision energy $\sqrt{s}$:

In high energy collider experiments, the total energy available in the CMS system for an elementary collision such as a proton-proton or proton-antiproton collision is conventionally denoted by $\sqrt{s}$. For heavy-ion collisions, the center-of-mass energy per nucleon-nucleon pair is represented as $\sqrt{s_{NN}}$ indicating the energy available for each nucleon-nucleon interaction within the colliding nuclei. The variable 's' is one of the Mandelstam variables which are Lorentz-invariant quantities used to describe the kinematics of scattering processes.

The CMS energy in a collision between two different systems, characterized by charges Z_1, Z_2 and atomic numbers A_1, A_2 (for a proton, $Z = A = 1$), is given by

$$\sqrt{s_{NN}} = 2\sqrt{s_{pp}} + \sqrt{s_{pp}}\sqrt{\frac{Z_1 Z_2}{A_1 A_2}},$$

where $\sqrt{s_{pp}}$ is the corresponding energy in pp collisions.

1.3.2 Transverse momentum (p_T):

Numerous subatomic particles are generated in high energy collisions, each characterized by their momentum p and energy E. The beamline direction, conventionally aligned with the z-axis, is referred to as the longitudinal coordinate,

while the plane perpendicular to it, encompassing the x and y axes, is known as the transverse coordinate. The three-momentum $\boldsymbol{p}$ can be decomposed into its longitudinal component p_z and its transverse component p_T. p_T is mathematically expressed as:

$$p_T = \sqrt{p_x^2 + p_y^2}.$$

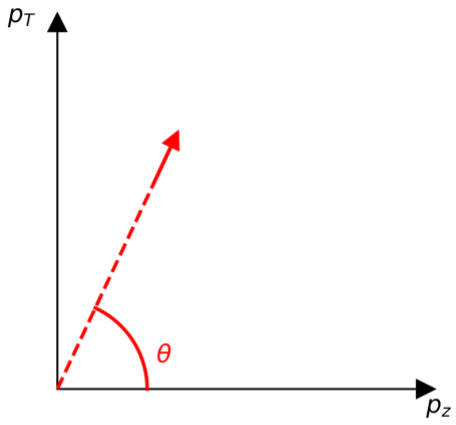

Fig. 1.6: Illustration of longitudinal and transverse momentum components.

The transverse momentum p_T remains invariant under Lorentz transformations. This concept is visually represented in Fig. 1.6. Here, θ is the angle between an emitted particle and beam axis.

1.3.3 Rapidity (y): The variable known as rapidity, y, is defined by:

$$y = \frac{1}{2}\, ln\left(\frac{E+p_z}{E-p_z}\right).$$

The shape of the rapidity distribution remains invariant under a longitudinal Lorentz boost, which means that when transitioning from the CMS to the laboratory system (LS), the rapidity values shift by a constant amount without altering the overall distribution. This property is the main advantage of using rapidity variable in studies of particle production in high energy nuclear collisions.

In asymmetric collision systems such as proton-nucleus interactions, the CMS frame does not coincide with the laboratory frame, which results in a rapidity shift that must be accounted for in experimental analyses.

For a collision between two different nuclei characterized by charge Z_1, Z_2 and atomic numbers A_1, A_2, the rapidity shift (Δy) is given by: $\Delta y \approx \frac{1}{2} \ln\left[\frac{Z_1 A_2}{Z_2 A_1}\right]$.

For pPb collision, $\Delta y \approx \frac{1}{2} \ln\left[\frac{Z_1 A_2}{Z_2 A_1}\right] = \frac{1}{2} \ln\left[\frac{82\times1}{1\times208}\right] = -0.465.$

Thus, for pPb collisions, flipping the beam (i.e., switching projectile and target directions) results in a rapidity shift of ± 0.465.

1.3.4 Pseudorapidity (η):

In high energy collider experiments, secondary particles produced from interactions are typically boosted in the z-direction along the beam axis. Rapidity (y) is commonly used to describe their distribution. However, at very high energies, where a particle's energy $E \sim pc$ and the longitudinal momentum is given by $p_z = p\,cos\theta$, rapidity can be approximated by pseudorapidity η, which is defined as:

$$y \equiv \eta = -\ln[tan\left(\frac{\theta}{2}\right)].$$

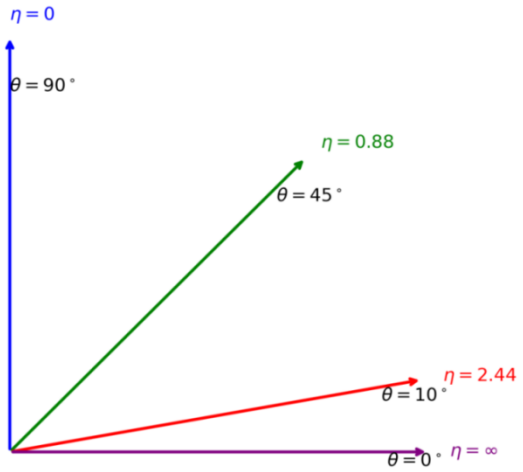

Fig. 1.7: Pseudorapidity variable η as a function of polar angle θ.

In collider experiments, pseudorapidity is preferred because it depends only on the polar angle θ. Pseudorapidity is defined irrespective of a particle's mass or collision energy and can be measured even without momentum information, which typically requires a magnetic field. Figure 1.7 illustrates the relationship between pseudorapidity

and the polar angle. It is clear that as the polar angle increases from zero, pseudorapidity gradually decreases from infinity.

However, pseudorapidity is an excellent approximation of true rapidity, particularly at very high energies where the transverse momentum of a particle is significantly greater than its mass.

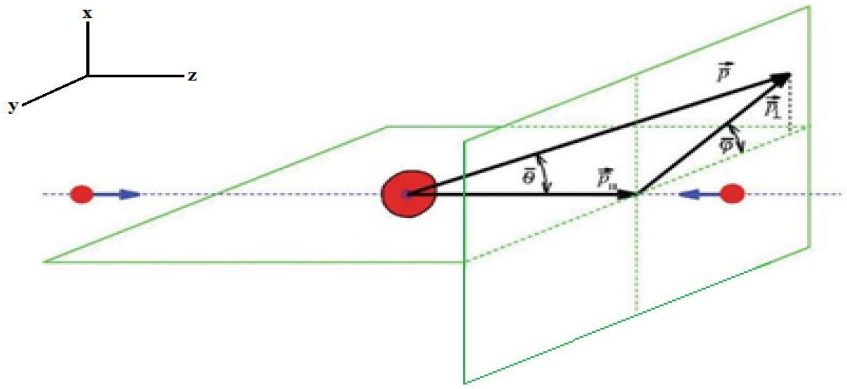

Fig. 1.8: Schematic representation of azimuthal angle Φ and polar angle θ.

1.3.5 Azimuthal angle (Φ):

The azimuthal angle Φ is defined as the angle around the beam axis in the transverse plane. Fig. 1.8 shows a schematic representation of the azimuthal angle φ. In terms of momentum components, the azimuthal angle is given by:

$$\Phi = \tan^{-1}\left(\frac{p_y}{p_x}\right).$$

1.4 QGP Signatures

As the lifetime of the QGP phase is of the order of a few fm/c, we have to rely on indirect signatures of QGP formation. Some of the signatures of QGP are the estimation of high energy density, jet quenching, strangeness enhancement, azimuthal anisotropy, elliptic flow, collective radial expansion, quarkonia suppression, direct photon and dilepton production, event-by-event fluctuations and correlations, long-range rapidity

correlations [27]. In the following section, a few relevant signatures of QGP will be briefly discussed.

1.4.1 Energy density

According to recent lattice QCD calculations, the critical energy density and temperature required for crossing the QCD phase boundary and forming the QGP are $\epsilon_c = (0.42 \pm 0.06)$ GeV/fm^3 and $T_c = (156.5 \pm 1.5)$ MeV [28]. The energy density and temperature in the early stages of a collision are thus essential observables that determine whether the necessary conditions for the QCD phase transition are achieved. First, we focus on the estimation of energy density.

Depending on the total produced transverse momentum, the energy density in a collision can be estimated using the 'Bjorken estimate' [29]:

$$\varepsilon_{Bj}(\tau) = \frac{1}{A_T \tau} \frac{dE_T}{dy},$$

where τ represents the proper time after the collision when the system reaches thermal equilibrium, A_T denotes the transverse area of the overlap region of the colliding nuclei, and $\frac{dE_T}{dy}$ is the total produced tranverse energy ($E_T = \sqrt{p_T^2 + m^2}$) per unit rapidity.

It is important to note that this estimation is based on certain assumptions such as local thermal equilibrium and longitudinal boost invariance, which implies uniform dynamics along the rapidity direction near mid-rapidity without transverse expansion.

The pseudorapidity density distribution $dN_{ch}/d\eta$ of produced charged particles is a fundamental measurement used to explore particle production mechanisms and estimate a lower bound on the energy density [30]. Fig. 1.9 shows the charged-particle pseudorapidity density for 0-5% central $PbPb$ collisions, NSD pPb collisions and INEL pp collisions at $\sqrt{s_{NN}}$ = 5.02 TeV, as measured by ALICE, along with available model calculations from EPOS 3.4 [24, 31-32] and PYTHIA 8.3 [33].

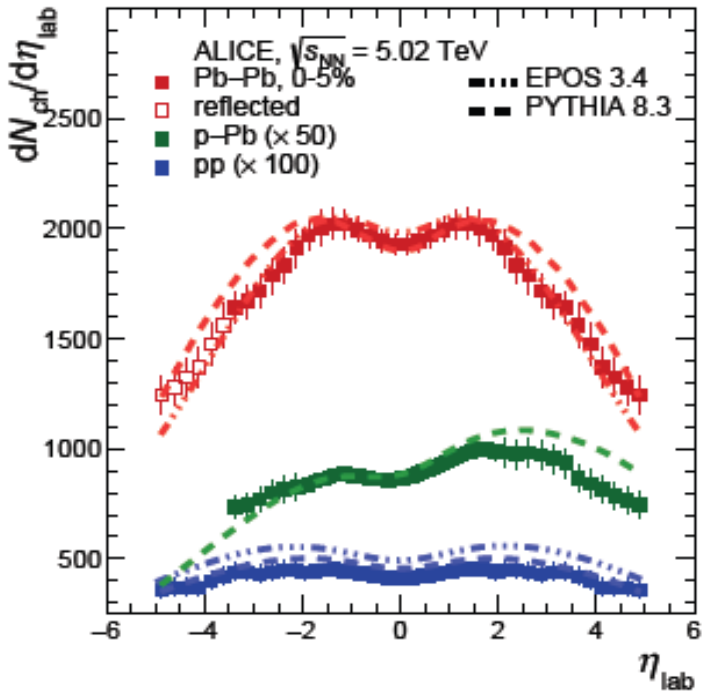

Fig. 1.9: Pseudorapidity density of charged particles in 0–5% central $PbPb$ collisions, NSD pPb collisions and INEL pp collisions at $\sqrt{s_{NN}}$ = 5.02 TeV, as measured by ALICE [30]. Dashed lines represent EPOS 3.4 model calculations, available only for pp and $PbPb$ collisions at this energy and PYTHIA 8.3, available for all collision systems.

Based on the measurements of the charged-particle pseudorapidity density and the assumption that the rapidity distribution of produced charged particles follows normal distribution, a lower-bound estimate of the energy density ε_{LB} multiplied by the formation time τ in the collisions can be derived, as given in [34]:

$$\varepsilon_{LB}\tau = \frac{1}{A_T}\frac{1}{f_{total}}\sqrt{1+a^2}\langle m\rangle\sqrt{1+\frac{1}{a^2 cosh^2\eta}}\frac{dN_{ch}}{d\eta}.$$

Here, $f_{total}(= 0.55 \pm 0.01)$ represents the ratio of charged particles to all particles, assumed to remain constant across all collision systems, $a = {}^{p_T}/_{m}$ denotes the ratio between transverse momentum and mass, and $\sqrt{1+a^2}\langle m\rangle$ represents the effective transverse mass. A_T is determined using Glauber model considering the full overlap region of the participating nucleons.

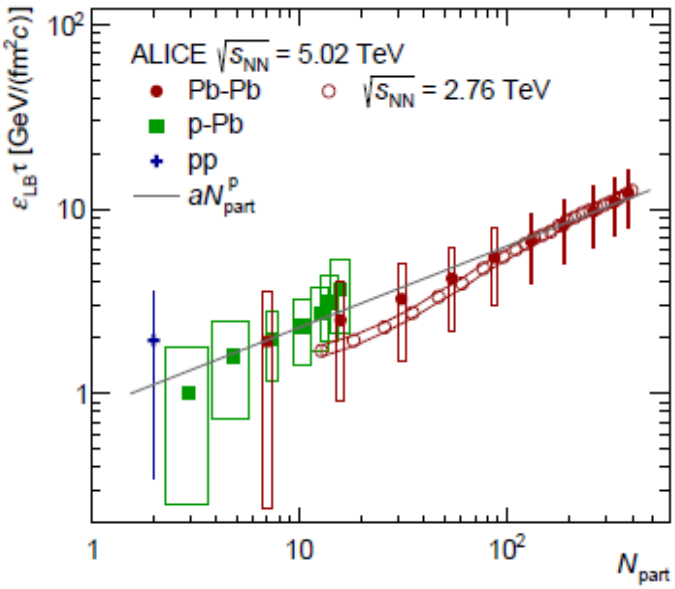

Fig. 1.10: The lower-bound estimate of the energy density multiplied by the formation time τ for pp, pPb and $PbPb$ collisions at $\sqrt{s_{NN}}$ = 5.02 TeV as a function of the number of participating nucleons [30]. The open circles represent results from $PbPb$ collisions at $\sqrt{s_{NN}}$ = 2.76 TeV derived from direct measurements of E_T [35].

Figure 1.10 displays the extracted $\varepsilon_{LB}\tau$ (solid markers) as a function of the number of participants N_{part} for pp, pPb and $PbPb$ collisions at $\sqrt{s_{NN}}$ = 5.02 TeV. The results indicate that $\varepsilon_{LB}\tau$ is approximately 1 GeV/fm^{2}c for pp and the most peripheral pPb collisions, while in the most central $PbPb$ collisions it rises to around 10 GeV/fm^{2}c. This significantly exceeds the critical energy density predicted by lattice QCD. The increasing trend of $\varepsilon_{LB}\tau$ follows a power law behavior expressed as aN_{part}^{p} with fitted parameters $a = 0.8 \pm 0.3$ GeV/fm^{2}c and $p = 0.44 \pm 0.08$. Figure 1.10 also includes earlier estimates of the Bjorken energy density (open markers) obtained from transverse energy E_T measurements in $PbPb$ collisions at $\sqrt{s_{NN}}$ = 2.76 TeV [35]. The trend observed at $\sqrt{s_{NN}}$ = 5.02 TeV is consistent with the previous measurements.

1.4.2 Two particle ridge-like correlation and jet quenching

The two-particle correlation function is constructed by analyzing the differences in azimuthal angles, $\Delta\varphi = \varphi_{trig} - \varphi_{assoc}$ and pseudorapidities, $\Delta\eta = \eta_{trig} - \eta_{assoc}$, where

φ_{trig} and φ_{assoc} (η_{trig} and η_{assoc}) correspond to the azimuthal angle (pseudorapidity) of the trigger (leading particle) and associated particles, respectively.

The correlation distribution function is mathematically expressed as follows [36]:

$$\frac{1}{N_{trig}}\frac{d^2N}{d\Delta\eta\Delta\varphi} = B(0,0) \times \frac{S(\Delta\eta,\Delta\varphi)}{B(\Delta\eta,\Delta\varphi)},$$

where N_{trig} represents the number of trigger particles within a specified p_T^{trig} (transverse momentum of trigger particle) range.

The function $S(\Delta\eta,\Delta\varphi)$ represents the per-trigger yield in the same event and is given by:

$$S(\Delta\eta,\Delta\varphi) = \frac{1}{N_{trig}}\frac{d^2N_{same}^{assoc}}{d\Delta\eta\Delta\varphi}.$$

A mixed-event background distribution $B(\Delta\eta,\Delta\varphi)$ is constructed to account for the uncorrelated particle pairs by pairing particles from different events with similar track multiplicities. This distribution is defined as:

$$B(\Delta\eta,\Delta\varphi) = \frac{d^2N^{mixed}}{d\Delta\eta\Delta\varphi},$$

where N^{mixed} represents the number of particle pairs obtained from mixed events.

$B(0,0)$ is the normalization factor.

The two-dimensional correlation distribution is projected in $\Delta\varphi$ by integrating over a defined range of Δη:

$$C(\Delta\eta,\Delta\varphi) = \frac{1}{N_{trig}}\frac{dN^{assoc}}{d\Delta\varphi}.$$

In high energy collisions, jets are collimated streams of particles generated from the fragmentation of partons. High-p_T jets originate in the early stages of the collision and traverse the evolving medium interacting with it along the way. As they propagate, they lose energy through gluon radiation and multiple interactions with the medium, a process known as jet quenching. The two-particle correlation method provides direct evidence of jet production and probes the interaction of hard-scattered partons with the medium.

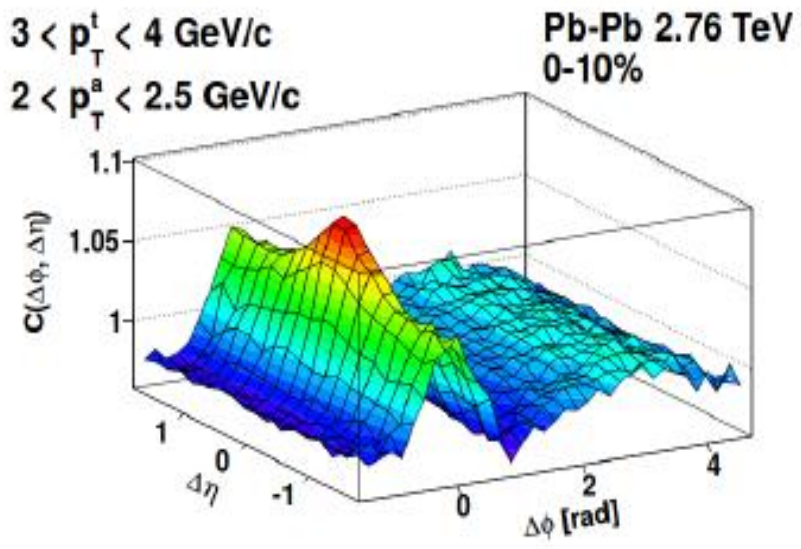

Fig. 1.11: Two-particle angular correlation measurements by ALICE Collaboration in central $PbPb$ collisions at $\sqrt{s_{NN}}$ = 2.76 TeV [37].

Short-range two-particle azimuthal correlations, characterized by $|\Delta\eta|\sim 0$, are primarily influenced by high-p_T jets, which are produced back-to-back through hard QCD scattering. These jet correlations are reflected in the $|\Delta\varphi|$ distribution. Near-side jets measured at $|\Delta\varphi|\sim 0$ travel a shorter path through the medium, while away-side jets observed at $|\Delta\varphi|\sim\pi$ traverse the entire medium, losing their energy. At large $\Delta\eta$ values, corresponding to long-range correlations, the influence of jets is minimized, enabling the investigation of the collective behavior of the produced particles.

Figure 1.11 presents two-particle correlations $C(\Delta\eta, \Delta\varphi)$ in $\Delta\eta$ and $\Delta\varphi$ as measured by ALICE Collaboration in central $PbPb$ collisions at $\sqrt{s_{NN}}$ = 2.76 TeV [37]. As seen in the figure, a clear peak at $\Delta\varphi = 0$ indicates the presence of near-side jets, whereas the absence of a significant peak at $\Delta\varphi = \pi$ suggests the suppression of away-side jets due to their interaction with the medium. It is interesting to note that a ridge-like structure appears with small $|\Delta\varphi|$ over a wide range of $|\Delta\eta|$ (long-range correlations). In the absence of medium formation, no significant structure is expected on the near side of long-range two-particle angular correlation functions, as contributions from jets and resonance decays are typically limited to short-range correlations. The appearance of the ridge structure is mainly associated with low-p_T or soft-particle phenomena. Hence, the formation of the ridge in $PbPb$ collisions at $\sqrt{s_{NN}}$ = 2.76 TeV indicates the presence of collective medium.

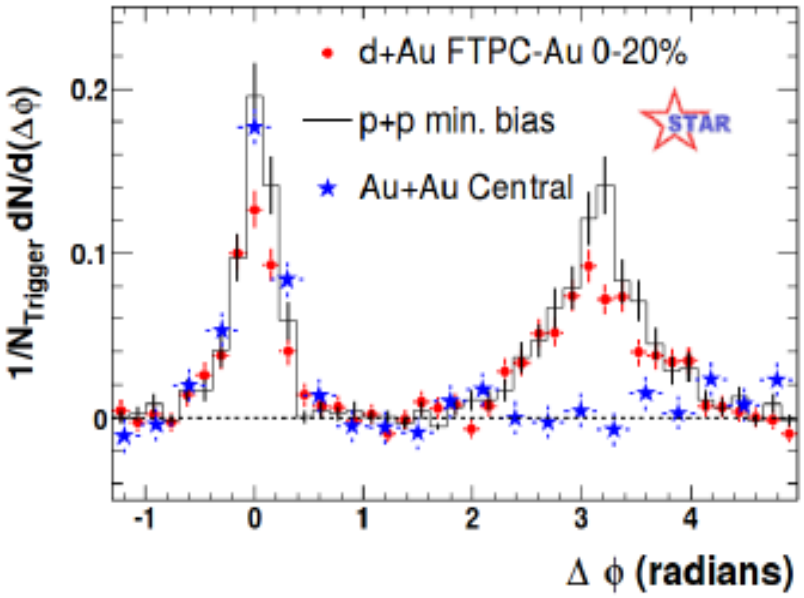

Fig. 1.12: STAR measurements of di-hadron azimuthal correlations in pp, dAu and $AuAu$ collisions at $\sqrt{s_{NN}}$ = 200 GeV [38].

Figure 1.12 represents di-hadron azimuthal correlations in pp, dAu and $AuAu$ collisions at $\sqrt{s_{NN}}$ = 200 GeV, as measured by the STAR Collaboration [38]. Trigger particles with p_T > 4 GeV/c and associated particles with p_T > 2 GeV/c were selected for the analysis. In $AuAu$ collisions, the away-side jet is significantly suppressed, whereas no such suppression of high-p_T jets is observed in dAu and pp collisions. The suppression of the away-side peak in $AuAu$ collisions provides experimental evidence of jet quenching, which corroborates the formation of QGP medium.

1.4.3 Event-by-event multiplicity fluctuations

Fluctuations in different observables such as net charge, multiplicity, particle ratios, mean transverse momentum, higher moments, etc., in ultra-relativistic heavy-ion collisions have been widely investigated, as they are important indicators of QGP formation. As a huge number of particles produced in each event of a collision, analyzing event-by-event multiplicity fluctuations in detail has been suggested as one of the signatures of the phase transition. Additionally, the study of multiplicity fluctuations is important for other event-by-event measurements.

The multiplicity fluctuation, represented in terms of the scaled variance (ω_{ch}), is defined as [39]:

$$\omega_{ch} = \frac{\langle N_{ch}^2 \rangle - \langle N_{ch} \rangle^2}{\langle N_{ch} \rangle} = \frac{\sigma_{ch}^2}{\langle N_{ch} \rangle},$$

where $\langle N_{ch} \rangle$ and σ_{ch}^2 represent the mean and variance of the charged-particle multiplicity distribution respectively.

Within the framework of the grand canonical ensemble, which may be applicable for describing particle production in heavy-ion collisions [40], the scaled variance of the multiplicity distribution is related to the isothermal compressibility (k_T), as given by [41]:

$$\omega_{ch} = \frac{k_B T \langle N_{ch} \rangle}{V} k_T,$$

where V and T are the volume and temperature of the system and k_B is the Boltzmann's constant.

Near the QCD critical point, k_T follows a power law scaling characterized by a critical exponent γ, which remains identical for systems belonging to the same universality class:

$$k_T \propto \left(\frac{T - T_c}{T_c} \right)^{-\gamma}.$$

Therefore, analyzing multiplicity fluctuations to estimate k_T provides a valuable approach for exploring the critical point in the QCD phase diagram from thermodynamic point of view.

The measurement of the multiplicity of produced particles in relativistic heavy-ion collisions is fundamental, as many experimentally observed quantities are directly linked to it. These multiplicity variations arise from fluctuations in the collision impact parameter or in the number of participant nucleons (N_{part}). Consequently, event-by-event fluctuations in participant nucleons contribute significantly to the measured multiplicity fluctuations and act as a background in determining the thermodynamic

quantities [42]. To mitigate this, narrow centrality intervals are selected, and multiplicity variations within each interval are considered. Residual participant fluctuations are estimated using the MC Glauber model [43], which treats nucleus-nucleus collisions as a superposition of individual nucleon-nucleon interactions. As a result, background fluctuations arise from both independent particle production and correlations of different physical origins. By subtracting these background contributions, the remaining fluctuations can be used to estimate k_T.

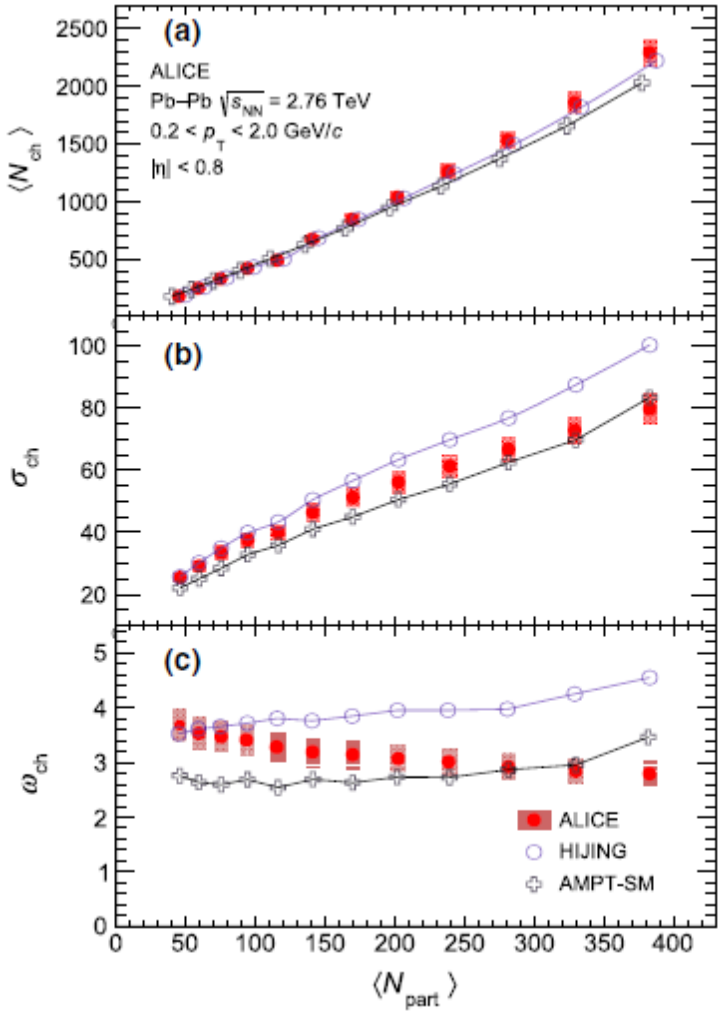

Fig. 1.13: Mean ($\langle N_{ch} \rangle$), standard deviation (σ_{ch}) and scaled variance (ω_{ch}) as a function of $\langle N_{part} \rangle$ in $PbPb$ collisions at $\sqrt{s_{NN}}$= 2.76 TeV for ALICE data along with HIJING and AMPT-SM model calculations [44].

Figure 1.13 presents the corrected mean ($\langle N_{ch} \rangle$), standard deviation (σ_{ch}) and scaled variance (ω_{ch}) as a function of $\langle N_{part} \rangle$ in $PbPb$ collisions at $\sqrt{s_{NN}}$= 2.76 TeV as measured by ALICE [44]. Predictions from the HIJING [45] and AMPT-SM [46] models are also included. It has been observed that both $\langle N_{ch} \rangle$ and σ_{ch} increase as $\langle N_{part} \rangle$ increases. Additionally, ω_{ch} decreases gradually from peripheral to central collisions. Though the model calculations are comparable to the data, they fail to describe the trend.

1.4.4 Strangeness enhancement

In proton-proton and heavy-ion collisions, the colliding particles are nucleons, primarily composed of up (u) and down (d) quarks. However, in the final state hadrons containing not only u and d quarks but also heavier quark flavors are observed. Since strange quarks are the lightest among the heavier quark families, their presence suggests production within a possible partonic medium. In a thermalized QGP, where the temperature of the system exceeds the mass of the strange quark ($m_s \gg m_{u,d}$), a large number of strange quarks and anti-quarks can be generated through various mechanisms leading to strangeness enhancement. These mechanisms include flavor creation ($qq \rightarrow s\bar{s}$, $gg \rightarrow s\bar{s}$), gluon splitting (g $\rightarrow s\bar{s}$), and flavor excitation ($gs \rightarrow gs$, $qs \rightarrow qs$). The observation of an enhanced yield of multi-strange hadrons relative to pions (which lack strangeness content) in the final state is referred to as strangeness enhancement and is considered as a key signature of QGP formation. Experimental evidence of this phenomenon has been reported in heavy-ion collision experiments conducted at CERN SPS [47], RHIC [48] and LHC [49].

The yield ratios of strange and multi-strange hadrons to pions have been analyzed to investigate possible QGP formation and are presented in Fig. 1.14 as a function of $\langle dN_{ch}|d\eta \rangle$ for pp, pPb and $PbPb$ collisions at CERN LHC energies along with predictions from various Monte Carlo models [50]. The results show strangeness enhancement in the production of strange hadrons relative to non-strange hadrons across all collision systems. A notable enhancement is observed in high multiplicity pp events. Interestingly, the trend seen in pp collisions closely resembles that of pPb collisions at a

slightly lower center-of-mass energy, both in terms of the absolute values of the ratios and their evolution with increasing multiplicity.

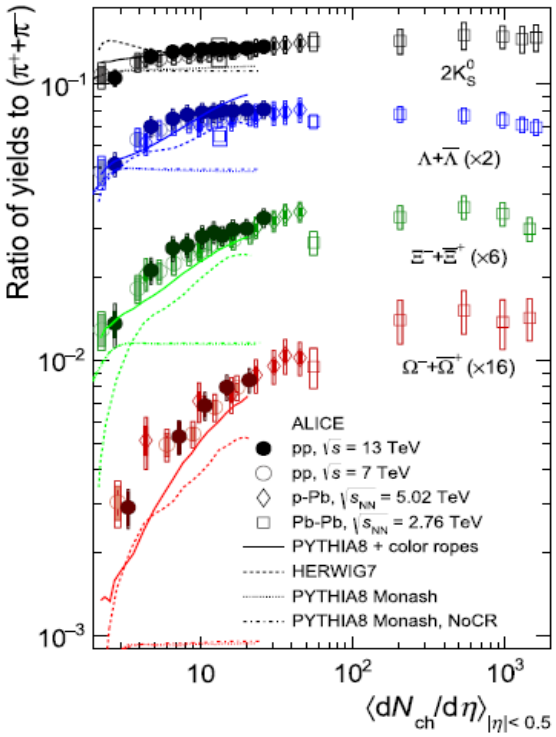

Fig. 1.14: Ratios of strange hadron yields to pions as a function of $\langle dN_{ch}|d\eta \rangle$ for pp, pPb and $PbPb$ collisions [50].

This novel observation of strangeness enhancement highlights that pp collisions, though traditionally serving as a baseline measurement, can also be studied to understand QGP formation and its properties.

1.5 Objective of the Thesis

Main objective of the present thesis is to investigate the formation and characteristics of QGP using correlation and fluctuation techniques in high energy collisions.

More specifically, the thesis focuses on exploring both long-range and short-range correlations in EPOS3 generated pp and pPb events at various LHC energies using specific Forward-Backward (FB) correlation observables.

Investigation on the fractal characteristics in multipion production process intends to uncover the possible sources of fluctuations in multiparticle production process at high and ultra-high energies.

Analysis in terms of erraticity moment aspires to capture spatial and event space fluctuations simultaneously and quantifies the amount of chaos in underlying branching processes.

1.6 Experimental Findings on Correlations and Fluctuations

A large number of experimental studies have been performed on correlations and fluctuations for a wide range of collision systems from SPS to LHC energies using different observables to identify and characterize QGP state. A brief survey of past studies relevant to this topic is carried out, highlighting the tools that have been exploited to achieve the objectives addressed in the present thesis.

1.6.1 Forward-backward correlation

Analyzing correlations between particles in different pseudorapidity regions in high energy collisions is a powerful method for exploring the complex dynamics of multiparticle production and hadronization. One of the most informative observables in this context is the forward-backward correlation, which probes the relationship between particle production in forward and backward pseudorapidity intervals that are symmetrically placed with respect to the collision vertex. These correlations carry signatures of both short-range and long-range dynamics [51-54] that originate from different physical mechanisms. Short-range correlations (SRCs) [55], typically confined within $|\eta|\sim1$, arise from processes such as jet fragmentation, minijet production and resonance decays. They are predominantly associated with particles produced at higher transverse momentum through hard and semi-hard perturbative processes. On the other hand, long-range correlations (LRCs) [56], which extend over larger η separations ($|\eta| > 1$), are associated with collective behavior and initial-state fluctuations that manifest in the final state through the evolution of the system, particularly in high energy heavy-ion collisions where the formation of QGP is expected.

The first observation of positive forward-backward multiplicity correlations in proton-antiproton ($p\bar{p}$) collisions at $\sqrt{s}$ = 540 GeV was reported by the UA5 Collaboration at the CERN SPS collider [53]. Following this, systematic studies in $p\bar{p}$ collisions were conducted across a broader energy range from $\sqrt{s}$ = 200 GeV to 900 GeV utilizing data from the Intersecting Storage Rings (ISR) [51-52]. These investigations confirmed the presence of strong FB multiplicity correlations and contributed to the understanding of the energy dependence and underlying mechanisms of particle production in hadronic collisions. Later, Bravina et al. examined pp and $p\bar{p}$ interactions at $\sqrt{s}$ = 7.86 GeV and reported that an increase in the particle multiplicity in one hemisphere of the collision system is correlated with a corresponding increase in the opposite hemisphere [57]. The correlation strength, quantified by the parameter b, was found to be 0.19 ± 0.01 for inelastic $p\bar{p}$ collisions and 0.10 ± 0.02 for pp interactions. These results were also reproduced in the quark-gluon string model (QGSM).

Though no notable FB multiplicity correlation has been reported in e^+e^- collisions by the HRS Collaboration [58], a very weak correlation strength was observed in e^+e^- annihilation by the TASSO Collaboration [59]. They analyzed FB multiplicity correlations at various energies and for different particle charge selections. Their study revealed that these correlations can be understood in terms of the fragmentation behavior of different quark flavours, as well as the production and decay of resonances. The observed correlations are also successfully described by the Lund string model. FB multiplicity correlation have also been studied by the OPAL Collaboration at LEP on a high statistics sample of Z^0 decays to multihadronic final states in e^+e^- interactions at $\sqrt{s}$ = 91.2 GeV [60]. They explained the observed positive correlations in the inclusive sample as arising from a mixture of distinct event topologies (2-, 3-, and 4-jet events), each associated with different amounts of hard gluon radiation and mean charged-particle multiplicities. The remaining positive correlation in a pure 2-jet sample is attributed to differences in quark flavor fragmentation and the production and decay of resonances. The observed results are well reproduced by the QCD-based Jetset 7.3 parton shower model, whereas Herwig 5.5 fails to accurately describe the measured correlations.

The NA22 Collaboration, in their study of σ^+p, K^+p and pp collision at $\sqrt{s}$ = 22 GeV, reported FB multiplicity correlations for all charges and for the different charge combinations [61]. Their findings indicated that these correlations primarily originate from particles produced in the central region of rapidity. Furthermore, the observed behavior was consistent with previous results obtained at ISR and CERN $p\bar{p}$-Collider. The experimental results were also compared with predictions from Monte Carlo models such as LUND, DPM and FRITIOF and a geometric interpretation was explored, linking FB correlations in hadron-hadron and e^+e^- collisions through impact parameter considerations.

The E735 Collaboration conducted a detailed study of FB multiplicity correlations in $p\bar{p}$ collisions at $\sqrt{s}$ = 0.3 to 1.8 TeV [62]. The findings were analyzed using a cluster model, which assumes that particle production occurs through cluster formation and decay, leading to correlated particle emission across separated pseudorapidity intervals. Following these experimental observations, Giovannini and Ugoccioni subsequently proposed a statistical framework based on the weighted superposition of Negative Binomial Distributions, known as the clan model, which successfully described the observed FB correlation strength in both hadron-hadron and electron-positron collisions by incorporating the concept of particle leakage from clans into both hemispheres [63].

Numerous theoretical models have been put forth to explain the experimental results on FB correlations. The Dual Parton Model (DPM) predicted significant FB multiplicity correlations as a natural consequence of multi-pomeron exchanges in high energy hadronic collisions. Capella and Tran Thanh Van demonstrated that particles produced in well-separated rapidity intervals exhibit long-range correlations due to the multiple partonic chains formed during the interaction [64]. This concept was further elaborated in a comprehensive review of the DPM, where FB correlations were emphasized as a key feature of the model [54].

The String Fusion Model (SFM), based on the parton picture of strong interactions, predicted that FB correlations arise from the overlapping and fusion of color strings formed in high energy nucleus-nucleus collisions [65-66]. Amelin *et al.* studied both forward-forward and forward-backward multiplicity correlations to distinguish string

fusion effects from hadron clustering mechanisms, and found that string fusion enhances long-range correlations [67]. They discuss results from AB collisions at CERN SPS and RHIC. Braun and Pajares, using the percolating color string framework, further investigated forward-backward correlations in transverse momentum distributions and showed that nonlinear effects from string interactions led to significant correlations across separated rapidity regions with predictions at SPS, RHIC and LHC energies [68]. Brogueira *et al.* applied the percolation model to pp collisions and observed that the FB correlation strength remained approximately constant over a wide rapidity range [69].

The theoretical foundation for long-range correlations in heavy-ion collisions including those contributing to FB multiplicity correlations, has been established through a Monte Carlo framework based on string fusion and fluctuations in the number of emitters [70]. FB multiplicity correlations between separated rapidity and azimuthal windows have subsequently been explored within a model that considers strings as independent, identical emitters [71].

FB multiplicity correlations have been studied within the CGC framework by Armesto, McLerran and Pajares [72]. In this approach, strong long-range components were predicted, with their strength increasing with collision centrality and being more pronounced for mesons than baryons.

The PHOBOS Collaboration investigated FB correlations of charged-particle multiplicities in $AuAu$ collisions at $\sqrt{s_{NN}}$ = 200 GeV using symmetric pseudorapidity bins [73]. The analysis indicates that short-range correlations play a significant role in the observed FB multiplicity correlations and comparisons with phenomenological models are interpreted through the framework of particle clustering. The STAR collaboration measured FB multiplicity correlations in $AuAu$ and pp collisions at $\sqrt{s_{NN}}$ = 200 GeV [74]. They observed strong short- and long-range correlations in central $AuAu$ collisions that decrease with decreasing centrality. These findings qualitatively align with DPM and CGC predictions, where multiple parton interactions and longitudinal color flux tubes contribute to the observed long-range correlations. A detailed investigation of FB multiplicity correlations, based on two-particle rapidity correlations through the dynamical fluctuation parameter σ_c^2 in forward-backward pseudorapidity windows for both ring-like and jet-like events in ^{16}O-AgBr interactions at 60 A GeV was

reported in Ref. [75]. The experimental results confirm correlations among the produced particles in the forward and the backward pseudorapidity region for both event types.

The ATLAS Collaboration measured forward-backward correlations of charged-particle multiplicities and summed transverse momentum in inelastic pp collisions at $\sqrt{s}$ = 0.9 and 7 TeV [76]. Jet-like structures were further explored through azimuthal distributions of charged particles with respect to the highest-p_T (leading) particle within a defined kinematic region. The measurements were compared to PYTHIA and HERWIG++ predictions, which show a good agreement with the data.

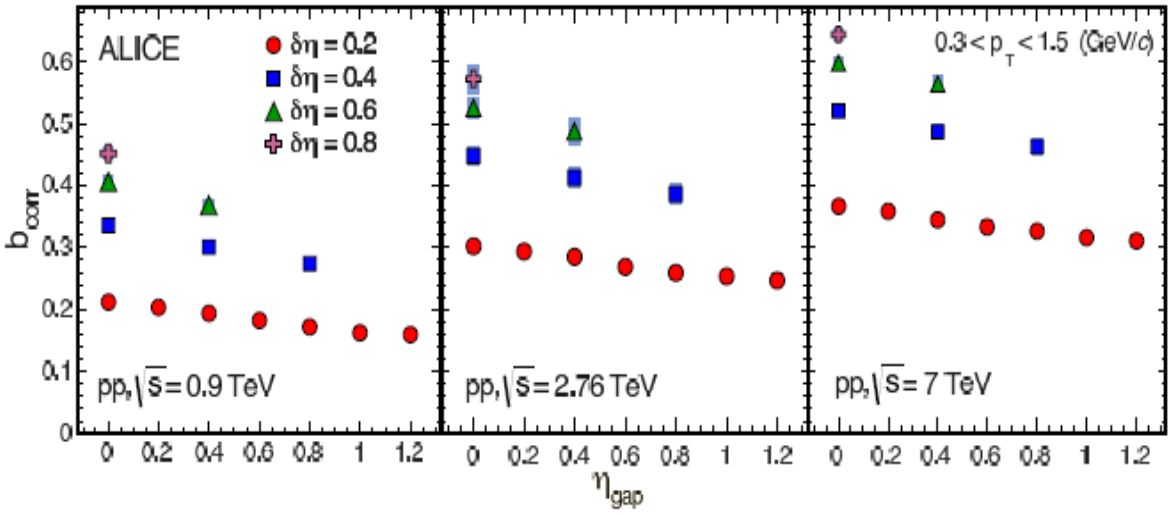

Fig. 1.15: FB multiplicity correlation coefficient b_{corr} as a function of η_{gap} for four pseudorapidity window widths in pp collisions at three different center-of-mass energies [77].

The ALICE Collaboration measured FB multiplicity correlations in pp collisions at $\sqrt{s}$ = 0.9, 2.76 and 7 TeV [77], investigating their dependence on pseudorapidity gap (η_{gap}), window width and transverse momentum. They found that correlation coefficient b_{corr} decreases gradually with increasing η_{gap}, while retaining a significant baseline value over the entire η_{gap} range (as shown in Fig. 1.15) and that for all collision energies, the correlation coefficient is observed to increase with $\delta\eta$. QGSM [78] successfully described ALICE data [77] and concluded that the multistring processes due to multi-pomeron exchanges were the main contributor to the FB correlations [79].

Interestingly, the strong FB correlations observed by the ATLAS [76] and ALICE [77] Collaborations in pp collisions are in contrast to the weak correlations reported by the STAR Collaboration [74].

There are also significant positive FB correlation values reported in pp, pPb and $PbPb$ collisions by the ATLAS Collaboration [80]. They highlighted that the strength of these correlations increases with system size being more pronounced in pPb and $PbPb$ collisions compared to pp, indicating the growing influence of multiple parton interactions and collective effects.

A recent study using the UrQMD model investigates FB multiplicity correlations and fluctuations in $AuAu$ collisions across various beam energies [81]. The variation of correlation and fluctuation parameters with beam energy, centrality, rapidity gap and window size is examined. The results indicate contributions from both short- and long-range correlations, with the former attributed to resonance decays or cluster formation, and the latter to hadronic rescattering and fragmentation of longitudinally stretched strings across rapidity.

1.6.2 Fractal characteristics in high energy collisions

The presence of large dynamical fluctuations in the produced particle spectra is considered an indicator of the QGP. Studies on these fluctuations in high energy interactions provide valuable insights into the dynamics of particle production. Bialas and Peschanski introduced the concept of intermittency [82-83] to investigate dynamical fluctuations, describing the power law behavior of factorial moments with respect to phase-space interval size in multipion production during heavy-ion interactions. This behavior suggests the presence of self-similar fluctuations which in turn indicate a fractal nature. Based on this analysis, researchers have hypothesized that the multipion production process may exhibit fractal properties and have also suggested a possible connection between intermittency and fractality. Additionally, the cascading mechanism inherent in multipion production reflects a fractal structure within the hadronization process.

Various methods have been suggested to study the fractal structure in the multipion production process using techniques derived from fractal theory. Among the most widely used approaches are those introduced by Hwa based on the $G_q$moment [84], and Takagi using the T_q moment [85]. Hwa introduced the use of G_q moments to examine the scaling properties of multiplicity distributions within narrow rapidity windows to characterize chaotic fluctuations in rapidity distributions. The results suggest that the observed scaling behavior is consistent with the multifractal formalism, providing deeper insight into the self-similar nature of the particle production process. F. Takagi analyzed the multifractal nature of multiplicity distributions in proton-antiproton and electron-positron interactions. Takagi, by employing the T_q moments, demonstrated that these distributions exhibit power law behaviors indicating a multifractal structure. It has been suggested that the scaling exponents derived from experimental data support the hypothesis that fractal-like structures govern particle production in heavy-ion collisions. D. Ghosh *et al.* explored the self-similarity in multiparticle production using various hadron-nucleus, lepton-nucleus and nucleus-nucleus interactions [86-93]. S. Bhattacharyya *et al*. applied Takagi's T_q moment method to charged pion production in ^{16}0-AgBr (2.1 A GeV) and ^{24}Mg-AgBr (4.5 A GeV) interactions and observed clear multifractal scaling behavior in multiparticle production [94].

C. K Peng *et al*. introduced and discussed the Detrended Fluctuation Analysis (DFA) technique to detect long-range correlations in nonstationary time series [95] and initially applied it to DNA sequences. J. W. Kantelhardt *et al.* extended DFA to Multifractal Detrended Fluctuation Analysis (MFDFA) enabling the characterization of multifractality in nonstationary time series. They established its equivalence to the partition function-based formalism for stationary signals and demonstrated its ability to distinguish multifractality arising from long-range correlations versus broad probability distributions [96]. A. Bhaduri and D. Ghosh analyzed cardiac dynamics during meditation using chaos-based nonlinear methods, specifically MFDFA and visibility network analysis [97]. P. Oswiecimka et al. [98] conducted a comparative analysis of MFDFA and WTMM (wavelet transform modulus maxima) in detecting monofractal and multifractal features and revealed that MFDFA is more reliable especially when the fractal nature of the data is unknown, whereas WTMM may produce biased results in some cases. Various studies [99-101] have further explored the applicability of

advanced multifractal analysis techniques in diverse time series. Diffusion Entropy Analysis (DE) [102] has been introduced to address the limitations of variance-based techniques. Further advancements include the Balanced Estimator of Diffusion Entropy [103-107] which enhance the accuracy of scaling exponent evaluation in short time series. Additionally, a factorial-moment-based method for estimating probability moments has been proposed to detect multifractals within short time series, offering an alternative method for analyzing complex dynamical systems [108].

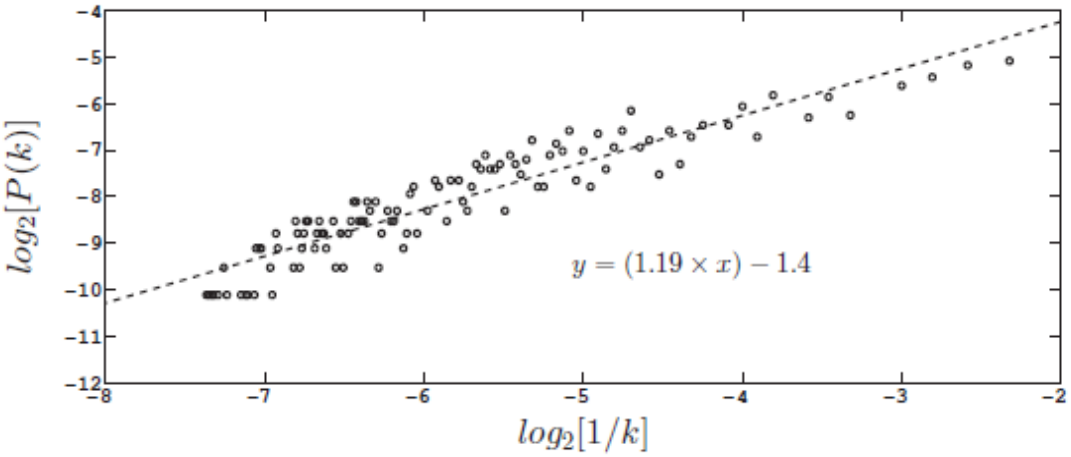

Fig. 1.16: Plot of $\log_2[1/k]$ versus $\log_2[P(k)]$ for the visibility graph constructed for $\pi^- - AgBr$ interactions at 350 GeV [120].

A significant development in this type of analysis is the Power of Scale-Freeness of Visibility Graph (PSVG) [109-112]. Visibility graph (VG) technique has been employed in various fields, including traffic congestion, turbulence, exchange rate dynamics, critical phenomena in the Ising model, and human heartbeat fluctuations [97,113–118]. With its proven effectiveness in studying critical phenomena, VG analysis has been extensively applied to explore the multifractal characteristics of multiparticle production in high energy collisions. S. Bhaduri and D. Ghosh examined ultrarelativistic nuclear collisions through the PSVG technique and confirmed that the fractal behavior depends on target excitation [119]. They also investigated pion multiplicity fluctuations in hadron-nucleus and nucleus-nucleus collisions using the VG method. The results revealed that the PSVG parameter captures features of fluctuation dynamics and indicates possible QGP-like phase transitions, with a clear power law behavior observed in the log-log degree distribution of the visibility graph (as shown in Fig. 1.16) [120].

Additionally, S. Bhaduri *et al.* applied the PSVG technique alongside Multifractal Detrended Cross-Correlation Analysis (MF-DXA) to study pion fluctuations in two-dimensional phase space. Their analysis showed strong scaling behavior and high cross-correlation between pseudorapidity and azimuthal angles highlighting the effectiveness of PSVG in assessing criticality in phase transitions [121]. Expanding on these studies, A. Bhaduri *et al.* explored azimuthal pion fluctuation in ultrarelativistic nuclear collisions, focusing on centrality dependence using chaos-based complex network analysis [122].

On the other hand, Mali *et al.* [123] employed the Horizontal Visibility Graph (HVG) [124-125] and Sandbox (SB) algorithm to analyze multifractality in pseudorapidity distributions of singly charged particles in high energy nucleus-nucleus collisions. Their findings indicate that the HVG-SB technique is a highly effective tool for characterizing multifractality in multiparticle emission data and in certain cases, provides more precise results than traditional methods.

1.6.3 Erraticity analysis in multiparticle production

In high energy collisions, researchers initially concentrated on analyzing averaged characteristics such as mean multiplicity, the first few moments of the multiplicity distribution and rapidity distributions. As accelerator energies increased, it became possible to divide the rapidity range into finer bins and analyze particle multiplicity fluctuations. This revealed significant fluctuations in the pseudorapidity distributions of produced particles in various collision systems, leading to the concept of intermittency, where normalized factorial moments exhibit a power law dependence on phase-space bin size [82-83]. However, traditional factorial moment methods that utilize horizontal or vertical averaging fail to capture both spatial (bin-to-bin fluctuations within an event) and event-to-event (between events) fluctuations simultaneously, which results in a loss of crucial information about the complexity of multiparticle production.

An analytical framework that simultaneously captures both spatial and event-by-event fluctuations through erraticity moments was first introduced by Cao and Hwa [126-127]. They [128] also explored two main types of branching models: one based on pure gluon dynamics in perturbative QCD and another that included quarks in

addition to gluons [129]. Using perturbative QCD and cascade models, they simulated events to investigate the temporal evolution of particle production through the normalized variance of multiplicity distributions across successive generations. In parallel, spatial characteristics were explored by analyzing fluctuations in normalized event factorial moments along with the corresponding entropy index. Their findings further revealed that branching in perturbative QCD exhibits chaotic features [129]. Although the normalized variance provided insight into generation-wise development, it was not experimentally measurable. In contrast, other indicators like the normalized event factorial moment, the moment of moments and the entropy index were found to be experimentally accessible and useful for studying chaoticity in high energy collisions.

Wang *et al.* [130-131] explored the chaotic nature of multiparticle production in 400 GeV/c proton-proton collisions, based on the methodology proposed by Cao and Hwa. Their results (Fig. 1.17(a)) indicate that these collisions exhibit chaotic behavior, which becomes more pronounced as the average multiplicity of the final-state particles decreases.

Cao and Hwa [132] later suggested new measures of erraticity that extend the concept of bin-size dependence in the moment of factorial moments. These updated erraticity measure represented as μ_q' were applied to ECOMB-generated events, with tuning to match NA22 and NA27 experimental data. Figure 1.17(b) presents their results, showing the variation of μ_q' with q obtained using two distinct analytical approaches. A similar analysis using new erraticity measures based on pp collision data at 400 GeV/c was conducted by Wang et al. [133] and showed results consistent with Cao and Hwa, suggesting that the ECOMB Monte Carlo model captures spatial fluctuations in soft hadronic events.

Furthermore, Hasan *et al.* [134] investigated spatial fluctuations in the final states of 14.6 A GeV Si-emulsion collisions. They used entropy indices to quantify these fluctuations and found significantly higher values than those from uncorrelated event simulations, indicating strong chaotic behavior. Their comparison with FRITIOF generated events suggested that the model could only partially account for the observed fluctuations. In a related study, event-by-event analysis in the context of factorial moments of ^{28}Si–nucleus interactions at 4.5A and 14.5A GeV/c reveals that erraticity

moments decrease with increasing multiplicity and are largely unaffected by variations in the energy or mass of the projectile and target nuclei [135]. A comparison with uncorrelated FRITIOF simulated data suggests that fluctuations in low-multiplicity events are predominantly driven by statistical effects. D. Chandra *et al.* [136] analyze nonstatistical fluctuations in the angular distribution of charged particles from ^{16}O-AgBr and ^{32}S-AgBr interactions at 200 A GeV using erraticity moments. They observe a consistent scaling pattern and report that experimental data exhibit substantially stronger fluctuations compared to those generated by FRITIOF and random number simulations.

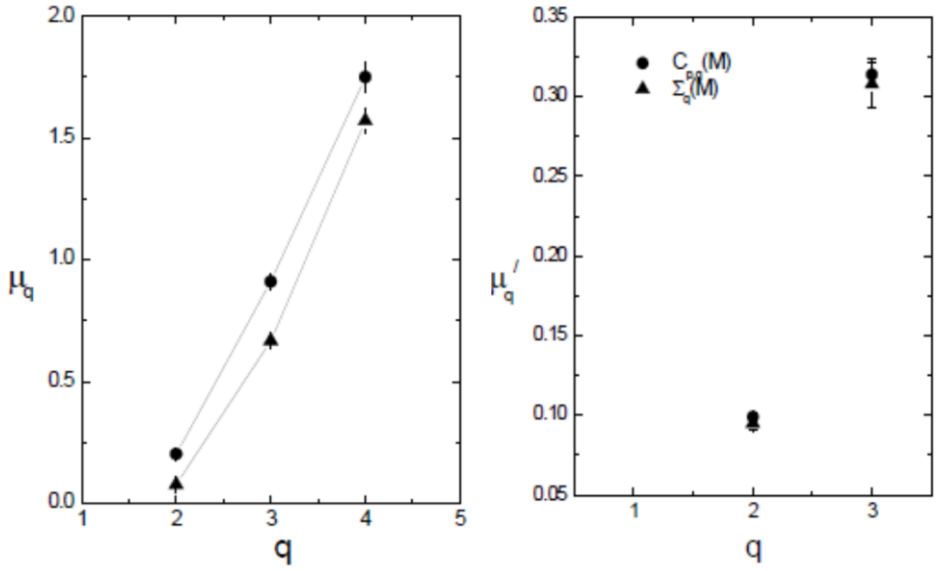

(a) (b)

Fig. 1.17: (a) Plot of μ_q versus q plot for different average multiplicity event samples in 400 GeV/c pp collisions. Solid circles represent the event sample with $Nev \geq 4$, while solid triangles correspond to $Nev \geq 10$ [130]. (b) Variation of μ_q' with q, as obtained through two different analytical methods [132].

D. Ghosh *et al.* explored event-to-event fluctuations in multipion production in ^{32}S-AgBr interactions at 200A GeV using erraticity measures [137-138]. In the latter study, newly defined erraticity measures were employed and a comparative analysis with random and VENUS model data revealed chaotic behavior in particle production

dynamics. In a subsequent study, they present a comprehensive multidimensional erraticity analysis of the same interaction and found a clear scaling relationship between erraticity moments and phase-space partitioning, thereby providing a deeper understanding of the chaotic nature of pion production [139]. D. Ghosh *et al.* also examine the erratic behavior of multipion production in $\pi^- - AgBr$ interactions at 350 GeV [140]. A notably large entropy index observed in this study suggests significant chaoticity in pion emission, which was found to diminish with increasing average multiplicity. R. Gupta *et al.* have performed intermittency and erraticity analysis of charged-particle distributions in $PbPb$ collisions at $\sqrt{s_{NN}}$ = 2.76 TeV [141-142]. The study has quantified event-by-event fluctuations through erraticity indices [141] across low-p_T ranges providing a benchmark for comparison with experimental data.

1.7 Organization of Thesis

Chapter 1: Introduction

Chapter 1 provides an overview of the physics of high energy collisions, highlighting the motivation for studying QGP formation, fundamental concepts and relevant observables. It concludes with the objectives of the thesis and a brief review of related literature.

Chapter 2A: Nuclear Emulsion Technique

Chapter 2A introduces the nuclear emulsion detection technique, describing track formation, track characteristics and the classification of secondary charged particles produced in high energy collisions. It briefly presents the measurement methods, along with the advantages and limitations of nuclear emulsion detectors. Details of the experimental data used in this thesis are also provided, including the pseudorapidity and multiplicity distributions of the produced particles.

Chapter 2B: Monte Carlo Simulations of High Energy Interactions

This chapter discusses Monte Carlo-based simulation models, specifically EPOS3 and UrQMD, used in this thesis. These models are employed to compare experimental results with theoretical predictions. A detailed discussion is provided on their working mechanisms, the generated event samples and the validation of the simulated events.

Chapter 3 Study of Forward-Backward Correlations at the LHC Energies

Chapter 3 presents a comprehensive study of forward-backward correlations among produced particles in high energy collisions. This includes investigations for EPOS3 generated pp events at $\sqrt{s}$ = 0.9, 2.76, 7 and 13 TeV and pPb events at $\sqrt{s_{NN}}$ = 5.02 TeV, emphasizing the influence of parameters such as the gap between FB windows (η_{gap}), collision energy, window width ($\delta\eta$) and minimum transverse momentum (p_{Tmin}). Further, the chapter provides a first systematic investigation of the collision energy dependence of $\delta\eta$-weighted average FB multiplicity and momentum correlation coefficients in pp collisions across different LHC energies. It also explores the multiplicity class dependence of momentum correlations in pp and pPb systems. Finally, the chapter analyzes the behavior of the strongly intensive observable $\sum(N_f, N_b)$ as a function of multiplicity bin width and separation between FB window centers (η_{sep}). The chapter concludes with a summary of the main findings.

Chapter 4: Fractal Characteristic Studies in High Energy Collisions

Chapter 4 explores the fractal characteristics of heavy-ion collisions at high energies to identify possible sources of multiparticle production using Visibility Graph (VG) technique. The power of scale freeness property of VG (PSVG) and related observables are studied for ^{16}O-AgBr interactions at 60 A GeV and their centrality dependence is also explored. Further, transverse momentum threshold (p_{Tmin}) dependence of fractal behavior is analyzed for EPOS3 simulated pp events at $\sqrt{s}$ = 7 TeV. The chapter ends with a summary of the findings.

Chapter 5 Evidence of Chaos in Multiparticle Production

Chapter 5 investigates the chaotic nature of multiparticle production using the framework of erraticity analysis. The analysis is systematically organized across datasets: ^{16}O-AgBr interactions at 60 A GeV, and corresponding IEH and UrQMD events, where erraticity measures are calculated and compared. A dedicated section explores the dependence of erraticity on target excitation by categorizing the experimental data accordingly. The chapter further extends the study to EPOS3 generated pp and pPb

collisions at LHC energies, offering a comparative analysis across different systems and energy scales. The chapter concludes with a summary of the findings.

Chapter 6 Concluding Remarks

Chapter 6 concludes the thesis by summarizing the major findings from the analyses and also discusses the future scope for extending the work to gain deeper insights into multiparticle production dynamics.

References

[1] R. Brandelik, *et al.*, Phys. Lett. B **86** (2), 243-249 (1979).

[2] S. Weinberg, Eur. Phys. J. C **34**, 5 (2004).

[3] "Standard Model of Elementary Particles", Wikimedia Commons, https://commons.wikimedia.org/wiki/File:Standard_Model_of_Elementary_Particles.svg (accessed July 4, 2025).

[4] G. Aad *et al.* (ATLAS Collaboration), Phys. Lett. B **716**, 1-29 (2012). https://doi.org/10.1016/j.physletb.2012.08.020

[5] S. Chatrchyan *et al.* (CMS Collaboration), Phys. Lett. B **716**, 30–61 (2012). https://doi.org/10.1016/j.physletb.2012.08.021

[6] J. C. Collins and M. J. Perry, Phys. Rev. Lett. **34**, 1353 (1975).

[7] J. Greensite, An introduction to the confinement problem, vol. **821**. (2011).

[8] L. C. P. Van Hove, *Theoretical prediction of a new state of matter, the "quark-gluon plasma" (also called "quark matter")*, Proc. 17th Int. Symp. on Multiparticle Dynamics, Seewinkel, Austria, (1987).

[9] H. Satz, Ann. Rev. Nucl. Part. Sci. **35**, 245-270 (1985).

[10] J. Adam, *et al.* (STAR Collaboration), Nucl. Phys. A **757**, 102-183 (2005).

[11] E. Annala, T. Gorda, A. Kurkela *et al.*, Nature Phys. **16**(9), 907-910 (2020).

[12] K. Yagi, T. Hatsuda, and Y. Miake, Quark-Gluon Plasma: From Big Bang to Little Bang, Cambridge University Press, 2005.

[13] U. W. Heinz and M. Jacob, Theoretical Physics Division: Geneva, Switzerland, 2000. arXiv:nucl-th/0002042

[14] I. Arsene *et al.* (BRAHMS Collaboration), Nucl. Phys. A **757**, 1-27 (2005).

[15] B. B. Back *et al.* (PHOBOS Collaboration), Nucl. Phys. A **757**, 28-101 (2005).

[16] K. Adcox *et al.* (PHENIX Collaboration), Nucl. Phys. A **757**, 184-283 (2005).

[17] R. Glauber, Nucl. Phys. B **21**, 135-157 (1970).

[18] R. M. Djilkibaev (2021), *An issue of determination of the centrality in nucleus-nucleus collisions.* arXiv preprint arXiv:2103.16899.

[19] B. Müller, *Investigation of hot QCD matter: theoretical aspects*, Phys. Scr. T**158**, 014004 (2013).

[20] Mattia. (2016). Evolution of Collisions and QGP.

[21] E. Iancu and R. Venugopalan, *The Color glass condensate and high-energy scattering in QCD*, arXiv:hep-ph/0303204.

[22] F. Gelis, E. Iancu, J. Jalilian-Marian, and R. Venugopalan, Ann. Rev. Nucl. Part. Sci. **60**, 463-489 (2010), arXiv:1002.0333 [hep-ph]

[23] F. Gelis, T. Lappi, and L. McLerran, Nucl. Phys. A **828**, 149-160 (2009). arXiv:0905.3234 [hep-ph]

[24] K. Werner, B. Guiot, *et al*., Phys.Rev. C **89**, 064903 (2014).

[25] M. Bleicher *et al.*, J. Phys. G: Nucl. Part. Phys. **25**, 1859–1896 (1999).

[26] L. Del Zanna, G. Inghirami *et al*., Eur. Phys. J. C **73**, 2524 (2013).

[27] M. Kleimant, R. Sahoo, T. Shuster, and R. Stock, *Global Properties of Nucleus-Nucleus Collisions, Lecture Notes in Physics*, **785**, 23-103 (2010).

[28] HotQCD Collaboration, A. Bazavov *et al*., Phys. Lett. B **795**, 15–21 (2019). arXiv:1812.08235 [hep-lat].

[29] J. D. Bjorken, Phys. Rev. D **27**, 140–151 (1983).

[30] ALICE Collaboration, *The ALICE experiment-A journey through QCD*, arXiv:2211.04384 [nucl-ex].

[31] H. J. Drescher *et al*., Phys. Rep. **350**, 93-289 (2001).

[32] K. Werner *et al.*, Phys. Rev. C **82**, 044904 (2010).

[33] C. Bierlich *et al.*, JHEP **10**, 134 (2018).

[34] S. Acharya *et al.* (ALICE Collaboration), Phys. Lett. B **845**, 137730 (2023).

[35] J. Adam *et al.* (ALICE Collaboration), Phys. Rev. C **94**, 034903 (2016).

[36] S. Kar *et al.*, J. Phys. G: Nucl. Part. Phys. **45**, 125103 (2018).

[37] K. Aamodt *et al.* (ALICE Collaboration), Phys. Lett. B **708**, 249-264 (2012).

[38] J. Adams *et al.* (STAR Collaboration), Nucl. Phys. A **757**, 102 (2005).

[39] H. Heiselberg, Phys. Rept. **351**, 161–194 (2001).

[40] A. Andronic *et al.*, Nature **561**(7723), 321–330 (2018).

[41] S. Mrowczynski, Phys. Lett. B **430**, 9-14 (1998).

[42] V. Begun, M. Mackowiak-Pawlowska, arXiv:1705.01110[nucl-th], P. Braun-Munzinger *et al.*, Nucl. Phys. A **960**, 114–130 (2017).

[43] M. L. Miller *et al.*, Ann. Rev. Nucl. Part. Sci. **57**, 205–243 (2007).

[44] S. Acharya *et al.* (ALICE Collaboration), Eur. Phys. J. C **81** (11), 1012 (2021).

[45] W. T. Deng *et al.*, Phys. Lett. B **701**, 133–136 (2011).

[46] Z. W. Lin *et al.*, Phys. Rev. C **72**, 064901 (2005).

[47] F. Antinori *et al.* (WA97 Collaboration), Nucl. Phys. A **661**, 130-139 (1999).

[48] G. Agakishiev *et al.* (STAR Collaboration), Phys. Rev. Lett. **108**, 072301 (2012).

[49] B. B. Abelev *et al.* (ALICE Collaboration), Phys. Lett. B **728**, 216-227 (2014).

[50] S. Acharya *et al.* (ALICE Collaboration), Eur. Phys. J. C **80**, 693 (2020).

[51] G. J. Alner *et al.* (UA5 Collaboration), Phys. Rep. **154**, 247 (1987).

[52] R. Ansorge *et al.* (UA5 Collaboration), Z. Phys. C **37**, 191 (1988).

[53] K. Alpgard *et al.* (UA5 Collaboration), Phys. Lett. B **123**, 361 (1983).

[54] A. Capella *et al*., Phys. Rep. **236**, 225 (1994).

[55] A. Capella and A. Krzywicki, Phys. Rev. D **18**, 4120 (1978).

[56] W. Kittel and E. A. De Wolf, Soft Multihadron Dynamics, World Scientific, Singapore (2005).

[57] L. V. Bravina *et al.*, Sov. J. Nucl. Phys. **50**, 245 (1989).

[58] M. Derrick *et al.* (HRS Collaboration), Phys. Rev. D **34**, 3304 (1986).

[59] W. Braunschweig *et al.* (TASSO Collaboration), Z. Phys. C **45**, 193 (1989).

[60] R. Akers *et al.* (OPAL Collaboration), Phys. Lett. B **320**, 417 (1994).

[61] V. V. Aivazyan *et al.* (NA22 Collaboration), Z. Phys. C **42**, 533 (1989).

[62] T. Alexopoulos *et al.* (E735 Collaboration), Phys. Lett. B **353**, 155 (1995).

[63] A. Giovannini and R. Ugoccioni, Phys. Rev. D **66**, 034001 (2002).

[64] A. Capella and J. T. T. Van, Z. Phys. C **18**, 85 (1983).

[65] N. S. Amelin, M. A. Braun, and C. Pajares, Phys. Lett. B **306**, 312 (1993); Z. Phys. C **63**, 507 (1994).

[66] M. A. Braun and C. Pajares, Nucl. Phys. B **390**, 542 (1993).

[67] N. S. Amelin *et al*., Phys. Rev. Lett. **73**, 2813 (1994).

[68] M. A. Braun and C. Pajares, Phys. Rev. Lett. **85**, 4864 (2000).

[69] P. Brogueira, J. Dias de Deus, and C. Pajares, Phys. Lett. B **675**, 308 (2009).

[70] V. V. Vechernin and R. S. Kolevatov, Phys. At. Nucl. **70**, 1797 (2007); **70**, 1809 (2007).

[71] V. V. Vechernin, Nucl. Phys. A **939**, 21 (2015); Proc. Sci. QFTHEP2013, 055 (2013).

[72] N. Armesto, L. McLerran, and C. Pajares, Nucl. Phys. A **781**, 201 (2007).

[73] B. B. Back *et al.* (PHOBOS Collaboration), Phys. Rev. C **74**, 011901 (2006).

[74] B. I. Abelev *et al.* (STAR Collaboration), Phys. Rev. Lett. **103**, 172301 (2009).

[75] M. Mondal *et al.*, Phys. Part. Nucl. Lett. **14**, 459–464 (2017).

[76] G. Aad *et al.* (ATLAS Collaboration), J. High Energy Phys. **07** (2012) 019.

[77] J. Adam *et al.* (ALICE Collaboration), J. High Energy Phys. **05** (2015) 097.

[78] A. B. Kaidalov, Phys. Lett. **116** B, 459 (1982); Phys. At. Nucl. **66**, 1994 (2003).

[79] L. V. Bravina, J. Bleibel, and E. E. Zabrodin, Phys. Lett. B **787**, 146 (2018).

[80] M. Aaboud *et al.* (ATLAS Collaboration), Phys. Rev. C **95**, 064914 (2017).

[81] J. Thakur, A. Mukhopadhyay, and P. Mali, Nucl. Phys. A **1035**, 122659 (2023).

[82] A. Bialas and R. Peschanski, Nucl. Phys. B **273**, 703–718 (1986).

[83] A. Bialas and R. Peschanski, Nucl. Phys. B **308**, 857–867 (1988).

[84] R. C. Hwa, Phys. Rev. D **41**, 1456 (1990).

[85] F. Takagi, Phys. Rev. Lett. **72**, 32 (1994).

[86] D. Ghosh *et al*., Europhys. Lett. **23**, 91 (1993).

[87] D. Ghosh *et al.*, Phys. Rev. D **51**, 3298 (1995).

[88] D. Ghosh *et al*., Z. Phys. C **73**, 269 (1997).

[89] D. Ghosh *et al*., Phys. Rev. C **58**, 3553 (1998).

[90] D. Ghosh *et al*., Int. J. Mod. Phys. A **14**, 2091 (1999).

[91] D. Ghosh *et al*., Phys. Rev. C **65**, 067902 (2002).

[92] D. Ghosh *et al*., Fractals **11**, 331 (2003).

[93] D. Ghosh *et al*., Phys. Rev. C **70**, 054903 (2004).

[94] S. Bhattacharyya, D. Ghosh, A. Deb, Physica A **390**, 4144 (2011).

[95] C. K. Peng *et al*., Phys. Rev. E **49**, 1685 (1994).

[96] J. W. Kantelhardt *et al*., Physica A **316**, 87–114 (2002).

[97] A. Bhaduri, D. Ghosh, Front. Physiol. **7**, 44 (2016).

[98] P. Oswiecimka *et al*., Phys. Rev. E **74**, 016103 (2006).

[99] E. Serrano, Physica A **388**, 2793–2805 (2009).

[100] Y. X. Huang *et al*., Phys. Rev. E **84**, 016208 (2011).

[101] S. Dutta *et al*., Front. Physiol. **4**, 274 (2013).

[102] N. Scafetta *et al*., Phys. Rev. E **66**, 036130 (2003).

[103] J. Qi *et al*., Phys. Rev. E **84**, 066114 (2011).

[104] W. Zhang *et al*., Phys. Rev. E **86**, 056107 (2012).

[105] X. Pan *et al*., Phys. Lett. A **378**, 2591 (2014).

[106] X. Pan *et al*., PLoS One **9** (12), e116128 (2014).

[107] Y. Yang *et al*., Chin. J. Phys. **55**, 2325 (2017).

[108] L. Qiu *et al*., Phys. Rev. E **94**, 062201 (2016).

[109] L. Lacasa *et al*., Proc. Natl. Acad. Sci. USA **105** (13), 4972 (2008).

[110] A. L. Barabasi *et al*., Science **286** (5439), 509 (1999).

[111] L. Lacasa *et al.*, Europhys. Lett. **86** (3), 30001 (2009).

[112] M. Ahmadlou *et al*., Physica A **391** (20), 4720 (2012).

[113] M. Andjelković *et al*., Phys. Rev. E **91** (5), 052817 (2015).

[114] C. Liu *et al*., Physica A **389** (13), 2675–2681 (2010).

[115] Y. Yang *et al*., Physica A **388** (20), 4431–4437 (2009).

[116] L. Zhao *et al*., PLoS One **12** (1), e0170467 (2017).

[117] S. Jiang *et al*., Appl. Phys. Lett. **102** (25), 253702 (2013).

[118] A. Bhaduri *et al*., Physica A **482**, 786–795 (2017).

[119] S. Bhaduri and D. Ghosh, Mod. Phys. Lett. A **31** (27), 1650158 (2016).

[120] A. Bhaduri and D. Ghosh, Int. J. Mod. Phys. A **31** (35), 1650185 (2016).

[121] S. Bhaduri *et al*., Eur. Phys. J. A **53**, 135 (2017).

[122] A. Bhaduri, S. Bhaduri, and D. Ghosh, Phys. Part. Nucl. Lett. **14** (4), 576–583 (2017).

[123] P. Mali *et al*., Mod. Phys. Lett. A **32** (08), 1750024 (2017).

[124] B. Luque *et al*., Phys. Rev. E **80** (4), 046103 (2009).

[125] L. Lacasa *et al*., Phys. Rev. E **82** (3), 036120 (2010).

[126] Z. Cao, R. C. Hwa, Phys. Rev. Lett. **75** (7), 1268 (1995).

[127] R. C. Hwa, Acta Phys. Pol. B **27**, 1789 (1996).

[128] Z. Cao, R. C. Hwa, Phys. Rev. D **53**(11), 6608–6618 (1996).

[129] Z. Cao, R. C. Hwa, Phys. Rev. D **54**, 6674 (1996).

[130] W. Shaoshun *et al*., Phys. Lett. B **416** (1–2), 216–219 (1998).

[131] W. Shaoshun, W. Zhaomin, Phys. Rev. D **57**(5), 3036–3039 (1998).

[132] Z. Cao, R. C. Hwa, Phys. Rev. D **61**, 074011 (2000).

[133] S. Wang, C. Wu, Z. Wang, Phys. Lett. B **458** (4), 505–510 (1999).

[134] R. Hasan *et al*., J. Phys. G: Nucl. Part. Phys. **28** (12), 2939 (2002).

[135] S. Ahmad *et al*., J. Phys. G Nucl. Part Phys. **30** (9), 1145 (2004).

[136] D. Chanda *et al*., Phys. Rev. C **71** (3), 034904 (2005).

[137] D. Ghosh, A. Deb, M. Mondal, and J. Ghosh, Phys. Lett. B **540** (1–2), 52–61 (2002).

[138] D. Ghosh, A. Deb, M. Mondal, J. Ghosh, *Phys. Rev. C* **68** (2), 024908 (2003).

[139] D. Ghosh, A. Deb *et al*., *J. Phys. G: Nucl. Part. Phys.* **31**(9), 1083 (2005).

[140] D. Ghosh, A. Deb *et a*l., *J. Phys. G: Nucl. Part. Phys.* **35** (12), 125005 (2008).

[141] R. Gupta and R. Sharma, arXiv:1411.0280 [hep-ph] (2014).

[142] R. Gupta, S. K. Malik, Adv. High Energy Phys. **2020**, 5073042 (2020).

Chapter 2A

Nuclear Emulsion Technique

2A.1 Introduction

Among the various tracking devices utilized in particle physics, nuclear emulsion detectors offer the highest spatial resolution for measuring ionizing particle track. These detectors have played a crucial role in several groundbreaking early discoveries and achievements in particle physics, such as the discovery of the pion [1].

Fundamentally, nuclear emulsion detectors are photographic plates composed of silver halide ($AgBr$) crystals uniformly embedded in a gelatin matrix. When a charged particle passes through the emulsion, it ionizes the medium along its trajectory creating a latent image track. This track becomes visible only after a chemical development process, making it possible to analyze the particle's path under a microscope.

In recent years, advancements in automated high-speed scanning systems and continuous improvements in emulsion gel composition have significantly enhanced their precision and data acquisition capability [2]. One notable innovation is the Emulsion Telescope Technique with Magnetic Field, developed by the Jadavpur–Lyon–Santander–Strasbourg collaboration (NA17 experiment approved by CERN), which enables momentum measurement of charged particles with up to 1% resolution for momenta up to 300 GeV [3].

Even after more than a century of use, nuclear emulsions continue to be an essential tool in experimental physics. They remain exceptionally effective for studying short-lived particles whose decay vertices occur within millimeters of their production point. Their role is expanding in neutrino physics and other emerging fields requiring high-precision tracking. Furthermore, their potential extends beyond fundamental research with growing applications in radiation monitoring, cosmic ray studies and space-based experiments.

2A.2 Track Formation in Nuclear Emulsion

When a charged particle traverses the nuclear emulsion, it interacts with the uniformly dispersed silver halide crystals embedded in the gelatin matrix. These interactions cause localized changes in the crystal structure through electro-ionic mechanisms, resulting in the formation of tiny silver nuclei known as latent image specks. During

chemical development, these specks act as catalysts, promoting the reduction of nearby silver ions into visible metallic silver. This process selectively amplifies the affected crystals while unaffected ones are removed during fixing. The resulting black silver grains firmly embedded in the gelatin form a permanent track that traces the path of the incident particle. High spatial resolution is achieved by using emulsions with fine grain sizes and minimal background sensitivity.

- **Formation of latent image**

Latent image formation mechanism is well described by the Gurney-Mott theory [4], originally proposed in 1938. According to this model, the process involves two stages: electronic and ionic. In the electronic stage, incident radiation excites electrons within silver bromide crystals, which then migrate and become trapped at specific sites known as sensitivity specks. These specks are typically microscopic imperfections or impurity centers, such as silver sulfide, that act as electron traps. In the subsequent ionic stage, these negatively charged sites attract mobile silver ions, resulting in the formation of metallic silver atoms at those trap locations. Repeated cycles of this process lead to the growth of tiny silver clusters that make up the latent image.

- **Development of latent image**

During chemical development, the latent image specks initiate the reduction of silver ions by weak reducing agents present in the developer. A silver halide grain containing a sufficiently large latent image cluster is entirely reduced to metallic silver, whereas grains lacking such centers remain unaffected. The unaltered grains are then removed in a fixing bath, typically sodium thiosulfate, which dissolves residual silver halide. The final outcome is a visible, permanent track of dark metallic silver grains embedded in the gelatin. The precision of track formation depends on several parameters including the sensitivity of the emulsion, the energy of the incident particle and the depth at which the interaction occurs within the emulsion layer.

2A.3 Track Characteristics

After track formation, various properties of tracks formed by charged particles in nuclear emulsion are analyzed to extract physical information. Three important characteristics are discussed below:

i. Grain density

Grain density refers to the number of developed silver grains per micron along the track. It is proportional to the rate of energy loss of particle per unit track length dT/dx (in KeV/micron) and to the square of the charge of the particle Z^2, as confirmed by experimental findings.

An empirical relation describing this behavior is [5]:

$$dn/dx = c[1 - \exp\{bz(dT/dx)^{1/2} - a^{1/2}\}]$$

where a, b and c are fitting parameters, and z is the charge of the ionizing particle.

Grain density typically increases toward the end of track. However, at relativistic speeds, it reaches a minimum near β = 0.45 and then rises again and becomes nearly constant for β > 0.995 [6- 7]. This is attributed to field distortions due to Lorentz contraction, which expand the ionization region around the track. Moreover, although the energy loss increases with particle energy (as$\sim \log E$), not all of this energy results in grain formation because part of it is deposited far from the core due to secondary interactions such as delta ray production. Additionally, Cherenkov radiation generated in gelatin when $\beta > 2/3$ can contribute to the observed increase in grain density by sensitizing nearby crystals and making them developable.

ii. Delta rays

Delta rays are high energy secondary electrons ejected when the electric field of a moving charged particle interacts with atomic electrons. When these electrons acquire energies greater than a few KeV, they can escape their original grain and induce development in neighboring grains that appear as side tracks or spurs.

For energies below ~ 5 KeV, these electrons remain localized near the main trajectory and contribute significantly to the observed grain density. Therefore, only these low-energy delta rays are considered when relating grain density to localized ionization, as higher-energy electrons often dissipate energy too far from the track to contribute meaningfully.

iii. Shrinkage factor

Since both gelatin and glycerin are hygroscopic in nature, the physical thickness and refractive index of the emulsion, whether processed or unprocessed, can vary depending on the ambient humidity. To account for this variability, a shrinkage factor S is introduced, defined as:

$$S = \frac{\text{Thickness of emulsion layer during exposure}}{\text{Thickness of emulsion layer during scanning}}.$$

This factor is essential for accurate estimation of track parameters like grain density, range and angle. Without correcting for shrinkage, these measurements can be significantly distorted. Generally, the shrinkage factor is provided by the manufacturer to ensure precise data analysis.

2A.4 Classification of Secondary Charged-Particle Tracks

The particles emitted after interactions are categorized into four main types based on their ionization, energy, range and velocity [8]:

i. **Black particles:** These are heavy, low-energy target fragments of various elements like carbon, lithium, beryllium etc. with ionization $I \geq 10I_0$ (I_0 is the minimum ionization of a singly charged particle). Their ranges are less than 3 mm, velocities $v < 0.3c$ (c is the velocity of light in vacuum) and energies below 30 MeV. Due to their short ranges and overlapping ionization, precise charge or element identification is generally not possible in emulsion experiments.

ii. **Grey particles:** They are mostly fast target recoil protons with energies up to 400 MeV. Their ionization lies between $1.4I_0 \leq I < 10I_0$, range is greater than 3 mm and velocities range from $0.3c \leq v \leq 0.7c$. Occasionally, grey tracks

may include deuterons, tritons or helium-3 nuclei from intra-nuclear cascades.

iii. **Shower particles:** These are relativistic particles, mainly pions, with ionization $I \leq 1.4I_0$ and energies in the GeV range. They travel at relativistic speeds, $v \geq 0.8c$ and are not usually confined within the emulsion pellicle. Neutral pions ($\boldsymbol{\pi^0}$) do not produce tracks due to their lack of charge.

iv. **Projectile Fragments:** These fragments originate from the incident projectile and are characterized by nearly constant ionization, long ranges and emission angles within 5° of the beam direction. They are often used to study projectile fragmentation dynamics.

2A.5 Measurement System

A modern compound microscope is an essential tool for analyzing particle tracks in nuclear emulsion. Among the most suitable instruments for this purpose is the Leitz Metalloplan microscope, equipped with several specialized attachments for accurate data collection.

i. **Scan 2000 Stage**

The Leitz Scan 2000 provides precise horizontal movement through a joystick-controlled scanning stage. It operates in the Microvarioscan mode, which incorporates scanning patterns such as Varioscan, Microscan and Macroscan. In Microscan mode, the stage follows a meander path defined by its start and end points. The system displays X and Y coordinates digitally based on a fixed reference frame.

ii. **Z-display**

The Z-display measures the Z co-ordinate of any point on the stage. To obtain the Z-coordinate, a reference point is first selected using the "REF" switch. The focus is then adjusted to the desired point and its Z-position is shown digitally.

iii. **Objectives**

Objectives form real images of the observed objects and are categorized into dry and immersion types:

- **Dry objectives** are mainly used for initial scans. High-power dry lenses (over 20× magnification) often produce suboptimal images unless used with a matching cover glass.
- **Immersion objectives** using cedarwood oil help reduce spherical aberration and coma by maintaining optical homogeneity. The refractive indices of the cedarwood oil, emulsion gelatin and cover glass are each close to 1.52, which allows aplanatic focusing and enhances image quality at high magnification.

The details of the types, magnifications and applications of objectives are provided in Table 2A.1.

iv. Binocular tube

The binocular viewing system of the Metalloplan microscope supports wide-field observation. It includes a Clausen micrometer and calibrated scales, along with a pair of eyepieces that magnify the image formed by the objective.

v. Illumination and filters

The microscope includes a controllable light source with adjustable intensity. A heat-absorbing filter is also integrated to prevent thermal distortion during observation.

Table 2A.1: Types, magnification powers and typical applications of Leitz microscope objectives used in nuclear emulsion analysis.

Type of Objective	Magnification (Leitz)	Application
Dry Objectives	10×, 20×, 25×	Low power scanning
Oil-immersion Objectives	40X, 100X	Accurate measurement

2A.6 Scanning Methods

Two standard scanning techniques are used for analyzing nuclear emulsions:

i. Area or volume scanning

In area scanning, the focal plane is moved vertically through the depth of the emulsion from its surface to the supporting glass by smoothly adjusting the fine

focus control. During this process events appear and disappear as they come into and go out of focus. Each field of view is carefully examined throughout the entire thickness of the emulsion to ensure complete three-dimensional coverage of a defined area that effectively corresponds to a scanned volume.

Area scanning is used in the following situations:

- When it is necessary to locate all events of a specific type within a given volume of emulsion.
- When a sample of a particular kind of event is required.
- When a representative and unbiased set of events is needed.
- When both the count and distribution of events in a given volume must be determined.

However, area scanning is not an effective method for identifying single diffractive dissociation events or interactions involving hydrogen nuclei, as these are typically more difficult to detect using this approach.

ii. Along the track scanning

If a stack of nuclear emulsion plates is exposed to a beam of particles entering perpendicularly through one face, and the goal is to examine the density and distribution of the incoming beam, then the recommended method is to move across each plate parallel to the leading edge and perpendicular to the direction of the tracks. This approach is referred to as along the track scanning.

A few general remarks on the scanning procedure are worth noting. Scanning is often a tedious and time-consuming task that demands a high level of concentration from the observer. The accuracy and reliability of the experimental results depend significantly on the scanner's decisiveness and consistency. Appropriate precautions must be taken to minimize observer bias and subjectivity in the data. While electronic counting may offer a quicker alternative, it lacks the discernment required for accurate scanning.

2A.7 Measurement of Space Angle

The space angle X between two tracks can be determined using a straightforward coordinate-based method. If the direction cosines of the two tracks are represented as (l_1, m_1, n_1) and (l_2, m_2, n_2), then the cosine of the angle between them is calculated as:

$$\cos X = l_1 l_2 + m_1 m_2 + n_1 n_2.$$

To compute the direction cosines of a given track, one can use the spatial coordinates of any two distinct points lying along that track. Suppose the coordinates of these points are (x_1, y_1, z_1) and (x_2, y_2, z_2). Then, the direction cosines (l, m, n) can be obtained from the differences in these coordinates as:

$$l = \frac{x_2 - x_1}{d}, \qquad m = \frac{y_2 - y_1}{d}, \qquad n = \frac{z_2 - z_1}{d},$$

where

$$d = \sqrt{(x_2 - x_1)^2 + (y_2 - y_1)^2 + (z_2 - z_1)^2}.$$

2A.8 Advantages and disadvantages of nuclear emulsion detectors

Nuclear emulsion detectors offer several advantages. Key benefits include the following:

- **High spatial resolution and full angular coverage**
  Nuclear emulsion detectors provide excellent spatial resolution due to the presence of fine silver halide grains typically ranging from 0.2 to 0.6 μm in diameter. These microcrystals record the passage of charged particles with sub-micrometer precision and allow detailed reconstruction of their trajectories and interaction vertices. The full 4π angular acceptance of emulsion layers ensures that charged particles emitted in any direction are captured and enables a complete and unbiased analysis of event topologies and reaction mechanisms.
- **Permanent recording and storage of interactions**
  Nuclear emulsions create a permanent photographic record of particle interactions. This feature ensures that events can be reanalyzed later with improved measurement techniques.
- **Sensitivity to a wide range of particle types**
  Emulsion detectors are sensitive to all charged particles, from highly ionizing fragments (black and grey particles) to fast-moving relativistic particles (shower particles). They are capable of recording both low energy and high energy interactions without a lower energy threshold.

- **Capability to identify short-lived particles**
  Emulsions can detect decay vertices of short-lived particles, such as hyperons and charm/bottom hadrons that decay within millimeters of their production point.

In addition to these, they offer high stopping power along with excellent stability and durability as well as resistance to environmental conditions making them reliable detectors for long-term experiments. These characteristics make nuclear emulsions especially valuable in high energy physics experiments, particularly for studying nuclear fragmentation, particle production mechanisms and short-lived exotic particles.

In spite of their many advantages, nuclear emulsion detectors are associated with certain limitations. They lack real-time data acquisition and require time-consuming development and scanning that makes them unsuitable for high-rate or online experiments. Their ionization measurement range is limited which can reduce the precision of charge identification. They are also sensitive to environmental conditions such as temperature, humidity and light that must be carefully controlled to ensure data quality. Emulsion plates are also single-use and have a relatively small detection volume increasing the effort required for extensive studies.

2A.9 Experimental Data Details

2A.9.1 Exposure of the emulsion plates

Stacks of emulsion plates were hoizontally exposed to ^{16}O beam at an energy of 60 A GeV at CERN SPS [9]. The specifications of the emulsion plates, exposure conditions and other technical parameters are summarized in Table 2A.2.

Table 2A.2: Exposure details for ^{16}O beam interaction with emulsion plates.

Incident beam	Energy	Place of exposure	Type of emulsion	Dimension	Flux of incident particles
^{16}O	60 A GeV	CERN SPS, Switzerland	Illford G5	$18 \times 7 \times 0.06\ cm^3$	1×10^3 ions per cm^2

2A.9.2 Scanning and events selection

Interactions were identified after 1 cm from the leading edge of each emulsion plate. Event scanning was performed manually using the along-the-track method under a microscope. Preliminary scanning was typically carried out with a 10× objective lens in conjunction with a 20× eyepiece. Each event was observed by at least two independent scanners to ensure accuracy and minimize subjective bias.

Only events meeting the following criteria were selected for further analysis:

- **Incident beam constraints:** The incident beam track must not deviate more than 3° from the main beam direction within the pellicle. This ensures the correct identification of projectile tracks.
- **Depth of vertex criteria:** Events located within 20 μm from the top or bottom surface of the pellicle are excluded to reduce track loss and minimize angular measurement errors.
- **Criteria of primary interaction:** The incident particle tracks are followed in the backward direction to verify that they originate from the beginning of the pellicle that confirms their identity as projectile tracks.
- **Criteria for rejection of events with carbon, nitrogen and oxygen (CNO):** Only events containing a significant number of heavily ionizing tracks, i.e., a total number of black and grey tracks $n_h > 8$ are chosen. This helps eliminate interactions involving ^{28}Si with light nuclei such as carbon, nitrogen or oxygen.

For our analysis, 250 events of ^{16}O-AgBr interactions at 60 A GeV have been chosen according to the above selection criteria. Here, the nuclear emulsion serves the purpose of both target and detector.

2A.9.3 Measurement

Each selected event was analyzed using a 100X oil-immersion objective. The emission angle (θ) for each track was determined by recording the coordinates of the interaction point (X_0, Y_0, Z_0), the coordinates at the end of the linear segment of each secondary

track (X_1, Y_1, Z_1), and a reference point on the incident beam (X_i, Y_i, Z_i). The measuring system integrated with the microscope offers a resolution of 1 μm along the X and Y axes and 0.5 μm along the Z axis.

2A.9.4 Pseudorapidity and multiplicity distribution

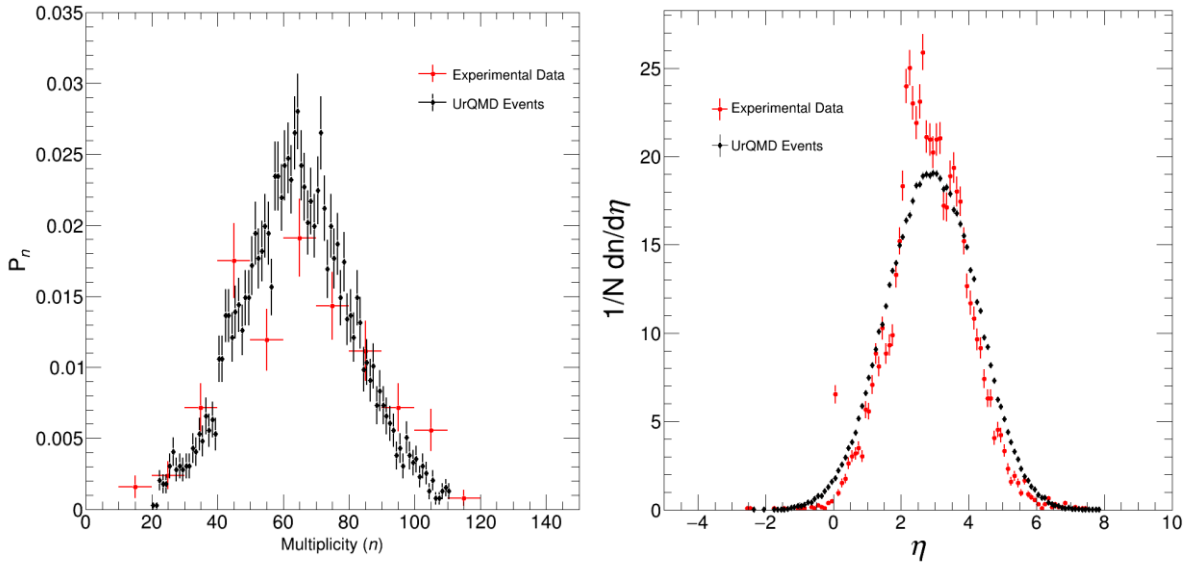

(a) (b)

Fig. 2A.1: (a) Multiplicity distribution and **(b)** Pseudorapidity distribution of shower particles in ^{16}O-AgBr interactions at 60 A GeV. The error bars represent statistical errors only.

In our analysis, only shower particles defined as secondary particles emitted from an interaction are considered. For each shower track, the pseudorapidity (η) is computed using the formula $\eta = -\ln\left[tan\left(\frac{\theta}{2}\right)\right]$. The precision in pseudorapidity meaasurements in the region of interest is approximately 0.1 pseudorapidity units [10-11]. Figure 2A.1(a) and Fig. 2A.1(b) represent multiplicity and pseudorapidity distribution of shower particles produced in ^{16}O-AgBr interactions at 60 A GeV respectively. Average multiplicity of our chosen events is 63.2 and the pseudorapidity distribution is centered at η_{center} = 2.25.

Chapter 2B

Monte Carlo Simulations of High Energy Interactions

2B.1 Introduction

Numerous theoretical and phenomenological models have been proposed to interpret the extensive experimental data from relativistic heavy-ion collisions. The overarching objectives are to develop a comprehensive theory that explains all existing observations and predicts the outcome of any conceivable experiment.

In order to achieve our goal, we have used the following two models in our analyses.

2B.2 EPOS3 Model

2B.2.1 Introduction

EPOS (Energy-conserving quantum mechanical approach, based on Partons, parton ladders, strings, Off-shell remnants, and Splitting of parton ladders) [12] is a sophisticated Monte Carlo event generator used for simulating high energy collisions. EPOS was initially developed in the early 2000s by physicists at the University of Frankfurt based on the Dual Parton Model (DPM) [13], a phenomenological framework describing hadron and nuclear interactions at high energies. In the late 2000s, it was further enhanced by incorporating the Parton-based Gribov-Regge Theory (PBGRT) [14], a more fundamental approach that expanded its simulation capabilities. EPOS offers high configurability in terms of event types, parameter settings and event timing, making it well-suited for applications such as machine learning training and the generation of synthetic datasets for detailed physical investigations.

EPOS is designed to simulate hard processes including heavy quark and prompt photon production and to study the properties of QGP [15]. It integrates multiple theoretical components such as quantum treatment of interactions, perturbative calculations, string fragmentation, and generates real events with both high-p_T jets and low-p_T particles to produce complete events rather than just inclusive spectra. EPOS reproduces a wide range of observables from proton-proton, proton-nucleus and nucleus-nucleus collisions at different energies [16-17].

EPOS3 [18] (used in this study) is a more advanced and comprehensive version of EPOS. It incorporates 3+1D viscous hydrodynamic evolution of the bulk matter, along

with improved core-corona separation and enhanced jet quenching mechanisms. This makes it more suitable for studying QGP properties.

2B.2.2 Parton-based Gribov-Regge Theory

Parton-based Gribov-Regge Theory (PBGRT) [19] is a theoretical framework that unifies the parton model and Gribov-Regge theory to describe high energy hadron-hadron interactions. The parton model suggests that hadrons are composed of point-like constituents called partons, which carry the momentum of the hadron and interact with each other through the exchange of gluons. The Gribov-Regge theory postulates that hadrons interact through the exchange of Regge trajectories, which represent families of particles with the same quantum numbers but different masses. PBGRT combines the parton model with the Gribov-Regge theory by treating partons as the constituents of Regge trajectories and as a result, provides a comprehensive description of scattering processes. PBGRT successfully explains various observables such as total, elastic and diffractive cross sections in hadron-hadron collisions and is also used to study particle production in high energy collisions.

2B.2.3 Mechanism of event generation in EPOS3

EPOS3 is a Monte Carlo event generator that produces events through a sequence of theoretical and computational steps simulating the full space-time evolution of the system from initial parton production to final hadronic output.

The main steps of the event generation process are as follows:

i. The initial conditions of the collision are specified such as the energy and momentum of the colliding particles.

ii. The PBGRT framework is used to model the initial stages of the collision. This involves the creation of partons from the colliding hadrons.

iii. The pQCD part of the PBGRT framework is used to model the interactions of the partons. This includes the scattering of partons, the production of new partons and the fragmentation of partons into hadrons.

iv. The non-perturbative part of the PBGRT framework divides the system into high- and low-string-density regions referred to as the core and corona respectively. The core undergoes a 3+1D viscous hydrodynamic evolution and hadronizes via the Cooper-Frye formalism. The corona hadronizes via string fragmentation and produces jets.

v. After hadronization, the system undergoes a hadronic cascade using the UrQMD (Ultra-Relativistic Quantum Molecular Dynamics) model [20-21], which simulates the subsequent evolution of the collision. This stage continues until the system reaches chemical freeze-out followed by kinetic freeze-out.

vi. The output of the simulation is a list of particles produced in the collision. This list includes each particle's type, momentum, position, etc.

A detailed description of the different phases involved in the event generation process is provided below [12, 18].

- **Initial state: parton interaction and multiple Scattering**

The theoretical framework of EPOS3 model emphasizes a sophisticated approach to both hadron-hadron scattering and the initial stages of ultra-relativistic collisions. This is particularly significant in understanding the possible parton-hadron phase transitions. EPOS3 model employs a combined methodology that integrates Gribov-Regge theory with the eikonalized parton model to ensure an accurate representation of the initial interactions occurring immediately after a collision. This approach maintains conservation laws and treats all subsequent interactions uniformly.

In this approach, an individual scattering is termed as a Pomeron. For a given pomeron, the corresponding chain of partons is treated as parton ladder which may be considered as a longitudinal color field or a flux tube, carrying transverse kinks from the initial hard scatterings [19]. In a collision, many elementary parton-parton hard scatterings form a large number of flux tubes that expand and are fragmented into string segments.

- **Core-corona separation and hydrodynamic evolution**

EPOS3 dynamically separates string segments into core and corona based on string density. The higher string density forms core which undergoes a 3+1D viscous hydrodynamic evolution with a shear viscosity to entropy density ratio η/s = 0.08. In this core region, no jet partons are expected to escape and hadronization occurs via the Cooper-Frye formalism. This collective expansion takes place till soft hadrons (low-p_T particles) freeze-out. In contrast, the lower string density constitutes corona, consisting of partons that do not undergo full thermalization and where we can expect the escape of jet partons. Such string segments having high transverse momentum that are close to the surface leave the bulk matter and hadronize directly. Rest of the string segments which have enough energy to escape the bulk matter constitute semihard or intermediate-p_T particles and considered as corona particle. At the time of escaping, these segments may pick up quarks or antiquarks from the bulk matter inheriting the imprints of its properties.

- **Hadronization**

In EPOS3, hadronization follows two distinct mechanisms for the core and the corona.

  - **Core hadronization**

    The core undergoes a 3+1D viscous relativistic hydrodynamic expansion, governed by an equation of state that includes a crossover transition from QGP to hadronic matter. As the system expands and cools, it eventually reaches the hadronization temperature T_H. At this stage, the Cooper-Frye formula is applied at the freeze-out surface to convert the energy-momentum tensor of the fluid into hadrons. This approach ensures that the produced hadrons inherit the collective flow developed during the hydrodynamic evolution.

  - **Corona hadronization**

    The corona consists of partons that do not undergo full thermalization and instead hadronize through the Schwinger mechanism using a string fragmentation approach. This is a non-equilibrium process, where the hadronization occurs via string breaking.

- **Final state interactions**

After hadronization, the system undergoes a hadronic cascade simulated by the UrQMD model, which describes the evolution of the collision in the hadronic phase [20-21]. This stage includes elastic and inelastic interactions among hadrons, as well as hadronic decays and the production of new hadrons. The evolution continues until the system reaches chemical freeze-out, where inelastic collisions cease and particle yields are fixed, followed by kinetic freeze-out, where elastic collisions stop and the momentum distributions of particles are frozen.

- **Event output**

In the final state of the system, the x, y and z components of momentum of identified hadrons including pions, kaons and protons are generated, and from this, observables such as flow coefficients (v_n), rapidity distributions and transverse momentum spectra are derived to characterize the dynamics of the collision. These predictions are then compared to experimental data from LHC, RHIC and cosmic ray experiments to validate the accuracy and reliability of the model.

2B.2.4 Parameters used to configure EPOS3 event generator

The important parameters used for EPOS3 event generations are:

- **Beam energy:** The beam energy is the energy of the colliding hadrons. This parameter is used to set the scale of the simulation.
- **Particle type:** The particle type specifies the type of hadrons that are simulated. The EPOS3 event generator can simulate a variety of hadrons, including protons, neutrons, pions, kaons and strange particles.
- **Impact parameter:** The impact parameter is the distance between the centers of the colliding hadrons. This parameter determines the overlap between the hadrons and, therefore, the number of particles that are produced in the collision.
- **Parton distribution functions (PDFs):** PDFs represent the momentum distribution of partons inside hadrons. EPOS3 uses different PDFs based on hadron type and collision energy. For nuclei, modified PDFs (nPDFs) are used to account for the influence of surrounding nucleons within the nucleus.

- **Parton scattering cross sections:** The parton scattering cross sections are the probabilities for partons to scatter off each other. The EPOS3 event generator uses different parton scattering cross sections for different types of partons and for different energies. It includes improved multiple scattering with gluon-saturation effects, more refined treatment of hard scatterings and detailed saturation mechanism.

These parameters are only a few among the complete set used in EPOS3 to control various simulation aspects, such as precision and the number of generated particles.

2B.2.5 Advantages of EPOS3 event generator

The most unique feature of EPOS3 model is to use a common theoretical scheme for the particle production in proton-proton, proton-nucleus and nucleus-nucleus collisions. Unlike many other Monte Carlo event generators, it produces real event which does not introduce any test particles and all kinds of fluctuations are treated on the basis of event-by-event fluctuations. EPOS3 is capable of simulating the entire event evolution from initial conditions to final hadronic interactions rather than focusing on just a specific phase of the collision. It incorporates full 3+1D viscous hydrodynamic evolution on an event-by-event basis capturing essential fluctuations and collective effects. The core-corona approach separates high-density and low-density regions and enables realistic modeling of QGP formation and hadronization dynamics. This framework naturally produces elliptic and triangular flow patterns observed in heavy-ion collisions. Moreover, it efficiently generates large volumes of events, which is particularly beneficial for high-statistics analyses and machine learning applications. EPOS3 is well-tuned to reproduce experimental results from RHIC, LHC and cosmic-ray experiments and serves as a reliable tool for predicting collision outcomes.

Overall, EPOS3 is a relatively accurate, fast, flexible and highly configurable Monte Carlo event generator that can be used to study a wide variety of high energy collisions.

2B.2.6 Data description

Table 2B.1: Details of the simulated events used in this thesis, generated using the EPOS3 model.

Inter-action Type	Center-of-Mass Energy (TeV)	Event Type	Sample Size (Approximately)
pp	0.9	Minimum-bias events without hydrodynamical evolution of particles	3 million
pp	0.9	Minimum-bias events with hydrodynamical evolution of particles	3 million
pp	2.76	Minimum-bias events without hydrodynamical evolution of particles	3 million
pp	2.76	Minimum-bias events with hydrodynamical evolution of particles	3 million
pp	7	Minimum-bias events without hydrodynamical evolution of particles	3 million
pp	7	Minimum-bias events with hydrodynamical evolution of particles	3 million
pp	13	Minimum-bias events with hydrodynamical evolution of particles	3 million
pPb	5.02	Minimum-bias events with hydrodynamical evolution of particles	3 million

2B.2.7 Data validation

It is essential to validate EPOS3 generated event samples against experimental data to ensure the accuracy and reliability of its predictions. In this thesis, we perform a detailed comparison of transverse momentum and pseudorapidity spectra between EPOS3 simulations and experimental results.

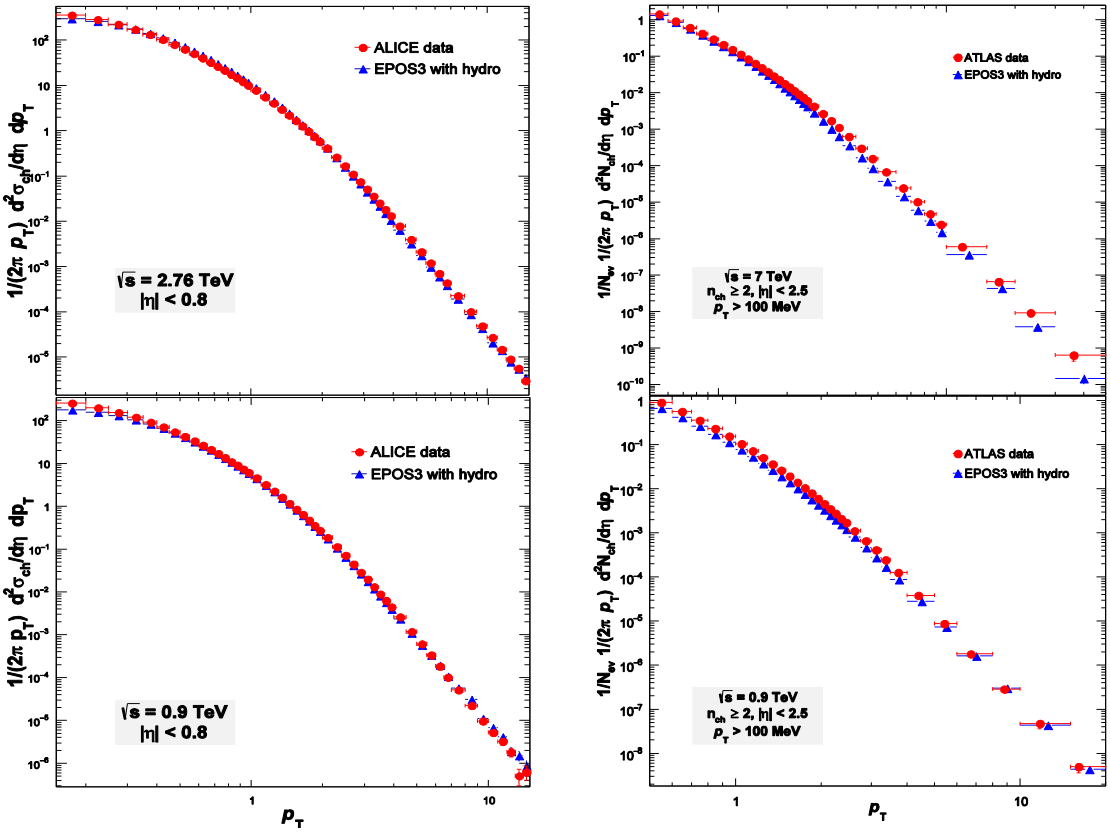

(a) (b)

Fig. 2B.1: **(a)** Differential cross section of charged particle as a function of p_T from EPOS3 with hydro generated minimum-bias events in pp collisions at $\sqrt{s}$ = 2.76 (upper panel) and 0.9 TeV (lower panel), compared to ALICE data [22]. **(b)** Charged-particle multiplicities as a function of p_T from the same EPOS3 events in pp collisions at $\sqrt{s}$ = 7 TeV (upper panel) and 0.9 TeV (lower panel) compared to ATLAS data [23].

- **Validation of simulated pp and pPb events at different energies based on p_T distribution:**

We have measured p_T-spectrum of EPOS3 generated with hydro minimum-bias pp events at $\sqrt{s}$ = 2.76 TeV and 0.9 TeV and compared to ALICE data [22] and also the same at $\sqrt{s}$ = 7 TeV and 0.9 TeV and compared to ATLAS data [23] in Fig. 2B.1(a) and Fig. 2B.1(b) respectively. Figure 2B.2 shows the invariant yields of charged-particles as a function of p_T for EPOS3 simulated with hydro pp events at $\sqrt{s}$ = 13 TeV (left) and pPb collisions at $\sqrt{S_{NN}}$ = 5.02 TeV (right) compared to ALICE data [24-25]. Red and blue points correspond to the experimental data and

EPOS3 simulated events. We observe that both EPOS3 calculations and experimental measurements exhibit a similar pattern. The figures clearly demonstrate that the p_T-spectrum has been successfully reproduced by the EPOS3 simulated events at the chosen energies.

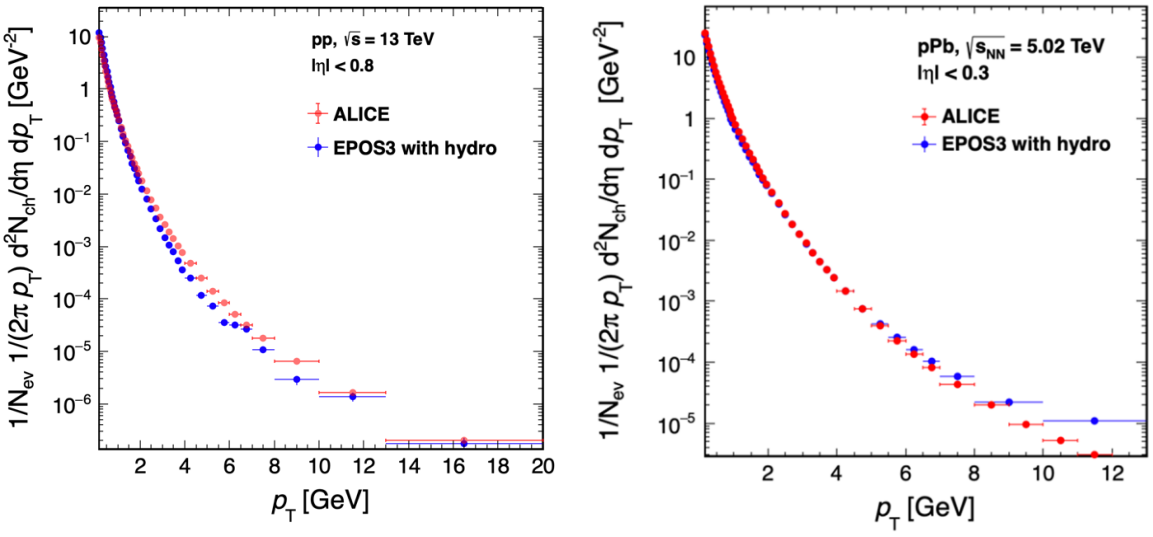

Fig. 2B.2: Charged-particle invariant yields as a function of p_T in pp collisions at $\sqrt{s}$ = 13 TeV (left) and in pPb collisions at $\sqrt{S_{NN}}$ = 5.02 TeV (right) compared to ALICE data [24-25].

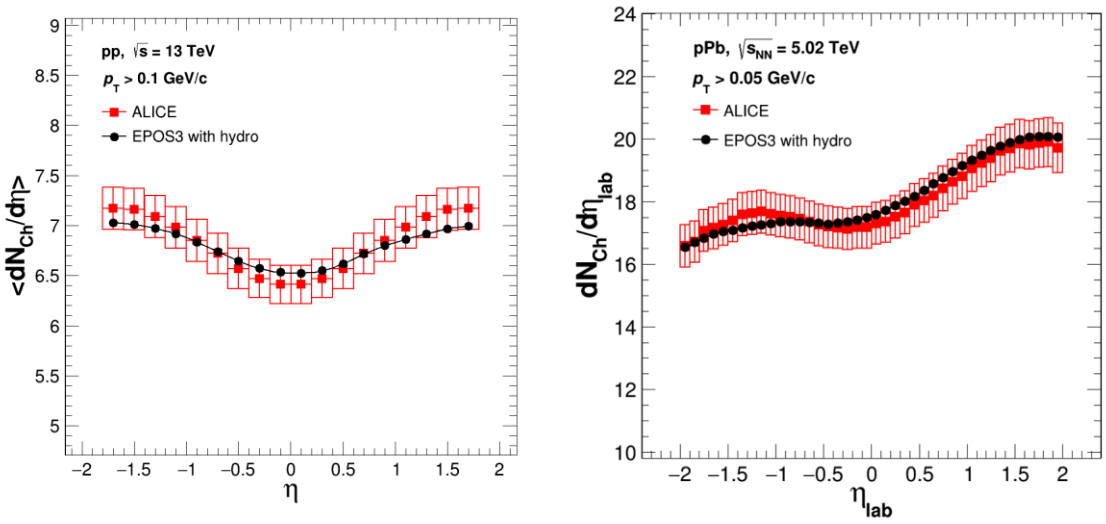

Fig. 2B.3: (Average) Pseudorapidity density of charged particle in pp collisions at $\sqrt{s}$ = 13 TeV (left) and in pPb collisions at $\sqrt{S_{NN}}$ = 5.02 TeV (right) compared to ALICE data [24, 26].

- **Validation of simulated pp events at $\sqrt{s}$ = 13 TeV and pPb events based on η-distribution:**

We have also validated the pseudorapidity distributions of charged particle against experimental data, especially for asymmetric pPb collisions. Average pseudorapidity density and pseudorapidity density of charged particles has been plotted in Fig. 2B.3 for EPOS3 simulated with hydro pp events at $\sqrt{s}$ = 13 TeV (left) and pPb collisions at $\sqrt{S_{NN}}$ = 5.02 TeV (right). Red and black points correspond to the ALICE data and EPOS3 simulated events. Compared results reflect that EPOS3 simulated events agreed well with the experimental measurements in the chosen kinematic intervals [24, 26].

The successful validation of the generated events ensures that EPOS3 can reproduce pp and pPb collisions at the chosen energies. Therefore, we use EPOS3 Monte Carlo event generator in this thesis for three distinct studies: forward-backward multiplicity and momentum correlation analysis, investigation of fractal characteristics and chaotic behavior of multiparticle production in high energy collisions.

2B.3 UrQMD Model

2B.3.1 Introduction

The Ultra-Relativistic Quantum Molecular Dynamics (UrQMD) [20] model is a widely used microscopic transport approach designed to simulate heavy-ion collisions across a broad range of beam energies typically from a few tens of MeV/nucleon up to several TeV/nucleon. It provides a comprehensive framework for studying the dynamics of hadronic matter including particle production, rescattering and the space-time evolution of the system, and is therefore applicable to experiments at facilities such as GSI, AGS, SPS, RHIC and even the LHC when coupled with hybrid hydrodynamic framework.

UrQMD operates through a combination of classical propagation, binary collisions and resonance formation and decay. It describes hadronic interactions using known

cross-sections and incorporates the excitation of resonances and the formation of string-like objects at higher energies. The model accounts for both soft and hard scattering processes through hadronic interactions and string excitations. While the standard UrQMD model is purely hadronic, its hybrid extensions incorporate a hydrodynamic phase that enables it to investigate the transition from hadronic to partonic matter in high energy collisions.

UrQMD v3.4 has shown strong agreement with experimental data across various collision systems and energy scales. It successfully describes the ALICE experimental pseudorapidity distribution in $PbPb$ interactions at $\sqrt{s_{NN}}$ = 2.76 TeV [27] and also reproduces the transverse momentum spectra of charged pions in inelastic proton-proton interactions reported by the NA61/SHINE Collaboration [28]. The consistency with experimental observations confirms the effectiveness of the model in simulating hadronic interactions and particle production across a wide range of collision energies and system.

2B.3.2 Working principal of UrQMD

Rooted in the microscopic transport approach, the model describes particle propagation through space while incorporating probabilistic rules for scattering, decay and resonance formation. These interactions are governed by known cross-sections and dynamical processes and ensure a realistic simulation of heavy-ion collisions across different energy scales. UrQMD solves the Boltzmann transport equation to model the space-time evolution of hadronic matter and provides a dynamic description of the collision process without assuming local equilibrium. This approach allows for the simulation of the entire nuclear collision process from the initial state of the colliding nuclei to the final state of the produced particles. It uses PYTHIA model [29] to describe the initial stage of the collision, where high energy strings are excited and subsequently fragment into hadrons. The model also utilizes PYTHIA routines for handling hard scatterings: initializing positions and momenta of nucleons, simulating hard scattering events to generate high energy partons, evolving parton showers and converting partons into hadrons through hadronization, before feeding these hadrons back into the UrQMD framework for further interaction simulations. For soft scatterings, UrQMD sets up initial conditions for colliding nuclei, propagates nucleons through space, determines

binary collisions based on predefined cross-sections, handles resonance formation and decay and simulates secondary interactions leading to system thermalization.

The main steps of the event generation process are as follows:

i. **Initialization:** Nucleon positions are sampled using a Woods-Saxon distribution and momenta are assigned via a Fermi distribution.
ii. **Nucleon propagation:** Nucleons and hadrons move according to classical Hamiltonian dynamics in phase space.
iii. **Collision dynamics:** Binary collisions occur when particles approach within a certain range, with outcomes determined by impact parameter and interaction cross-sections.
iv. **Soft and hard scatterings:** Soft interactions follow hadronic transport theory; hard scatterings are modeled using PYTHIA for parton dynamics and hadronization.
v. **Resonance formation and decay:** Resonances form and decay via the Breit-Wigner formalism contributing to particle production.
vi. **Secondary interactions and thermalization:** Particles undergo rescattering and medium effects leading to the system thermalization.
vii. **Hadronic freeze-out:** As the system expands and densities decrease, interactions cease and hadrons stream freely toward detectors. The final particle spectra are recorded for comparison with experimental data.

2B.3.3 Advantages of UrQMD model

UrQMD provides a consistent hadronic transport framework capable of simulating heavy-ion collisions from low energy nuclear reactions to ultra-relativistic interactions at RHIC and LHC. Its unique strength lies in its microscopic treatment of hadron interactions across all energies, with optional hybrid extensions to include hydrodynamic evolution at higher energies. The model incorporates a broad spectrum of hadronic species including more than 50 baryon and 45 meson types. It accounts for various interaction channels such as baryon-baryon, meson-baryon and meson-meson collisions including resonance formation and decay processes. UrQMD effectively describes soft hadronic processes through transport dynamics. At higher energies

($\sqrt{S_{NN}} \geq$ 10-20 GeV), it incorporates embedded PYTHIA routines to model hard scattering events. It also includes essential features such as secondary interactions, multiple rescattering processes and in-medium modifications, which significantly affect the evolution of final-state particles. These mechanisms are essential for modeling the dense nuclear environment and for capturing the resulting changes in momentum distributions, flow patterns and correlation structures. It can be coupled with hydrodynamic approaches or parton cascade models for hybrid simulations, enhancing its applicability in different physics scenarios.

The latest version, UrQMD v3.4, introduces significant advancements, including an integrated hybrid approach with hydrodynamic evolution, refined treatment of high energy processes and extended particle species coverage. These enhancements improve the model's precision and make UrQMD a robust and versatile framework for studying nuclear and hadronic collision across a broad range of beam energies.

2B.3.4 Data description

For our study, 4000 ^{16}O-AgBr events at 60 A GeV were generated using the latest version of UrQMD transport model, i.e., UrQMD v3.4 [30]. We have used the following key parameters: for the Field-Feynman fragmentation function $f(z) \propto z^{-a}(1-z)^{b}$, parameter a = 1.0d0 and parameter b = 2.0d0; for the phase space, PhaseSpace:pTHatMinDiverge = 1; and for the momentum cut off in hard scattering, $Q^2 > 2.25\ (GeV/c)^2$.

2B.3.5 Data validation

Figure 2A.1(a) and 2A.1(b) respectively show the multiplicity and pseudorapidity distributions of shower particles produced in UrQMD generated ^{16}O-AgBr events at 60 A GeV, compared with corresponding experimental data. The simulated and experimental results exhibit similar trends, which validate UrQMD generated events. However, the pseudorapidity distribution from the UrQMD model appears narrower than that of the experimental data and underestimates the central region. Nevertheless, considering the overall qualitative agreement, the UrQMD generated events have been used in this thesis to study chaos in multiparticle production through the erraticity moment method.

References

[1] C. M. G. Lattes *et al.*, Nature **159**, 694-697 (1947).

[2] A. Ariga, T. Ariga, G. De Lellis, A. Ereditato, K. Niwa. Nuclear Emulsions. In: C. W. Fabjan, H. Schopper (eds.), Particle Physics Reference Library. Volume 2: Detectors for Particles and Radiation, Springer International Publishing, Cham, 383-438 (2020). https://doi.org/10.1007/978-3-030-35318-6_9.

[3] M. Basu *et al.*, Proc. 20th Int. Cosmic Ray Conf. (Moscow), 6, 444 (1987).

[4] R. W. Gurney and N. F. Mott, Proc. R. Soc. A **164**, 151-167 (1938).

[5] A. E. S. Green, Nuclear Physics, McGraw-Hill Book Company, New York, 1955.

[6] L. Voyvodic, Bristol Conf. Rep. Dec. 1951.

[7] L. Voyvodic and E. Pickup, Phys. Rev. **85**, 91-95 (1952).

[8] C.F. Powell, P.H. Fowler and D.H. Perkins, The Study of Elementary Particles by the Photographic Method, Pergamon Press, New York, 1959.

[9] D. Ghosh, A. Deb, S. R. Sahoo, P. K. Haldar, Md. A. K. Jafry, Nucl. Phys. A **707**(1-2), 213-223 (2002).

[10] D. Chanda *et al.*, Phys. Rev. C **71**(3), 034904 (2005).

[11] G. Bhoumik, S. Bhattacharyya, A. Deb, D. Ghosh, Eur. Phys. J. A **52**, 196 (2016).

[12] K. Werner *et al.*, Phys. Rev. C **82**, 044904 (2010).

[13] A. Capella *et al.*, Phys. Rep. **236**, 225-329 (1994).

[14] K. Werner, F.-M. Liu, and T. Pierog, Phys. Rev. C **74**, 044902 (2006).

[15] L. C. P. Van Hove, *Theoretical prediction of a new state of matter, the "quark-gluon plasma" (also called "quark matter")*, Proc. 17th Int. Symp. on Multiparticle Dynamics, Seewinkel, Austria, (1987).

[16] S. Porteboeuf, T. Pierog and K. Werner, arXiv preprint arXiv:1006.2967 (2010).

[17] B. Guiot and K. Werner, J. Phys.: Conf. Ser. 589, 012028 (2015).

[18] K. Werner, B. Guiot, Iu. Karpenko, and T. Pierog, Phys. Rev. C **89**, 064903 (2014).

[19] H. J. Drescher *et al*., Phys. Rep. **350** (2–4), 93-289 (2001).

[20] M. Bleicher *et al.*, J. Phys. G: Nucl. Part. Phys. **25**(9), 1859–1896 (1999).

[21] H. Petersen *et al*., Phys. Rev. C **78**, 044901 (2008).

[22] B. Abelev *et al.* (ALICE Collaboration), Eur. Phys. J. C **73**, 2662 (2013).

[23] G. Aad *et al.* (ATLAS Collaboration), New J. Phys. **13**, 053033 (2011).

[24] J. Adam *et al.* (ALICE Collaboration), Phys. Lett. B **753**, 319-329 (2016).

[25] B. Abelev *et al.* (ALICE Collaboration), Eur. Phys. J. C **74**, 3054, (2014).

[26] B. Abelev *et al.* (ALICE Collaboration) Phys. Rev. Lett. **110**, 032301 (2013).

[27] N. Hussain, B. Bhattacharjee, Phys. Rev. C **96**(2), 024903 (2017).

[28] V. Ozvenchuk, A. Rybicki, Nucl. Phys. A **973**, 104–115 (2018).

[29] T. Sjöstrand, Comput. Phys. Commun. **82**(1), 74-89 (1994).

[30] The UrQMD Frankfurt Duke Nantes user guide. (The UrQMD group, 2014). https://itp.uni-frankfurt.de/~bleicher/userguide.pdf. Accessed on 1st September 2024.

Chapter – 3

Study of Forward-Backward Correlations at the LHC Energies

3.1 Introduction

The study of correlations among charged particles (i.e.-pions, kaons and protons) produced in different pseudorapidity (η) regions in ultra-relativistic nuclear collision may provide an understanding of multi-particle production mechanism. More differential tools like forward-backward (FB) correlations between particles from two distinct phase spaces further enhance our cognizance.

In heavy-ion collisions, the initial energy density fluctuates strongly from event-to-event, which in turn influences the space-time evolution of the produced medium in the final state. The substantial initial-state fluctuations give rise to observed long-range correlations (LRCs) between final-state particles, typically appearing as correlations between multiplicity densities in different η windows [1]. Additionally, longitudinal multiplicity correlations also include short-range correlations (SRCs), which are confined to a smaller η range and arise from sources such as single jets, minijets and resonance decays. FB correlations serve as a powerful tool to distinguish between LRC and SRC components [2], advancing knowledge of the basic dynamics governing particle production in high energy hadron and nuclear collisions. Pairs of pseudorapidity intervals of equal size, symmetrically located on either side of the collision vertex, are designated as forward (in the beam direction) and backward (opposite to the beam direction) windows. Event-by-event variations of different observables within these FB windows can be used to construct FB correlation strengths [2-4].

Several experimental studies on FB correlations have been conducted for different collision systems including electron-positron (e^+e^-), proton-proton (pp), proton-antiproton ($p\bar{p}$), proton-nucleus (pA) and nucleus-nucleus (AA) [3, 5-15]. The ATLAS [7] and ALICE [15] Collaborations at the LHC have reported strong FB correlations in pp collisions at $\sqrt{s}$ = 0.9, 2.76 and 7 TeV. A detailed investigation of FB multiplicity correlations is carried out by analyzing asymmetry in terms of the dynamical fluctuation parameter σ_c^2 in forward-backward pseudorapidity windows for both ring-like and jet-like events of ^{16}O-AgBr interactions at 60 A GeV [16]. Their study shows σ_c^2 values significantly greater than 1 for both ring-like and jet-like events, highlighting strong FB multiplicity correlations in the multiparticle production mechanism of ring-

like and jet-like events. However, no noticeable difference was observed between two types of event structures.

Various theoretical models have been proposed to explain the experimental results on FB correlations. The dual parton model [17, 18] and the quark-gluon string model [19] predicted the existence of long-range correlations by considering multiple parton-parton interactions. The Monte Carlo implementation of QGSM [20], which successfully described ALICE data [15] on FB correlations, suggested that the FB correlations in pp collisions at different center-of-mass energies arises from the superposition of various multistring processes with different mean multiplicities. The string fusion model [21] explored long-range correlations by considering interactions between strings, highlighting different types of FB correlations as mentioned above [22]. Additionally, the Monte Carlo version of SFM provided a reasonable reproduction of LHC data in both hadronic and nuclear collisions [23, 24]. FB correlations have also been investigated through the string percolation mechanism in pp collisions [25]. Studies within the CGC framework [26-29] revealed that initial-state correlations and density fluctuations contribute to the observed long-range correlations among final-state particles, predicting a centrality-dependent increase in LRC for heavy-ion collisions [14].

The EPOS3 model, incorporating an inbuilt hydrodynamic feature [30, 31], has successfully described ALICE data [32] for charged-particle flow. However, results from the ATLAS experiment at the LHC show that EPOS simulations underestimate the strength of FB correlations in pp collisions at 13 TeV [1]. Notably, the hydrodynamic component of the EPOS model remains unexplored and has not been tested for all the available energies at the LHC. Consequently, despite extensive experimental and theoretical efforts, the underlying physics of FB correlations remains inconclusive. Furthermore, recent findings on high-multiplicity events in small systems (pp/pA), which resemble many heavy-ion outcomes, demand further studies in this area.

In this chapter, we have used EPOS3 generated events with and without hydrodynamical evolution of particles (referred as “with and without hydro” in rest of the texts) to study the FB correlations in several pseudorapidity windows in pp collisions at $\sqrt{s}$ = 0.9, 2.76, 7 and 13 TeV and pPb collisions at $\sqrt{s_{NN}}$ = 5.02 TeV.

3.2 Forward-Backward Charged-Particle Correlation Strength

In general, FB correlations between produced particles can be categorized into three main types [33]:

(i) $n - n$, the correlation between charged-particle multiplicities
(ii) $p_T - p_T$, the correlation between mean or summed transverse momenta of charged particles
(iii) $p_T - n$, the correlation between mean or summed transverse momenta in one pseudorapidity interval and the multiplicity of charged particles in another pseudorapidity interval

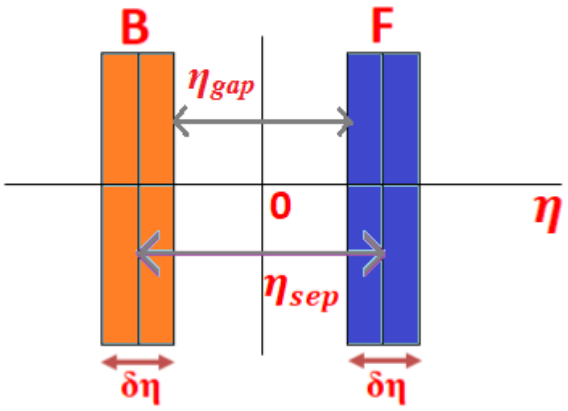

Fig. 3.1: Construction of forward and backward window.

The FB correlation strength is measured in a coordinate system with origin $\eta = 0$ which is always located at midrapidity. Two symmetric, non-overlapping pseudorapidity intervals are selected, one in the forward ($\eta > 0$) and another in the backward hemispheres ($\eta < 0$) in the center-of-mass system. Figure 3.1 shows forward and backward window construction where η_{gap} being the gap between the window pairs, η_{sep} being the distance between the window centers and $\delta\eta$ being the width of each window.

The FB correlation strength can be obtained from a linear regression analysis of the average charged-particle multiplicity in the backward hemisphere ($\eta < 0$), $\langle N_b \rangle_{N_f}$, as a function of the event multiplicity in the forward hemisphere ($\eta > 0$), N_f, such that,

$$\langle N_b \rangle_{N_f} = a + b_{corr}(mult) N_f, \tag{3.1}$$

where a is a constant and the slope of the straight line $b_{corr}(mult)$ measures the multiplicity correlation strength [5, 17]. If linear relation of Eq. (3.1) holds, then $b_{corr}(mult)$ can be estimated using the following formula of Pearson correlation coefficient:

$$b_{corr}(mult) = \frac{\langle N_f N_b \rangle - \langle N_f \rangle \langle N_b \rangle}{\langle N_f^2 \rangle - \langle N_f \rangle^2} = \frac{D_{fb}^2}{D_{ff}^2}. \tag{3.2}$$

In Eq. (3.2), D_{fb}^2 (covariance) and D_{ff}^2 (variance) are the forward-backward and forward-forward dispersions, respectively [2, 17].

Since the charged-particle multiplicity is an extensive quantity, the FB multiplicity correlation strength is affected by the so-called "volume fluctuations" which originate from event-by-event fluctuations of the number of participating nucleons. To avoid such fluctuations, we can consider intensive observables like the sum of the absolute transverse momentum of particles within the observation windows. Similar to the multiplicity correlation, forward-backward summed-p_T correlation strength can be extracted using the following formula:

$$b_{corr}\left(\sum p_T\right) = \frac{\langle \sum p_{Tf} \sum p_{Tb} \rangle - \langle \sum p_{Tf} \rangle \langle \sum p_{Tb} \rangle}{\left\langle \left(\sum p_{Tf} \right)^2 \right\rangle - \langle \sum p_{Tf} \rangle^2}, \tag{3.3}$$

where $\sum p_{T_f}$ and $\sum p_{T_b}$ are the event summed transverse momentum in forward and backward window respectively.

Similarly, the correlation strength between mean or summed transverse momenta and the charged-particle multiplicity can also be described following the formula of Pearson correlation coefficient. In this thesis, however, we have focused on the first two types of FB correlations in detail.

3.3 Details of Analyzed Events

In this study, simulated data are obtained using the EPOS3 [30] event generator, which employs a hybrid model incorporating parton-based multiple scattering and

hydrodynamic evolution. A detailed description of the generator is given in Chapter 2B.2.

We have used 3 million minimum-bias pp events for center-of-mass energies 0.9, 2.76 and 7 TeV, for each of the options, with and without hydro, 3 million minimum-bias with hydro pp events at $\sqrt{s}$ = 13 TeV and pPb events at $\sqrt{s_{NN}}$ = 5.02 TeV. On top of the minimum-bias analysis, a more differential approach has been introduced by taking particles coming from either the core or corona for pp events at center-of-mass energy 13 TeV and for pPb events, and we have varied certain model parameters in order to achieve this.

3.4 FB Multiplicity and Momentum Correlations in EPOS3 Generated pp Events at $\sqrt{s} = 0.9, 2.76$ *and* 7 *TeV*

We have plotted forward multiplicity versus backward multiplicity taking window width $\delta\eta$ = 0.8 and $\eta_{gap} = 0$ for EPOS3 simulated pp events at $\sqrt{s} = 7$ TeV in Fig. 3.2. It shows that charged particles are not distributed isotropically in forward and backward directions. We want to study if there is any correlation between the particles emitted in forward direction with the particles emitted in backward direction. To check the relationship between average charged-particle multiplicity in the backward window ($\langle N_b \rangle_{N_f}$) and the charged-particle multiplicity in the forward window (N_f), we have plotted $\langle N_b \rangle_{N_f}$ as a function of N_f taking window width $\delta\eta$ = 0.6 and η_{gap}= 0.4 for EPOS3 simulated pp events at $\sqrt{s}$ = 0.9, 2.76 and 7 TeV in Fig. 3.3. Here, left and right panels represent EPOS3 simulated pp events considering without hydro and with hydro respectively. The data points exhibit linear behavior, as described in Eq. (3.1). The linear fits have been done and shown by the red lines in all panels in Fig. 3.3. Slope of these lines actually measure the correlation strength between multiplicities in forward and backward windows.

Henceforth, we have applied the Pearson correlation coefficient formulas described in Eq. (3.2) and Eq. (3.3) to compute FB multiplicity and momentum correlation strengths, respectively.

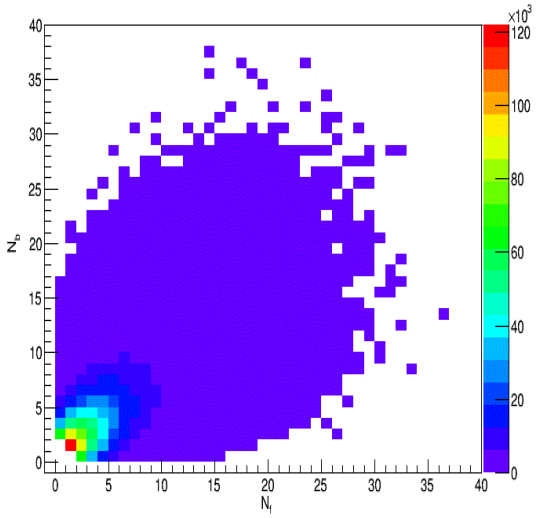

Fig. 3.2: Illustrative example of forward versus backward multiplicity for EPOS3 simulated pp events at $\sqrt{s} = 7$ TeV with window width $\delta\eta$ = 0.8 and $\eta_{gap} = 0$.

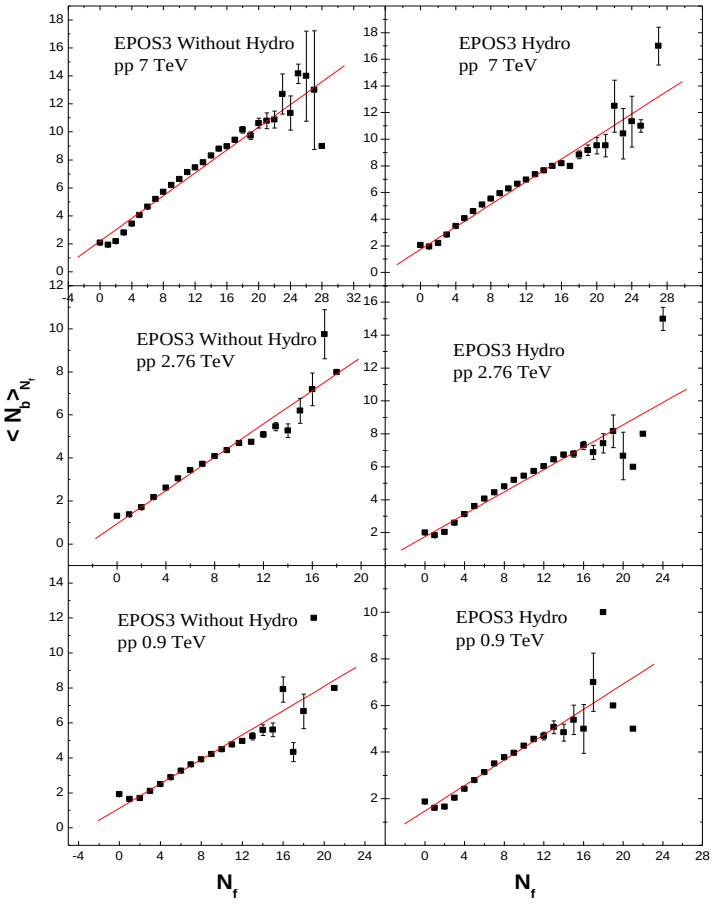

Fig. 3.3: Variation of $< N_b >_{N_f}$ with N_f for window width $\delta\eta$ = 0.6 and η_{gap} = 0.4 at three center-of-mass energies of EPOS3 simulated pp Events. Red lines represent the corresponding linear fits.

3.4.1 Analysis considering ALICE kinematics:

In ALICE [15] kinematics events are selected with a minimum of two charged particles in the kinematic interval $0.3 < p_T < 1.5$ (GeV/c) and $|\eta| < 0.8$. FB Correlations are studied as a function of the gap between the windows (η_{gap}). Three different values of η_{gap} are taken, η_{gap} = 0, 0.4 and 0.8. For each value of η_{gap}, we have considered four different values of δη, i.e., $\delta\eta = 0.2, 0.4, 0.6\ and\ 0.8$. Figure 3.4 shows all chosen configurations of η window pairs.

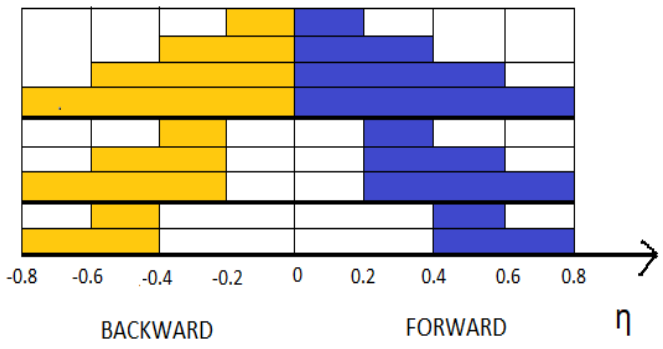

Fig 3.4: Illustration of sets of η windows with different widths $\delta\eta$ and separation gaps η_{gap}.

We have performed the following analysis considering the above criteria:

- **Dependence of FB multiplicity correlation on:**
    - **Separation between the FB windows (η_{gap}):**

      The FB multiplicity correlation strength $b_{Corr}(mult)$ as a function of η_{gap} and for four different window widths havs been shown in Fig. 3.5 at three collision energies $\sqrt{s}$ = 0.9, 2.76 and 7 TeV for EPOS3 simulated both with and without hydro *pp* events (left panel). Right panel of the figure represents ALICE data [15]. It has been observed that b_{corr} values for each center-of-mass energy decrease slowly with the increase of the separation between FB windows. It is clear that

the experimental values are higher than those of simulated values but the trend of dependence on η_{gap} is in agreement with the experiment.

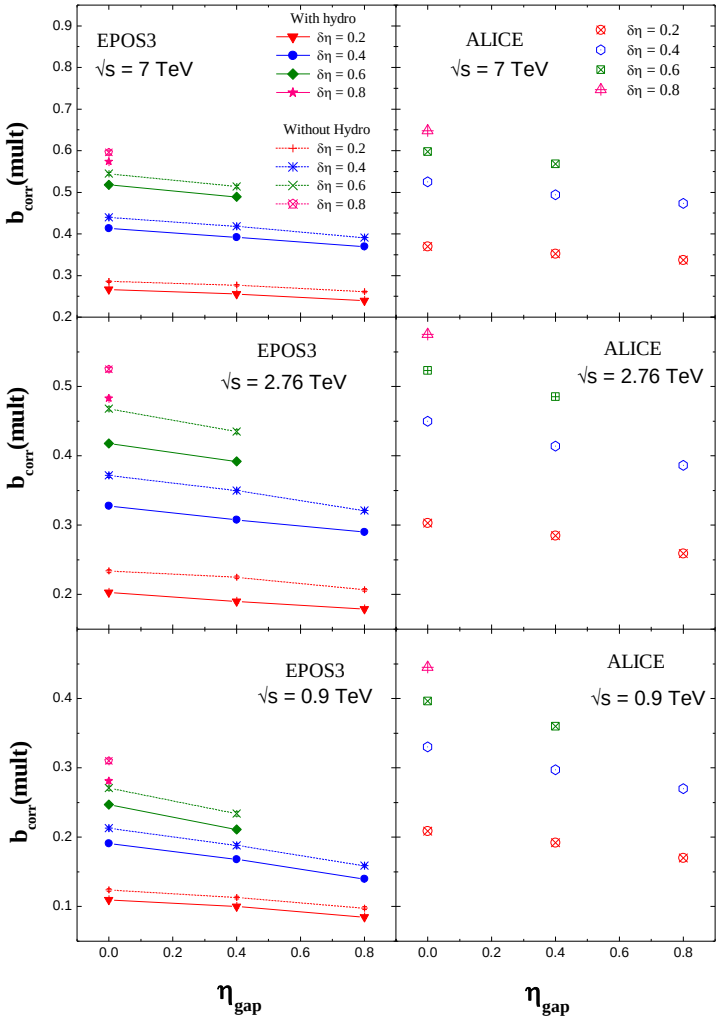

Fig. 3.5: FB multiplicity correlation $b_{corr}(mult)$ as a function of η_{gap} for four window widths $\delta\eta$ = 0.2, 0.4, 0.6 and 0.8 in pp events at three center-of-mass energies $\sqrt{s}$ = 0.9, 2.76 and 7 TeV. The left panel shows results from EPOS3 generated pp events with and without hydro, while the right panel presents corresponding measurements from ALICE experimental data [15].

- **Collision energy ($\sqrt{s}$):**

It is evident from Fig. 3.5 that with the increase of collision energy FB multiplicity correlation increases. To have a closer look on energy dependence, the FB multiplicity correlation strength $b_{Corr}(mult)$ is plotted with η_{gap} for

$\delta\eta$ = 0.4 at three center-of-mass energies in Fig. 3.6. Although the slopes of the η_{gap} dependence of $b_{Corr}(mult)$ for three center-of-mass energies remain approximately constant for experimental data [15] as well as simulated events, it has been observed that the pedestal values of $b_{Corr}(mult)$ increase with collision energy. One of the reasons of this increase of the pedestal values of $b_{Corr}(mult)$ with center-of-mass energy is the increase in mean multiplicity, $\langle N_f \rangle$. However, ALICE Collaboration [15] has reported that if one chooses window sizes such that the mean multiplicities stay constant at different energies, the increase is still noticeable. A strong energy dependence of $b_{Corr}(mult)$ values was also reported by the UA5 Collaboration [6] and ATLAS Collaboration [7].

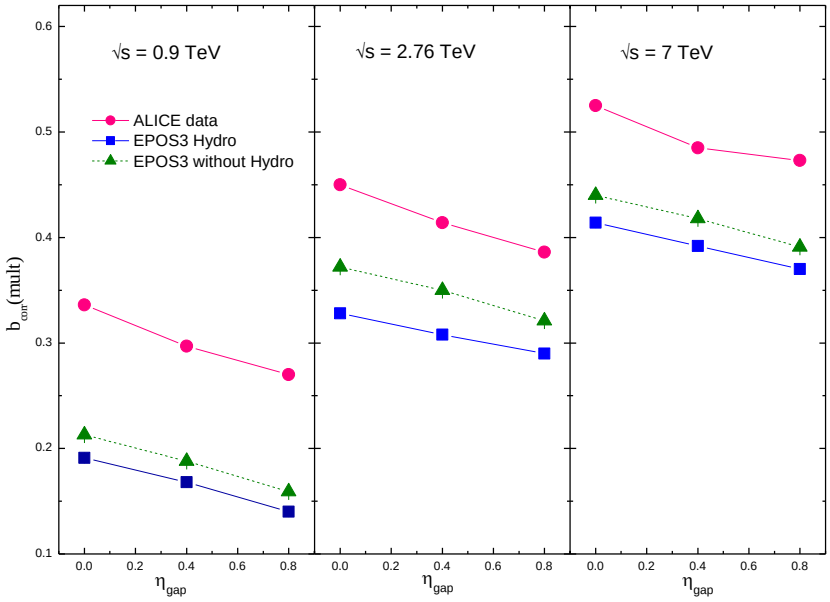

Fig. 3.6: FB multiplicity correlation $b_{corr}(mult)$ as a function of η_{gap} for window width $\delta\eta$ = 0.4 in pp events at $\sqrt{s}$ = 0.9, 2.76 and 7 TeV.

- **Dependence of FB summed-p_T correlations on η_{gap} and collision energy:**

The dependence of FB summed-p_T correlation on η_{gap} for four η intervals, i.e., $\delta\eta$ = 0.2, 0.4, 0.6 and 0.8 has been shown in Fig. 3.7 for three center-of-mass energies $\sqrt{s}$ = 0.9, 2.76 and 7 TeV for EPOS3 simulated both with and without hydro pp events following ALICE kinematics. It can be seen that, similar to FB multiplicity correlation, FB momentum correlation strength also decreases gradually with the increasing η_{gap}

for all window widths and maintains nearly constant slope. It increases with the increase of center-of-mass energy.

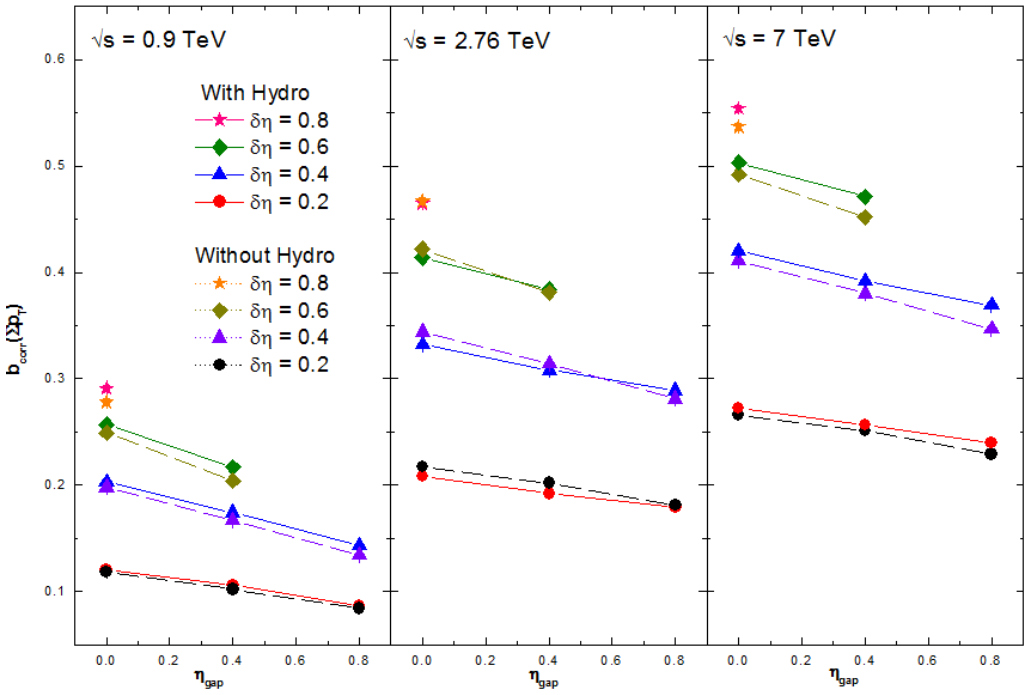

Fig. 3.7: FB summed-p_T correlation b_{corr} $(\sum p_T)$ as a function of η_{gap} for four windows widths $\delta\eta$ = 0.2, 0.4, 0.6 and 0.8 in pp events at $\sqrt{s}$ = 0.9, 2.76 and 7 TeV.

- ***δη*-dependence of FB multiplicity and momentum correlations:**

It can be noticed from Fig. 3.5 and Fig. 3.7 that for a fixed gap between FB windows, b_{corr} increases with the increase of window width. For studying the nature of increase, $b_{corr}(mult)$ and b_{corr} $(\sum p_T)$ are plotted for the most central window with respect to $\delta\eta$ for three center-of-mass energies in Fig. 3.8 and Fig. 3.9 respectively. The figures show that multiplicity and momentum correlations increase nonlinearly with window width $\delta\eta$. This dependence is in qualitative agreement with ALICE data [15]. The nonlinear dependence of b_{corr} on $\delta\eta$ has been explained in a simple model reported by ALICE Collaboration [15], along with other approaches mentioned in [2, 20, 34, 35]. The similar trend for both with and without hydro shows that the hydrodynamical evolution of the bulk matter has negligible effect on b_{corr} as the SRC may be dominated due to event-by-event multiplicity fluctuations.

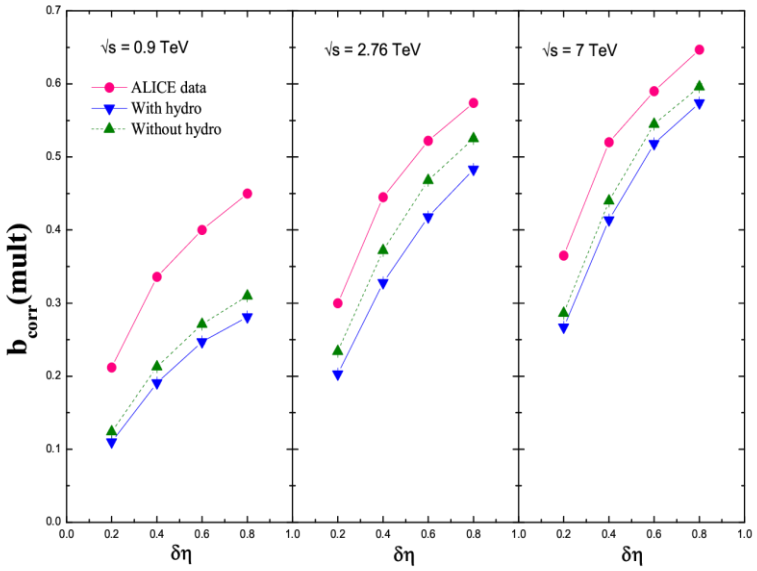

Fig. 3.8: Dependence of $b_{corr}(mult)$ on $\delta\eta$ with η_{gap}= 0 in pp events at $\sqrt{s}$ = 0.9, 2.76 and 7 TeV.

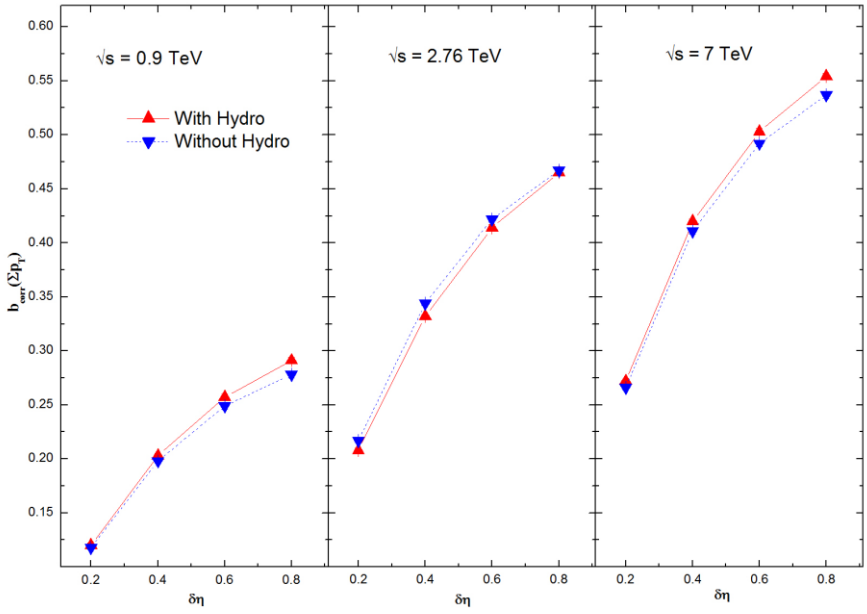

Fig. 3.9: Dependence of $b_{corr}(\sum p_T)$ on $\delta\eta$ with η_{gap}= 0 in pp events at $\sqrt{s}$ = 0.9, 2.76 and 7 TeV.

3.4.2 Analysis considering ATLAS kinematics:

In ATLAS [7] kinematics events are chosen with a minimum of two charged particles in the kinematic interval p_T > 0.1 (GeV/c) and |η| < 2.5. Equal intervals in pseudorapidity

of size $\delta\eta$ = 0.5 were chosen. All configurations of chosen window pairs for the analysis are drawn in Fig. 3.10.

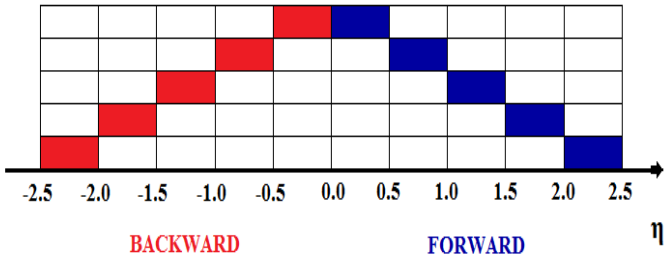

Fig. 3.10: Illustration of sets of η windows with equal window widths $\delta\eta$ = 0.5 and separation gaps η_{gap}.

The FB multiplicity correlation strengths have been calculated for the full matrix of FB windows of width $\delta\eta$ = 0.5 covering the whole range $|\eta|$< 2.5 and p_T > 0.1 GeV/c using EPOS3 simulated pp events with and without hydro at $\sqrt{s} = 0.9$ and 7 TeV. The results are shown in Fig. 3.11. The main diagonal represents the symmetric FB windows with increasing separation. It is evident that the FB multiplicity correlation varies strongly with η_{gap}s but weakly with the mean-η value for a given separation for both with and without hydro in EPOS3 simulated pp events at at $\sqrt{s} = 0.9$ and 7 TeV.

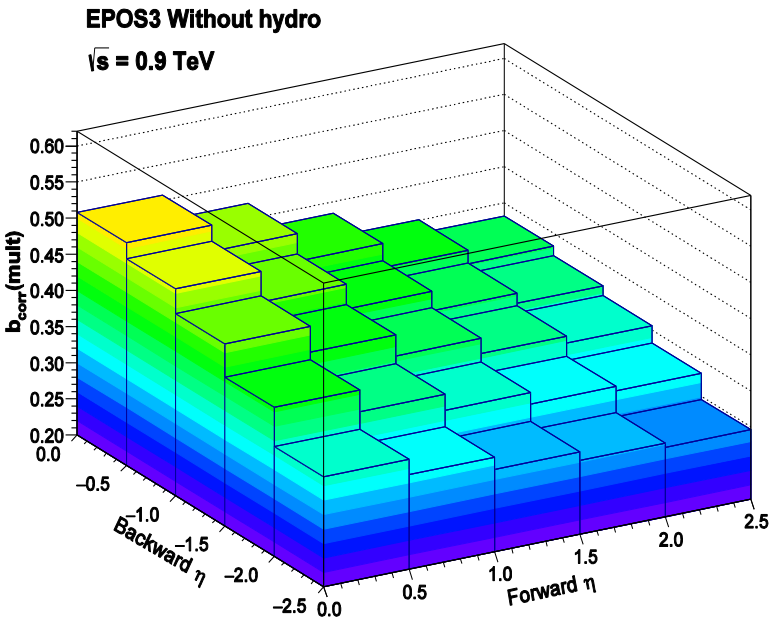

(a)

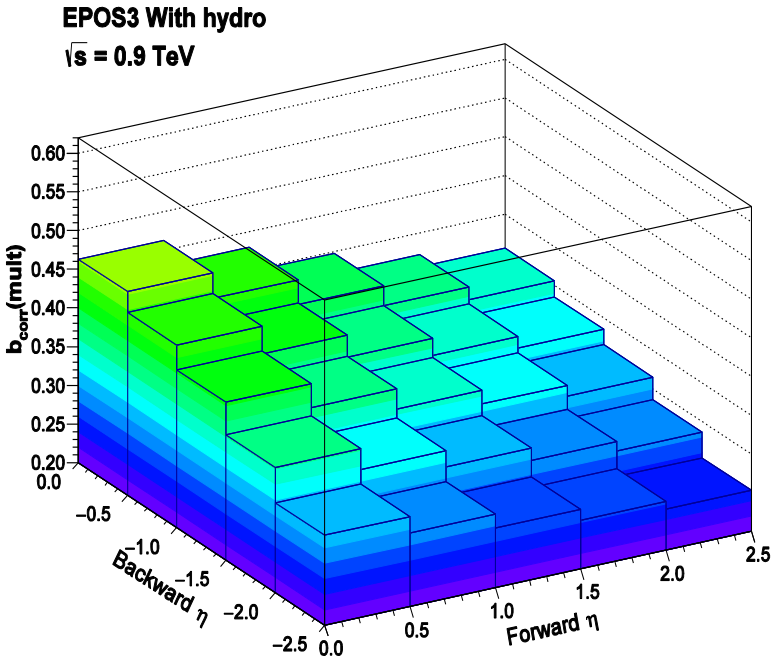
EPOS3 With hydro
√s = 0.9 TeV
b_corr(mult)
0.60
0.55
0.50
0.45
0.40
0.35
0.30
0.25
0.20
0.0
−0.5
−1.0
−1.5
−2.0
−2.5
Backward η
0.0
0.5
1.0
1.5
2.0
2.5
Forward η

(b)

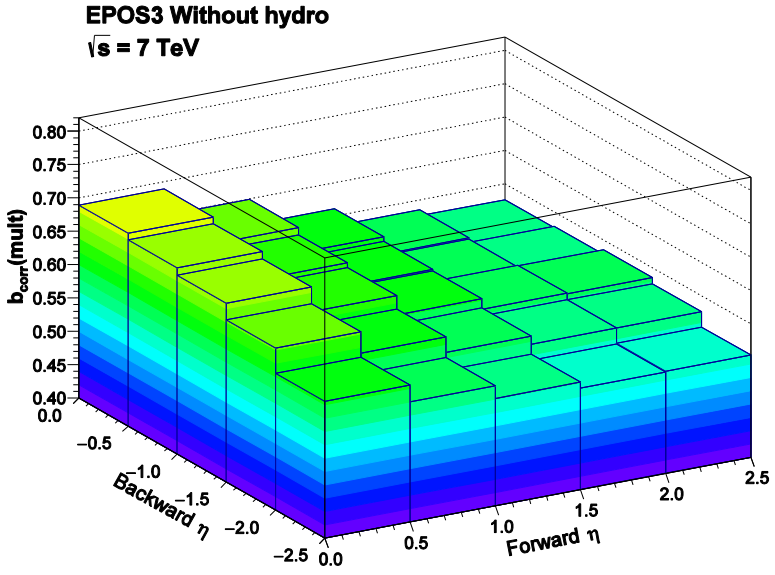
EPOS3 Without hydro
√s = 7 TeV
b_corr(mult)
0.80
0.75
0.70
0.65
0.60
0.55
0.50
0.45
0.40
0.0
−0.5
−1.0
−1.5
−2.0
−2.5
Backward η
0.0
0.5
1.0
1.5
2.0
2.5
Forward η

(c)

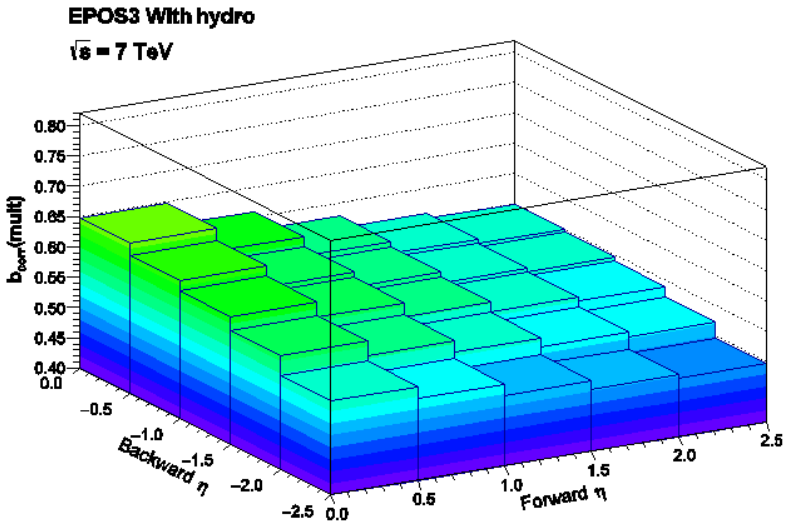

(d)

Fig. 3.11: Multiplicity correlation in a matrix of forward/backward η-intervals for $|\eta| < 2.5$ and p_T > 0.1 GeV/c for EPOS3 simulated events with at least two charged particles: (a) Without hydro at 0.9 TeV, (b) With hydro at 0.9 TeV, (c) Without hydro at 7 TeV, (d) With hydro at 7 TeV.

- **Dependence of FB multiplicity and momentum correlations on:**
  - **Separation between the FB windows (η_{gap}):**

The correlations between symmetrically opposite FB η-intervals of equal width $\delta\eta$ = 0.5 have also been observed separately. Fig. 3.12 and Fig. 3.13 respectively represent the dependence of FB multiplicity and momentum correlations on η_{gap} for EPOS3 simulated pp events at $\sqrt{s}$ = 0.9 and 7 TeV and compared to ATLAS results [7]. The lower panels of each figure represent the ratio between the simulated and experimental values for both the energies. It is interesting to note that the general trend is well reproduced by both types of EPOS3 simulated events. EPOS3 simulated events with hydro quantitatively reproduce the experimental data for different η_{gap}s except the most central one at $\sqrt{s}$ = 7 TeV but underestimate the correlation strength at $\sqrt{s}$ = 0.9 TeV, whereas, events without hydro overestimate the same for both the energies.

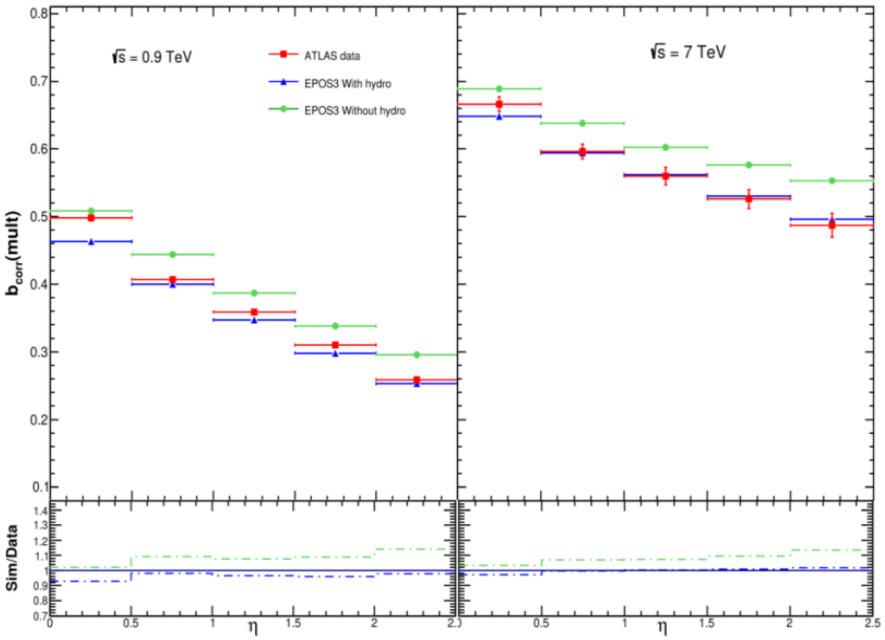

Fig. 3.12: FB multiplicity correlation in symmetrically opposite η intervals for EPOS3 simulated *pp* events with and without hydrodynamics, compared to ATLAS data at $\sqrt{s}$ = 0.9 and 7 TeV. (Lower panel) Ratio of simulated events to ATLAS data.

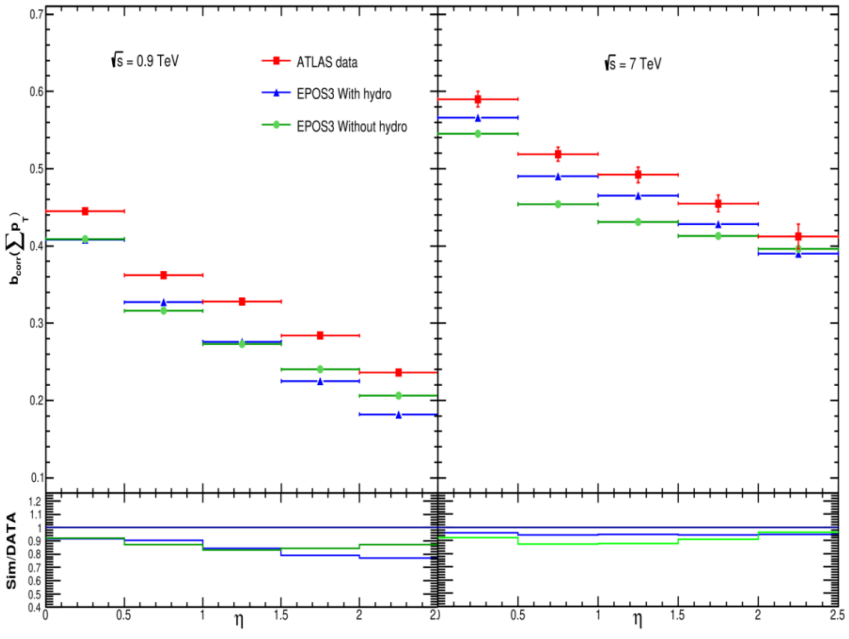

Fig. 3.13: FB momentum correlation in symmetrically opposite η intervals for EPOS3 simulated *pp* events with and without hydrodynamics, compared to ATLAS data at $\sqrt{s}$ = 0.9 and 7 TeV. (Lower panel) Ratio of simulated events to ATLAS data.

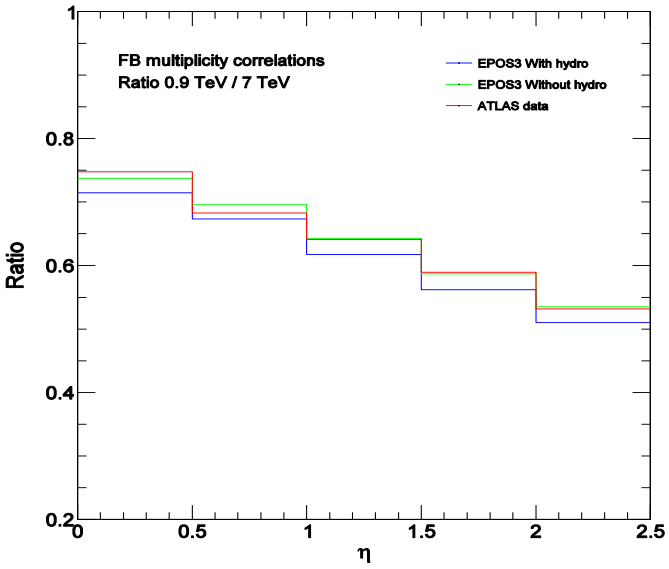

Fig. 3.14: Ratio of the FB multiplicity correlation for 0.9 TeV results to the 7 TeV results for EPOS3 generated with and without hydro pp events and ATLAS data.

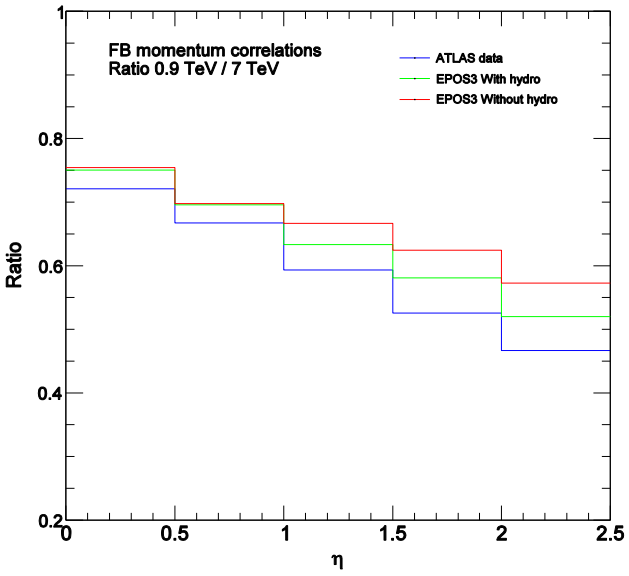

Fig. 3.15: Ratio of FB summed-p_T correlation for 0.9 TeV results to the 7 TeV results for EPOS3 generated with and without hydro pp events and ATLAS data.

- **Collision energy ($\sqrt{s}$):**

Figure 3.14 and Fig. 3.15 represent respectively the ratio of the above FB multiplicity and momentum correlation at $\sqrt{s}$ = 0.9 and 7 TeV for the simulated events as well as for the experimental data [7]. It has been found that both FB

multiplicity and momentum correlation is higher for 7 TeV than 0.9 TeV and the relative difference is greater for the higher pseudorapidity gaps. Here, we can infer that similar to the data, in EPOS3 simulated events the LRC dominates over the SRC as the collision energy increases.

- **Minimum transverse momentum (p_{Tmin}):**

We know that in high energy collisions with the increase of particle transverse momentum, there is a gradual transition from soft processes to hard processes. To capture the contribution of this transition in multiplicity correlation, we have evaluated the value of $b_{corr}(mult)$ for seven different values of minimum transverse momentum (p_{Tmin}), i.e., p_{Tmin}= 0.1, 0.2, 0.3, 0.5, 1.0, 1.5 and 2.0 GeV in case of symmetric FB windows with no separation for EPOS3 simulated events with and without hydro for pp collisions at $\sqrt{s}$ = 7 TeV and plotted in Fig. 3.16 along with the ATLAS data [7]. Figure 3.17 represents the variation of $b_{corr}(\sum p_T)$ with p_{Tmin} for the same EPOS3 simulated pp events. It has been found that the correlation decreases rapidly as p_{Tmin} increases above a few hundred MeV following the same trend as in the experimental data. The decrease is sharper for without hydro EPOS3 events than with hydro. However, the agreement with experimental result is better for with hydro EPOS3 events.

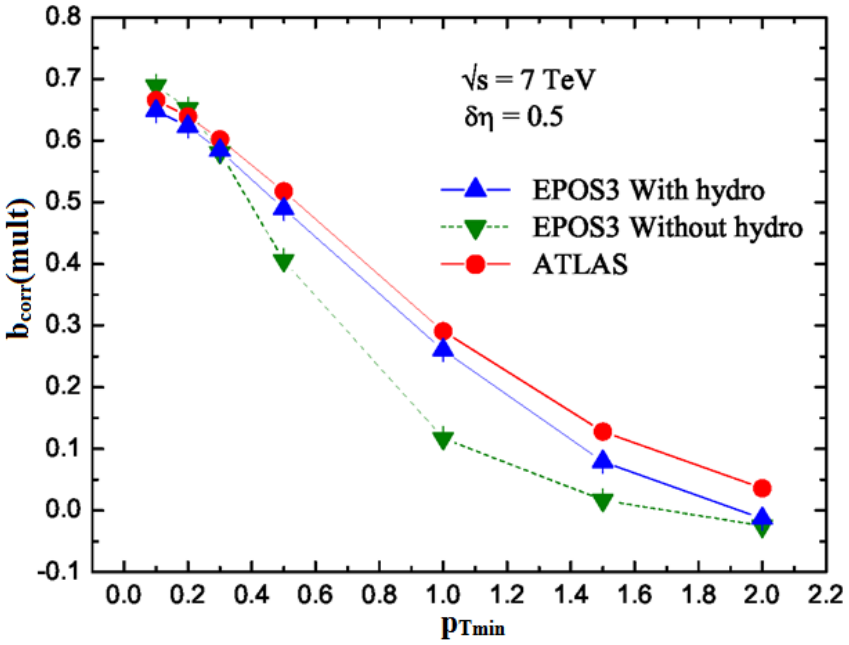

Fig. 3.16: FB multiplicity correlation as a function of p_{Tmin} for $\delta\eta$ = 0.5.

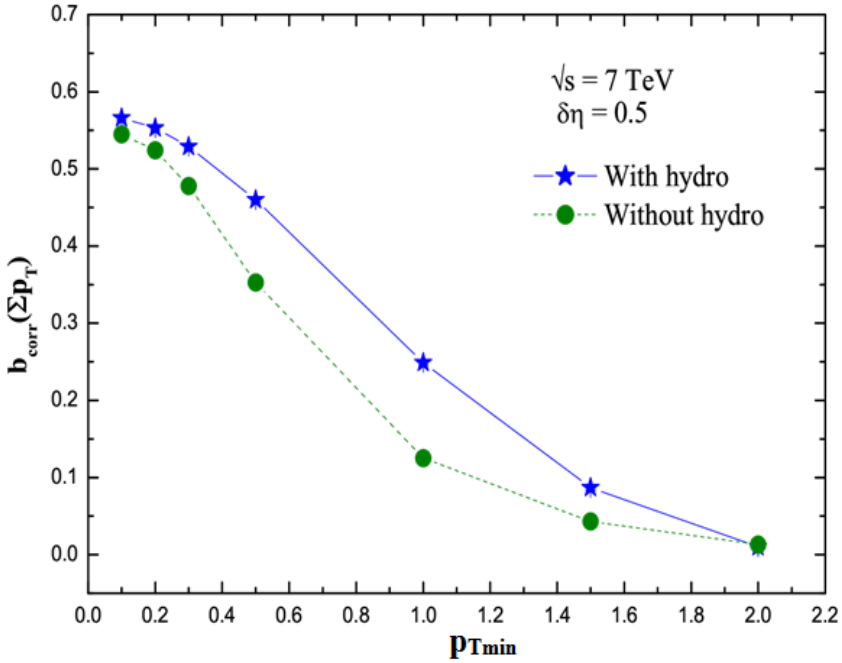

Fig. 3.17: FB momentum correlation as a function of p_{Tmin} for $\delta\eta$ = 0.5.

3.5 FB Multiplicity and Momentum Correlations in EPOS3 Generated *pp* Events at $\sqrt{s} = 13$ *TeV* and *pPb* Events at $\sqrt{s_{NN}} = 5.02$ *TeV*

Studies using different models show that the FB correlation strength is found to be increasing with decreasing nuclear size upon the selected η-windows and with increasing collision energy for a fixed collision system [36-37]. It has also been proposed that instead of the contribution coming from particle production in the initial stages of collisions, the subsequent stage could modify the behavior of FB correlations and hadron nucleus collision is expected to give more information on the whole scenario. Keeping this in mind, a comparative analysis of *pp* and *pPb* systems has been performed to enhance our current understanding of FB phenomena. We have extended our study on forward-backward correlation strength in terms of charged particle multiplicity and summed transverse momentum for *pp* collisions at the higher center-of-mass energy $\sqrt{s}$ = 13 TeV, as well as for *pPb* collisions at centre-of-mass energy $\sqrt{S_{NN}}$ = 5.02 TeV. As EPOS3 simulated with hydro *pp* events at lower vcenter-of-mass energies showed better agreement with ATLAS data, we have considered only EPOS3 simulated with hydro events for both *pp* and *pPb* collision systems in the present extrapolated study. In order to clarify the functions of each component of the model that contribute

to the outcomes, we have further divided the model into core and corona approaches. The energy density of the strings in the core is sufficient to activate the hydrodynamically evolving QGP description. In the corona, hadron creation from nucleon-nucleon collisions is viewed as an independent phenomenon [30].

We have measured FB multiplicity and momentum correlations for the EPOS3 generated events with all charged particles and particles originating from core and corona separately. Then we have thoroughly inspected the behaviour of both correlation strengths as a function of η_{gap}, $\delta\eta$, p_{Tmin} and different multiplicity classes following standard kinematical cuts used by the ALICE [15] and the ATLAS [7] experiments at the LHC energies for both EPOS3 generated event samples discussed above.

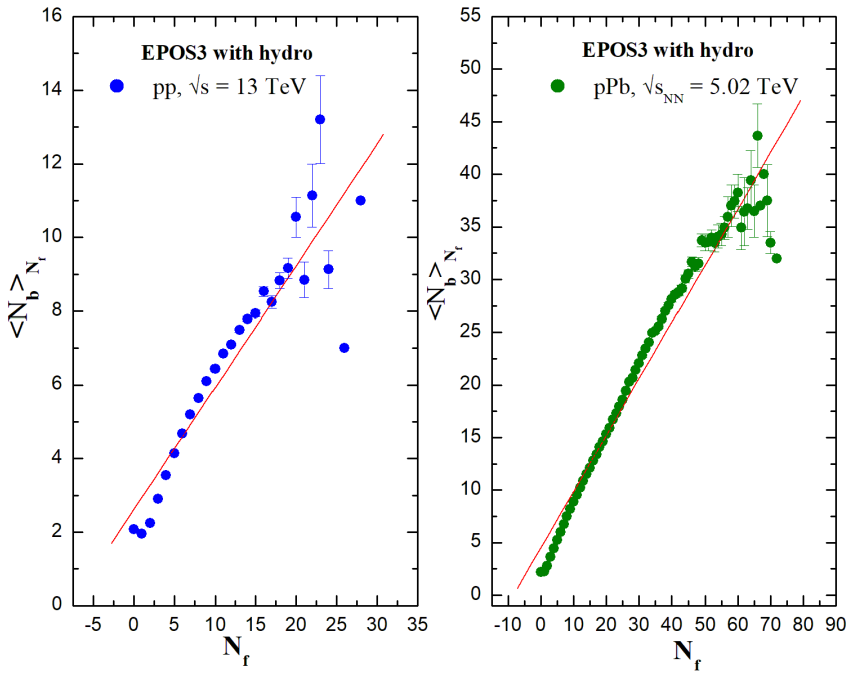

Fig. 3.18: Variation of $< N_b >_{N_f}$ with N_f for window width $\delta\eta$ = 0.6 and η_{gap} = 0.4 for EPOS3 generated pp events at $\sqrt{s}$ = 13 TeV (left panel) and pPb events at $\sqrt{S_{NN}}$ = 5.02 TeV (right panel). Red lines represent linear fits for both systems.

We have calculated and plotted in Fig. 3.18 the average backward multiplicity ($< N_b >_{N_f}$) for each fixed value of forward multiplicity N_f for window width $\delta\eta$ = 0.6 and η_{gap} = 0.4 for EPOS3 generated pp events at $\sqrt{s}$ = 13 TeV (left panel) and pPb

events at $\sqrt{S_{NN}}$ = 5.02 TeV (right panel). It is noticeable that the scatter plots confirm a linear relationship between $< N_b >_{N_f}$ and N_f. A linear fit has been displayed by the red lines in both panels. Therefore, we have used the Pearson correlation coefficient formulas described in Eq. (3.2) and Eq. (3.3) to evaluate FB multiplicity and momentum correlation strengths respectively.

- **Dependence of FB multiplicity and momentum correlations on:**

  - **Separation between the FB windows (η_{gap}):**

    The variation of FB multiplicity and momentum correlation strengths with η_{gap} for four different window widths ($\delta\eta$ = 0.2, 0.4, 0.6 and 0.8) have been shown in Fig. 3.19 and Fig. 3.20 respectively for EPOS3 simulated all charged particles, only-core and only-corona particles in pp collisions at $\sqrt{s}$ = 13 TeV (top panel) and pPb collisions at $\sqrt{S_{NN}}$ = 5.02 TeV (bottom panel). We have compared all three cases for window widths $\delta\eta$ = 0.2 and 0.4 (left panel) and $\delta\eta$ = 0.6 and 0.8 (right panel) for both pp and pPb events. We observed that for a fixed window width, the FB correlation strengths decrease slowly with the increasing η_{gap} and increase with increasing $\delta\eta$ at a fixed η_{gap}, which resemble the trend at lower centre-of-mass energies in pp collisions as described in our earlier study.

    Quantitatively, we found that the correlation strengths are larger for pPb collisions than for pp collisions for all chosen η_{gap} and $\delta\eta$ combinations. The asymmetric nature of pPb collisions where the proton collides with a nucleus containig a larger number of sources compared to pp collisions, results in a higher initial-state parton density in the lead nucleus than in the proton. Such asymmetric collisions could have larger fluctuations in the final state which may contribute to stronger FB correlation strength in pPb collisions with respect to pp collisions.

    Interestingly, we have noticed that for pPb events the correlation strengths decrease faster with increasing η_{gap} as compared to pp events. The SRC component depends strongly on the collision system, and it is asymmetric

between the forward and backward windows in pPb collisions, while the LRC component is nearly symmetric in all collision systems [1]. Thus, the faster dilution of the SRC component at large η_{gap} between the forward and backward regions could be the reason behind the faster decrease of correlation strength in asymmetric pPb collisions with respect to symmetric pp collisions.

The dominance of correlation strength due to core-only particles is clearly visible over corona-only particles. Since the particles from the corona are mostly dominated by jets or minijet partons, the paucity of the LRC component results in smaller correlation strength for particles from the corona over the core at large η_{gap} for both collision systems.

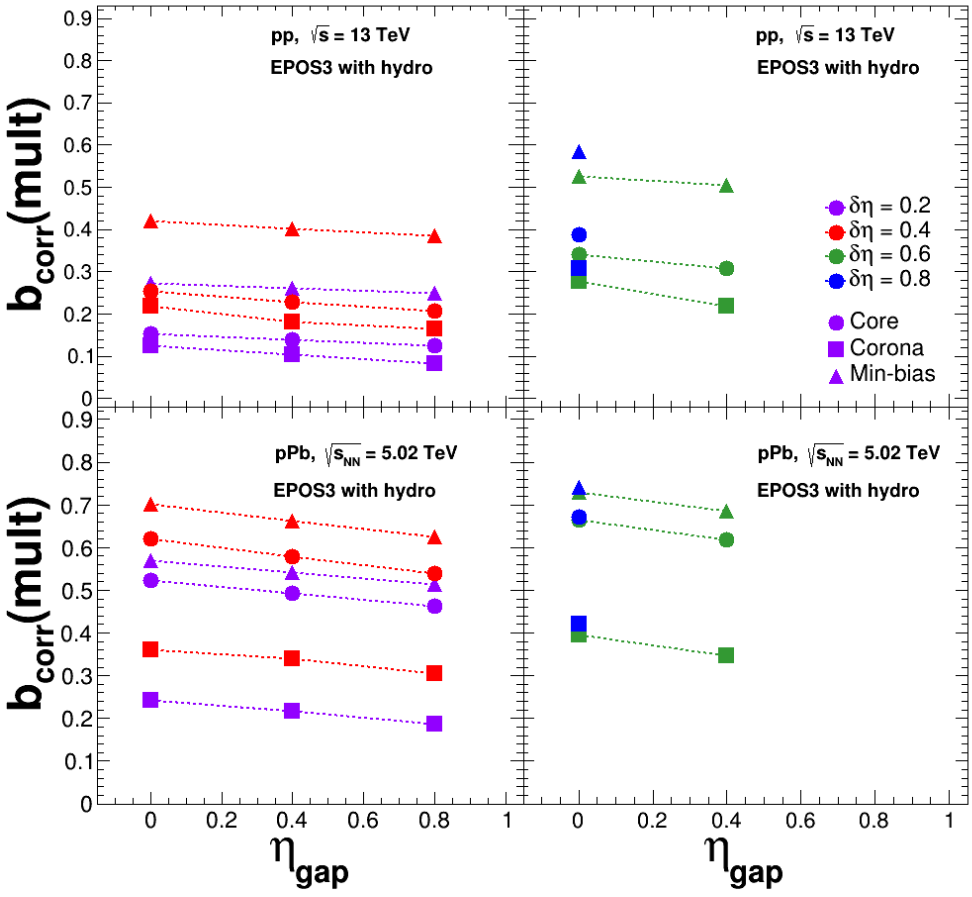

Fig. 3.19: $b_{corr}(mult)$ as a function of η_{gap} for $\delta\eta$ = 0.2, 0.4, 0.6 and 0.8 for EPOS3 generated all charged particles and particles from core and corona in pp ($\sqrt{s}$ = 13 TeV) collisions (top panel) and pPb ($\sqrt{S_{NN}}$ = 5.02 TeV) collisions (bottom panel).

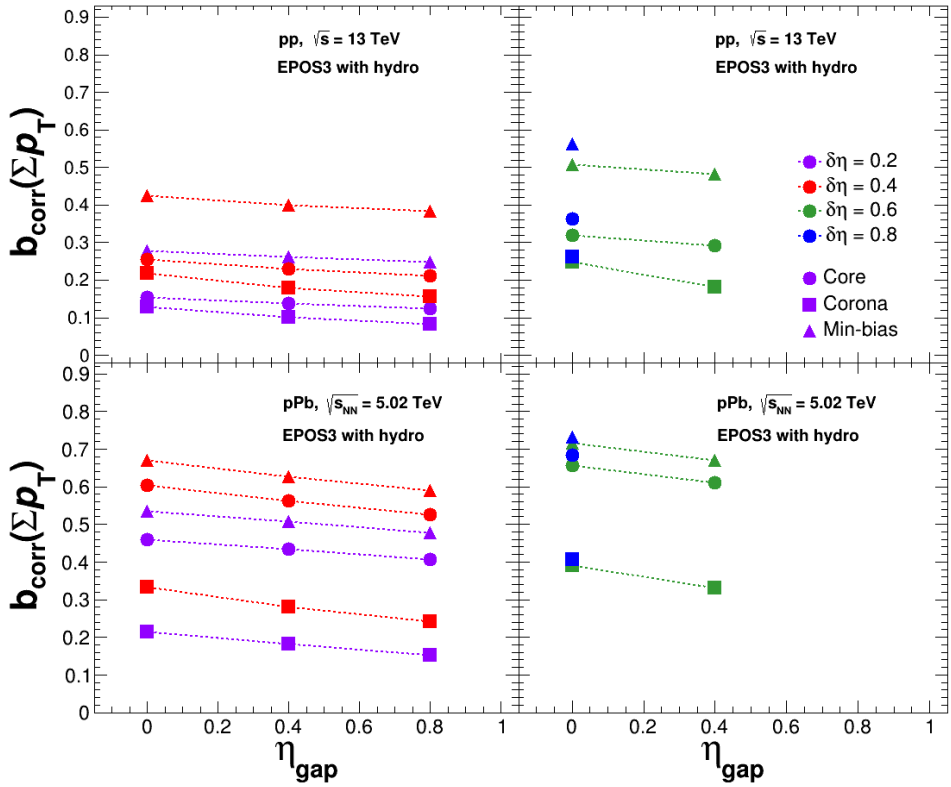

Fig. 3.20: $b_{corr}(\Sigma p_T)$ as a function of η_{gap} for $\delta\eta$ = 0.2, 0.4, 0.6 and 0.8 for EPOS3 generated all charged particles and particles from core and corona in pp ($\sqrt{s}$ = 13 TeV) (top panel) and pPb ($\sqrt{S_{NN}}$ = 5.02 TeV) collisions (bottom panel).

- **FB window width ($\delta\eta$):**

The $\delta\eta$-dependence of FB multiplicity and momentum correlation strengths for contiguous (η_{gap} = 0), symmetrical windows with respect to collision centre are shown in Fig. 3.21 and Fig. 3.22 respectively for pp collisions at $\sqrt{s}$ = 13 TeV and pPb collisions at $\sqrt{S_{NN}}$ = 5.02 TeV using EPOS3 simulated with hydro events. We have studied and presented the multiplicity and momentum correlation strengths for the EPOS3 generated event samples with all charged particles and particles from core and corona. We observed that the core-only and corona-only cases underestimate both the correlation strengths for minimum-bias event sample. The correlation strengths increase nonlinearly with $\delta\eta$ for both pp and pPb events though the values are higher in case of pPb events which may be due to reason described earlier. The results are found to be similar to our earlier measurements qualitatively, featuring the dominance of SRC component for the nonlinear growth of the FB correlation strengths. Here also we have found that

the correlation strengths as a function of $\delta\eta$ are larger for core-only particles than corona-only particles.

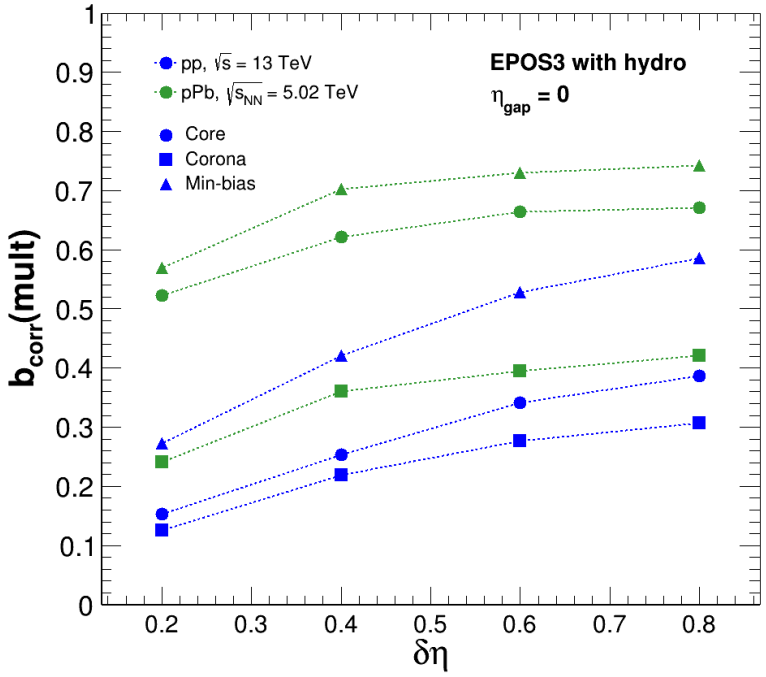

Fig. 3.21: $b_{corr}(mult)$ as a function of $\delta\eta$ for EPOS3 generated pp and pPb events for all charged particles and particles from core and corona.

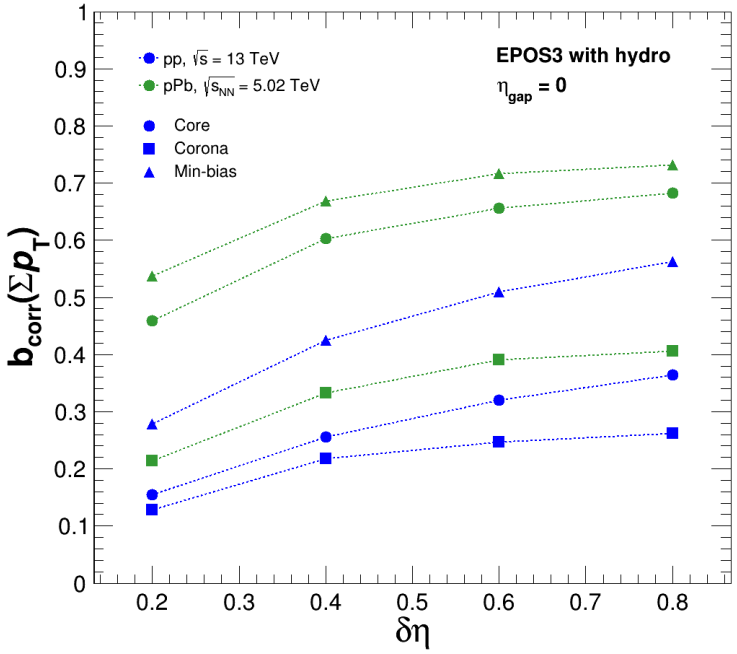

Fig. 3.22: $b_{corr}(\sum p_T)$ as a function of $\delta\eta$ for EPOS3 generated pp and pPb events for all charged particles and particles from core and corona.

- **Mminimum transverse momentum (p_{Tmin}):**

The variation of FB multiplicity and momentum correlations with minimum transverse momentum of charged particles (p_{Tmin}) have been shown in Fig. 3.23 and Fig. 3.24 respectively for both EPOS3 generated with hydro pp events at $\sqrt{s}$ = 13 TeV and pPb events at $\sqrt{S_{NN}}$ = 5.02 TeV following ATLAS kinematics [7]. We calculated the values of b_{corr} at seven different levels of minimum transverse momentum (p_{Tmin}), specifically at p_{Tmin} = 0.1, 0.2, 0.3, 0.5, 1.0, 1.5, and 2.0 GeV/c. These calculations were performed for symmetric forward-backward windows without any separation. The multiplicity and momentum correlation strengths decrease rapidly with the increase of p_{Tmin} values for both pp and pPb events confirming similar trend at lower center-of-mass energies. With the increase of p_{Tmin}, dominance of LRC component decreases resulting weaker FB multiplicity and momentum correlation strengths suggesting the transition from soft process to hard processes with increasing transverse momentum of the produced particles. As described earlier, the correlation strengths are also found to be greater for pPb collisions than for pp collisions.

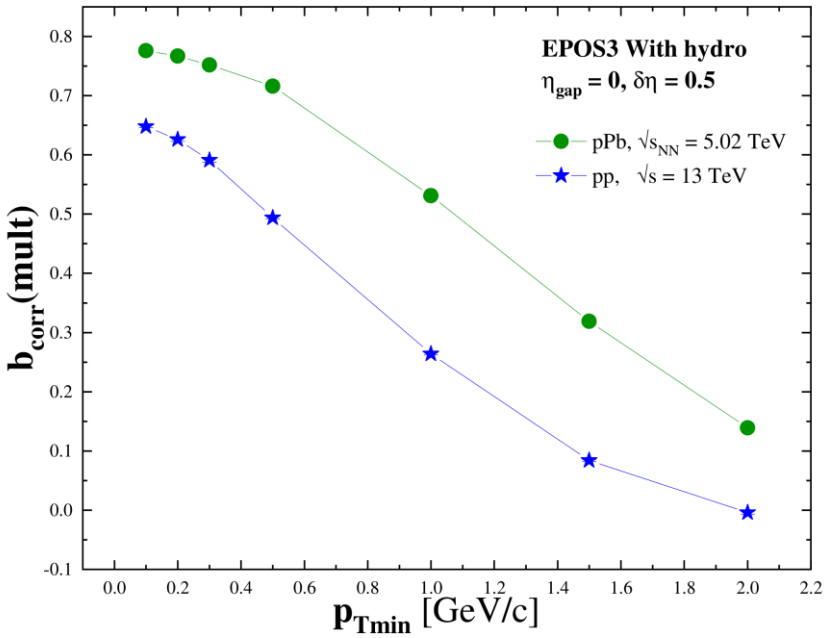

Fig. 3.23: $b_{corr}(mult)$ as a function of p_{Tmin} for window width $\delta\eta$ = 0.5 for EPOS3 simulated pp events at $\sqrt{s}$ = 13 TeV and pPb events at $\sqrt{S_{NN}}$ = 5.02 TeV.

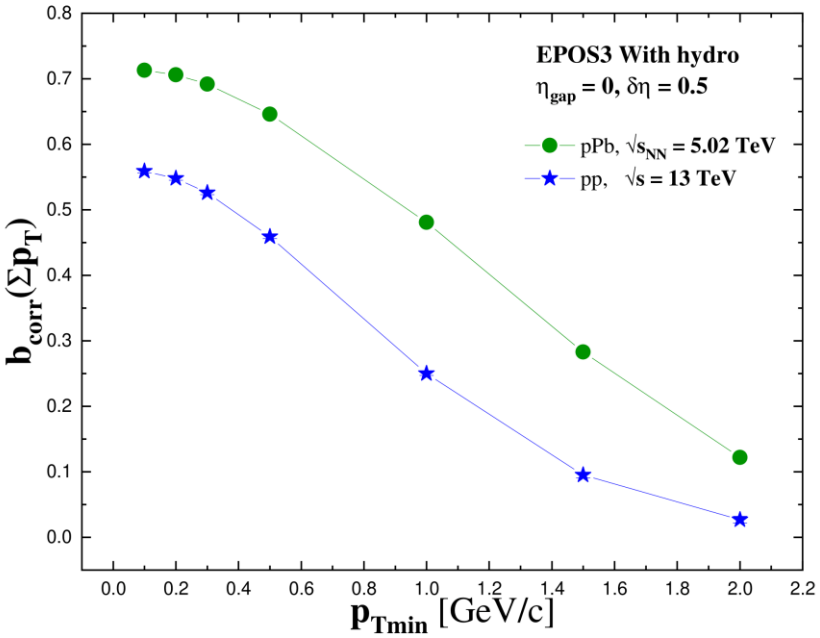

Fig. 3.24: $b_{corr}(\sum p_T)$ as a function of p_{Tmin} for window width $\delta\eta$ = 0.5 for EPOS3 simulated pp events at $\sqrt{s}$ = 13 TeV and pPb events at $\sqrt{S_{NN}}$ = 5.02 TeV.

3.6 $\delta\eta$-Weighted Average of FB Correlations in pp Collisions: Energy Dependence

An intuitive observable, the $\delta\eta$-weighted average of the FB multiplicity and momentum correlation strength, has been introduced for the first time and is defined as follows:

$$\langle b_{corr}\,(mult)/b_{corr}(\sum p_T)\rangle_{\delta\eta} = \frac{\sum_i((b_{corr}(mult)/b_{corr}(\sum p_T))_i \delta\eta_i}{\sum_i \delta\eta_i}. \qquad (3.4)$$

We have examined the behaviour of $\delta\eta$-weighted average of FB multiplicity and momentum correlation strengths as a function of centre-of-mass energy using EPOS3 simulated pp event samples. Such an unconventional measurement is still not available experimentally. Hence, to compare our findings in a systematic way we have evaluated $\delta\eta$-weighted average for the available experimental $b_{corr}(mult)$ and $b_{corr}(\sum p_T)$ values for the ALICE [15] and the ATLAS [7] data. Figure 3.25 and Fig. 3.26 show the $\delta\eta$-weighted average of FB multiplicity and momentum correlation as a function of centre-of-mass energy following ALICE and ATLAS kinematics.

In the left panel of Fig. 3.25 and Fig. 3.26, we observed that initially $< b_{corr}(mult) >_{\delta\eta}$ and $< b_{corr}(\sum p_T) >_{\delta\eta}$ values increase rapidly with increasing $\sqrt{s}$ upto 2.76 TeV, then grows moderately upto $\sqrt{s}$ = 7 TeV for both EPOS3 simulated events and experimental data. For comparison, we have calculated the $\delta\eta$-weighted average of FB correlation strengths using results from other available theoretical models including QGSM [20, 35] which also show a similar trend.

It is also very interesting to find that for EPOS3 simulated events, the $\delta\eta$-weighted average of FB correlation strengths as a function of $\sqrt{s}$ lean towards saturation approximately beyond $\sqrt{s}$ = 7 TeV, where there is no available experimental data for such a measurement. The derived results from QGSM model although do not show such a strong saturation effect at higher energy.

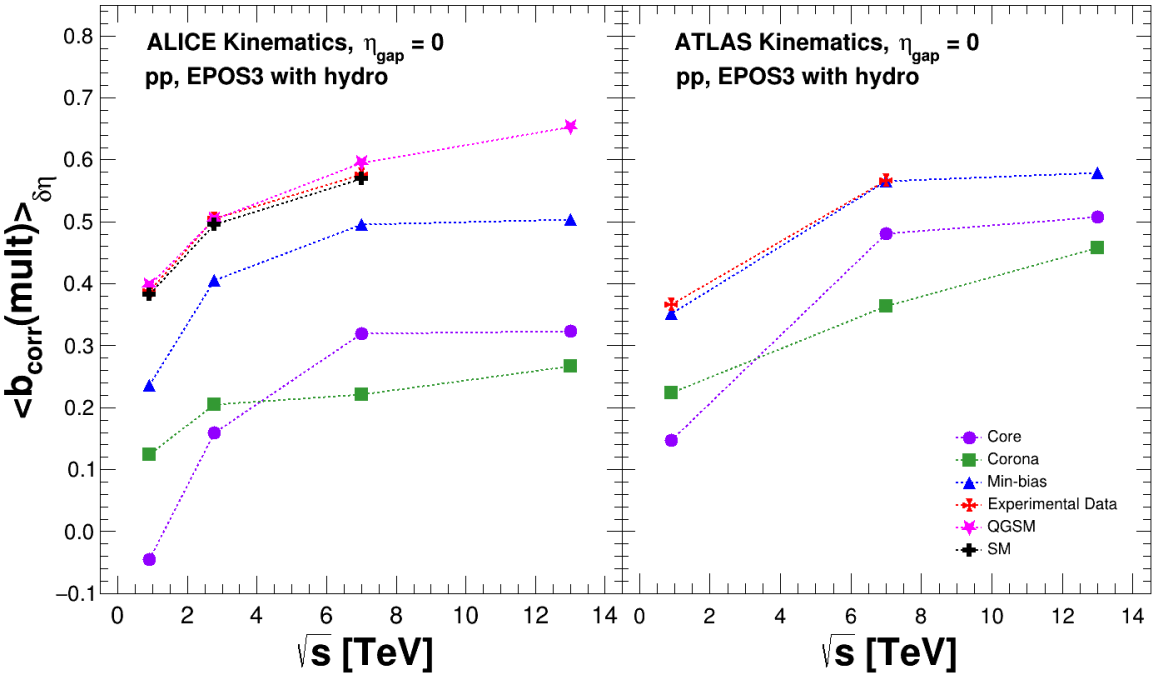

Fig. 3.25: Comparison of $\delta\eta$-weighted average FB multiplicity correlations ($< b_{corr}(mult) >_{\delta\eta}$) as a function of $\sqrt{s}$ for the EPOS3 simulated pp events (all charged particles, core and corona) following ALICE kinematics (left) and ATLAS kinematics (right). The results are compared with derived ALICE data (left), ATLAS data (right), and theoretical model-derived data (left).

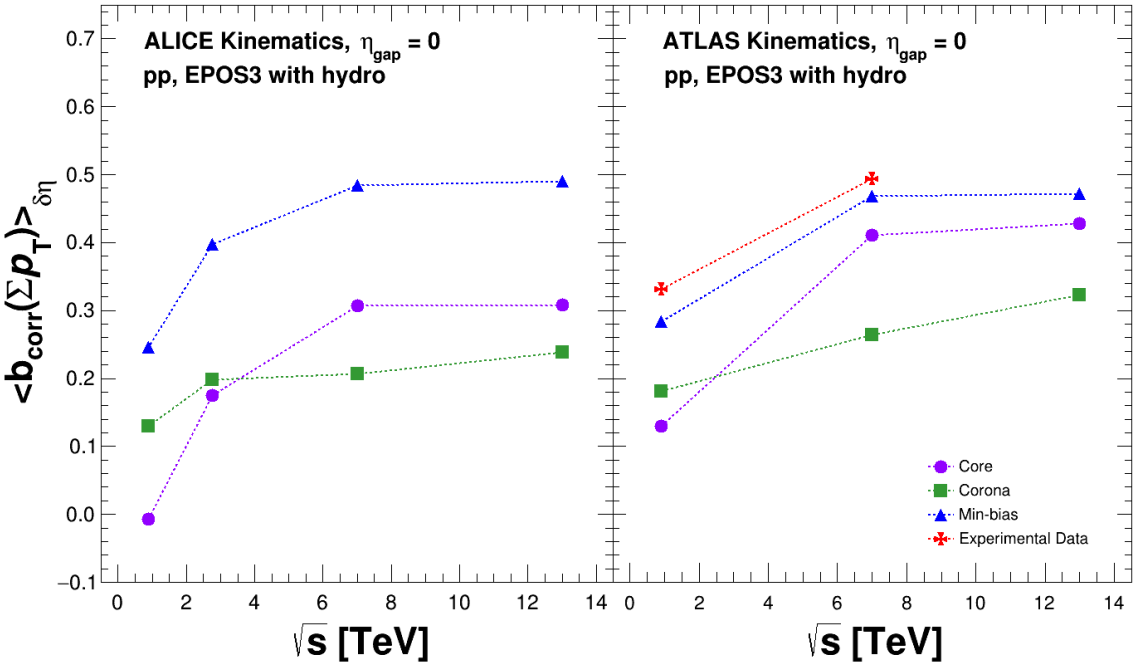

Fig. 3.26: Comparison of $\delta\eta$-weighted average FB summed-p_T correlations ($< b_{corr}(\sum p_T) >_{\delta\eta}$) as a function of $\sqrt{s}$ for the EPOS3 simulated pp events (all charged particles, core and corona) following ALICE kinematics (left) and following ATLAS kinematics (right) along with derived ATLAS data.

For better understanding of the fascinating behavior observed in the $\delta\eta$-weighted average of FB correlation strengths, we computed this metric separately for the particles coming either from core or corona. We have found that the observed saturation at higher centre-of-mass energy is predominantly due to the saturation for the core-only particles whereas the corona-only particles show increasing trend. In EPOS3 model, the corona is dominated by the high-p_T particles whereas the core contains particles which undergo 3+1D hydro mimicking the formation of QGP-like medium [38].

The exchange of multiple pomerons between colliding particles [39] in a collision remains the primary source of fluctuations producing multiple particles in a correlated way. The multiplicity of produced particles and their transverse momentum is thus very much influenced by the initial conditions of a collision, and in particular, they are much more apparent in small collision systems like pp or pA where final-state effects are less.

In the CGC framework [40, 41] it has been argued that at small $x \sim p_T/\sqrt{s}$, gluon density first grows and then gets saturated with an increase in energy which results in a moderate increase in charge particle multiplicity density in pp or pA collisions as the beam energy increases [42]. Since an observable like b_{corr} is an extensive quantity, it might show such a saturation effect mainly because fluctuations associated with the number of sources get saturated [39]. Henceforth, the EPOS3-model-based FB correlation analysis at higher center-of-mass energy encourages further experimental study.

3.7 Multiplicity Dependence of FB Momentum Correlation

In addition to the study using minimum-bias EPOS3 events, we have exploited a multiplicity-dependent summed-p_T FB correlations study as well. The charged-particle multiplicity (N_{ch}) have been calculated following ATLAS kinematics [7] for this study.

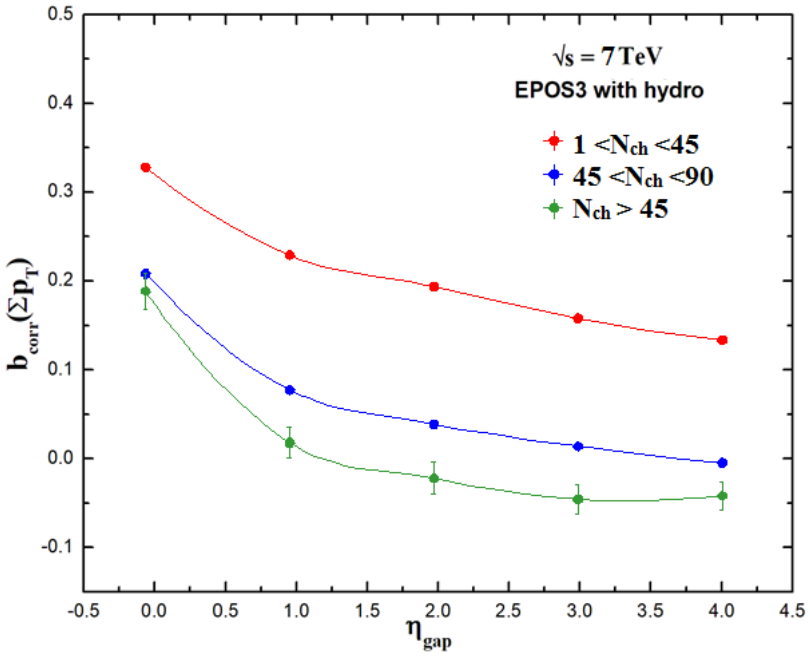

Fig. 3.27: FB summed-p_T correlations as a function of $\boldsymbol{\eta_{gap}}$ for window width $\delta\eta$ = 0.5 in different multiplicity range in EPOS3 simulated pp events at $\sqrt{s}$ = 7 TeV.

Figure 3.27 shows FB summed-p_T correlation as a function of η_{gap} for $\delta\eta$ = 0.5 in three nonoverlapping multiplicity regions for EPOS3 simulated pp events at $\sqrt{s}$ = 7 TeV: low ($1 < N_{ch} < 45$), mid ($45 < N_{ch} < 90$) and high ($N_{ch} > 90$). Red, blue and green points represent the low-, mid- and high-multiplicity region respectively.

Fig. 3.28 and Fig. 3.29 show similar FB summed-p_T correlation as a function of η_{gap} for $\delta\eta$ = 0.5 using EPOS3 simulated pp events at $\sqrt{s}$ = 13 TeV and pPb events at $\sqrt{S_{NN}}$ = 5.02 TeV respectively. For consistency and comparative understanding we have used the same multiplicity intervals in both systems: low ($2 < N_{ch} < 30$), mid ($30 < N_{ch} < 60$) and high ($60 < N_{ch} < 90$). Again, red, blue, and green points correspond to the low-, mid- and high-multiplicity classes respectively.

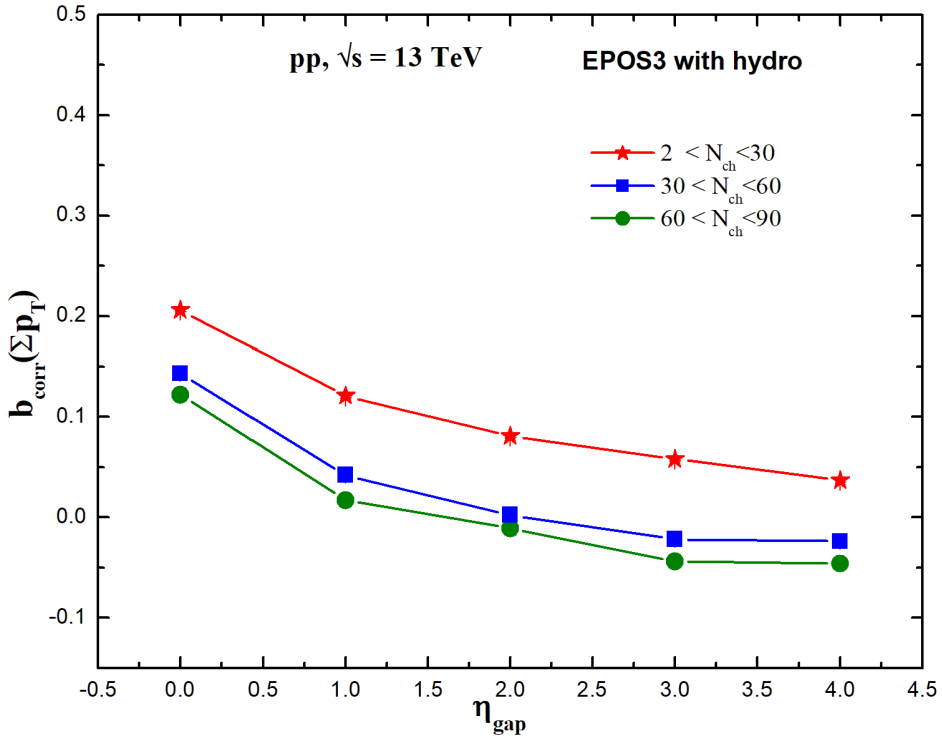

Fig. 3.28: FB summed-p_T correlations as a function of η_{gap} for window width $\delta\eta$ = 0.5 in different multiplicity ranges for EPOS3 simulated pp events at $\sqrt{s}$ = 13 TeV.

In all three figures, we observe that the correlation strength decreases with increasing η_{gap}. Interestingly, we found that $b_{corr}(\sum p_T)$ decreases with increasing multiplicity for a fixed η_{gap} and becomes lowest in high-multiplicity events. The decrease in correlation strength with increasing multiplicity could be due to the fact

that, in EPOS3, high-multiplicity events are generated via breaking of parent strings into a sequence of string segments producing a large string density, i.e., core. Such fusion of strings into core may lead to the smearing of correlation strength reflecting lower FB correlation in different η window in high-multiplicity EPOS3 events. The negative values for $b_{corr}(\sum p_T)$ (anticorrelation) in high-multiplicity EPOS3 events in larger η_{gap} could be due to lack of enough statistics.

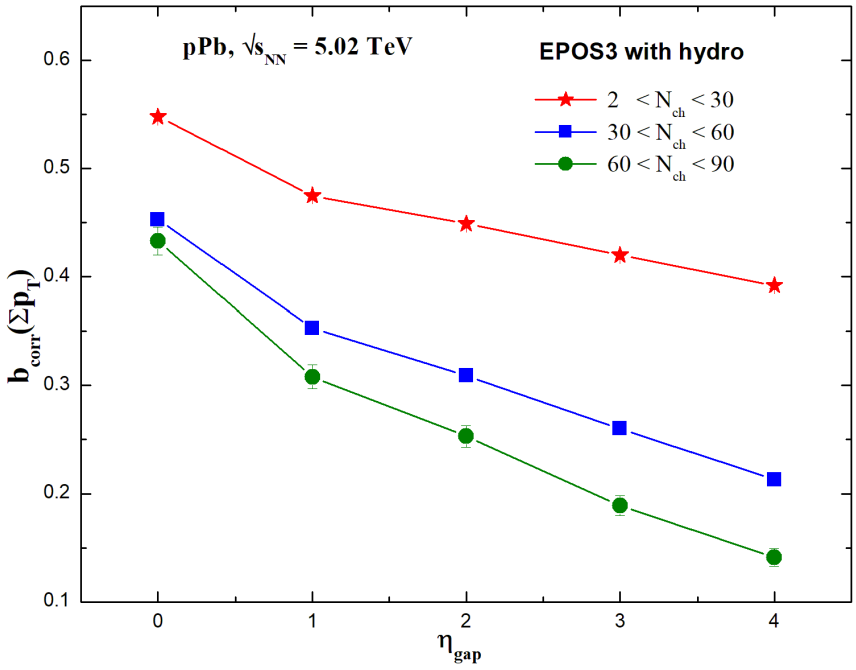

Fig. 3.29: FB summed-p_T correlations as a function of η_{gap} for window width $\delta\eta$ = 0.5 in different multiplicity ranges for EPOS3 simulated pPb events at $\sqrt{S_{NN}}$ = 5.02 TeV.

3.8 Study of Forward-Backward Correlations Using a Strongly Intensive Observable

Most challenging part of FB correlation study is to avoid volume fluctuations, i.e., event-by-event fluctuations of the number of the participating nucleons [43, 44]. Though considering intensive observable like the sum of the absolute transverse momentum of particles within the observation windows reduces such contribution of volume fluctuations [45, 46], our multiplicity-dependent summed-p_T correlation study displayed that FB momentum correlation strength depends on the total number of

charged particle produced in a pseudorapidity bin. Hence, we have explored more sophisticated correlation observable Σ [47] to suppress the contribution of volume fluctuations.

In the context of FB multiplicity fluctuation studies, the strongly intensive observable $\Sigma[N_f, N_b]$ is defined by the following formula:

$$\Sigma[N_f, N_b] = \frac{W_b\langle N_f\rangle + W_f\langle N_b\rangle - 2(\langle N_f N_b\rangle - \langle N_f\rangle\langle N_b\rangle)}{\langle N_f\rangle + \langle N_b\rangle}. \quad (3.5)$$

Here, forward (backward) scaled variance, $W_{f(b)}$, is defined as:

$$W_{f(b)} = \frac{\langle {N_{f(b)}}^2\rangle - \langle N_{f(b)}\rangle^2}{\langle N_{f(b)}\rangle}.$$

It has been confirmed [48] that the strongly intensive observable Σ does not depend on system volume nor system volume fluctuations and carries more clear information on the early dynamics of the high energy hadronic interactions compared to FB multiplicity and momentum correlations.

We have studied the behaviour of $\Sigma[N_f, N_b]$ as a function multiplicity bin width and η_{sep} (distance between F and B window centers) in EPOS3 simulated pp events at $\sqrt{s}$ = 13 TeV and pPb events at $\sqrt{s_{NN}}$ = 5.02 TeV with hydrodynamical evolution of particles.

- **Dependence of the strongly intensive observable $\Sigma[N_f, N_b]$ on:**
  - **Multiplicity bin width:**

    Figure 3.30 represents $\Sigma[N_f, N_b]$ variable as a function of the multiplicity bin width i.e. Δmultiplicity for both EPOS3 simulated with hydro pp events at $\sqrt{s}$ = 13 TeV and pPb events at $\sqrt{s_{NN}}$ = 5.02 TeV. Identifying sharp multiplicity cuts we have converted pp and pPb events multiplicity distributions into percentile classes following ALICE centrality class determination method. We focused mainly on the most central part, i.e., high-multiplicity events (0-10%). We increased multiplicity bin width from 2% to 10% around 5% of both pp and pPb event multiplicity classes.

It is clear from the figure that with the increase of multiplicity bin width, $\Sigma[N_f, N_b]$values remain almost unaffected for both pp and pPb events. Also we observed that the values of $\Sigma[N_f, N_b]$are higher for pp events than pPb events. More geometrical fluctuations in pp events compared to pPb events may result higher $\Sigma[N_f, N_b]$ values in pp events for each value of multiplicity bin widths.

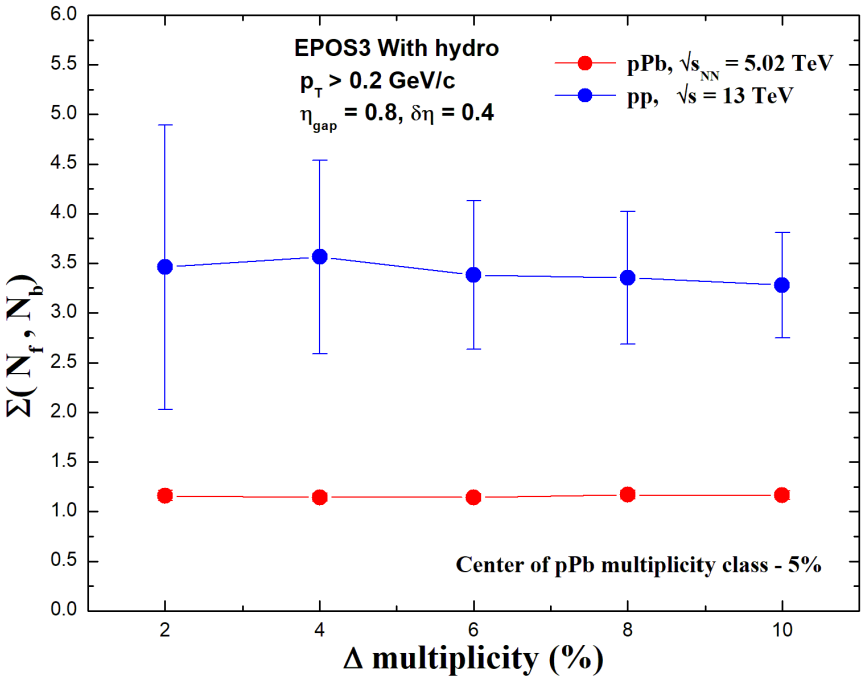

Fig. 3.30: $\Sigma[N_f, N_b]$ as a function of narrow multiplicity bin width for window width $\delta\eta$ = 0.4 in EPOS3 simulated pp events at $\sqrt{s}$ = 13 TeV and pPb events at $\sqrt{s_{NN}}$ = 5.02 TeV.

- **Separation between FB window centers (η_{sep}):**

Figure 3.31 exhibits the variation of $\Sigma[N_f, N_b]$ with η_{sep} for EPOS3 simulated with hydro pp events at $\sqrt{s}$ = 13 TeV and pPb events at $\sqrt{s_{NN}}$ = 5.02. It is clearly visible that $\Sigma[N_f, N_b]$ values increase with the increase of η_{sep} for both pp and pPb events. $\Sigma[N_f, N_b]$ values are higher for pp events than pPb events. Smaller system size of the pp compared to the pPb collisions may enhance the fluctuations which in turn may increase the $\Sigma[N_f, N_b]$ values.

It is also observed that at larger distance between F and B window centers, $\eta_{sep} \sim 1$, $\Sigma[N_f, N_b]$ increases slowly for pp events which may indicate smaller contribution of long-range components compared to short-range components in the FB multiplicity fluctuations. This behavior of $\Sigma[N_f, N_b]$ observable as a function of η_{sep} is well explained in the framework of QGSM with independent identical strings [49].

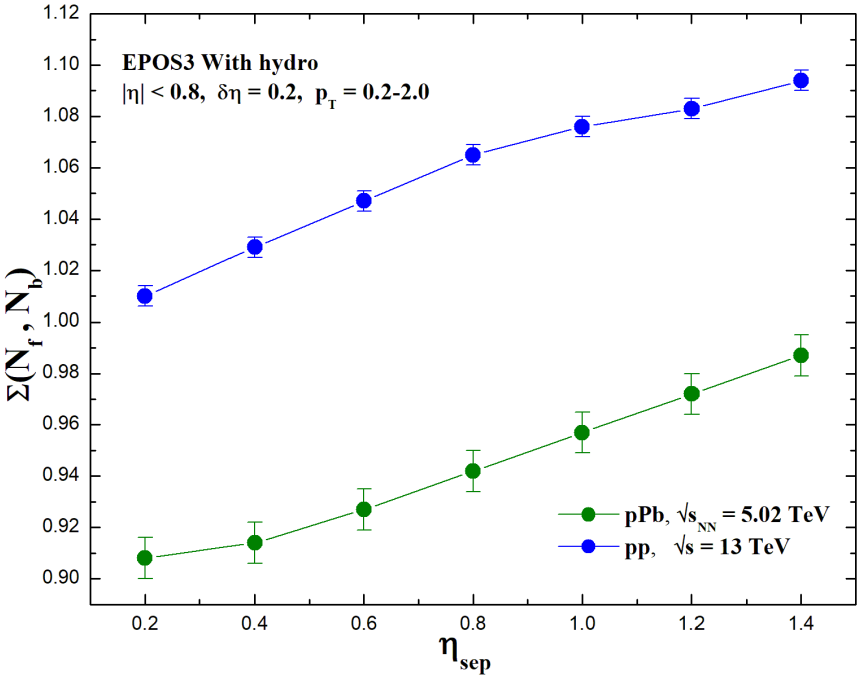

Fig. 3.31: $\Sigma[N_f, N_b]$ as a function of η_{sep} for window width $\delta\eta$ = 0.2 in EPOS3 simulated pp events at $\sqrt{s}$ = 13 TeV and pPb events at $\sqrt{s_{NN}}$ = 5.02 TeV.

3.9 Summary

By exploring FB multiplicity and momentum correlation, the present analysis highlights some important results and observations on long- and short-range correlations among produced charged particles in EPOS3 generated pp events at three center-of-mass energies $\sqrt{s}$ = 0.9, 2.76 and 7 TeV. The study reveals that:

- FB multiplicity and momentum correlation strengths decrease with η_{gap} for EPOS3 events (both with and without hydro) and LHC data (both ALICE and ATLAS data). The slope of this fall in correlation strength remains

approximately constant for three different energies for both simulated and experimental data.

- FB correlation increases with center-of-mass energy for EPOS3 simulated events. This feature is consistent with ALICE and ATLAS data. The energy dependence of FB correlation suggests that it might be due to the fact that the increase in long-range component of FB correlation is greater than its short-range component with the increase of multiple parton-parton interactions along with increasing center-of-mass energy [6].
- Like ALICE and ATLAS data, FB multiplicity and momentum correlation strength increases nonlinearly with η window width for EPOS3 events.
- For EPOS3 and ATLAS events correlation strength decreases with the increase of minimum transverse momentum. The observed rapid decrease of FB correlations with the increase of p_{Tmin} endorses the fact that at low p_T values, partonic strings may uniformly fragment in the longitudinal direction but at higher p_T, particles may be associated with jets showing weak correlations between different jets [50].

It has been seen that the overall trend of above dependences is in agreement with the experimental results from ALICE [15] and ATLAS [7]. However, better agreement with ATLAS data has been noticed in case of simulated pp events with hydrodynamical evolution of particles for all FB window pairs except the most central one.

Overall, we may conclude that the hybrid Monte Carlo model, EPOS3 remains consistent in explaining the LHC data in terms of FB multiplicity and momentum correlations qualitatively and explores the possible interplay between the soft and the hard processes in particle production in pp collisions along with the variation of collision energy density. The study also reflects that switching ON/OFF hydrodynamical evolution of bulk particles does not affect much the correlation strength.

We have extended the study of FB multiplicity and momentum correlations to higher center-of-mass energy in pp collisions ($\sqrt{s}$ = 13 TeV) and explored their behavior in asymmetric pPb collisions ($\sqrt{S_{NN}}$ = 5.02 TeV). To understand the contribution of different components in the EPOS3 model, we have calculated the FB correlation strengths for all charged particles as well as for particles originating from the core and

corona separately in both pp and pPb events. The results confirm similar FB correlation trends as seen at lower energies and the core-corona analysis further supports the consistency of EPOS3 in capturing system-size and energy-dependent correlation behavior.

It is interesting to note that $\delta\eta$-weighted average of FB multiplicity and momentum correlation strengths increases with center-of-mass energy up to 7 TeV, which is clearly visible and then tends to saturate at very high energies. We found that for the particles from corona, the $\delta\eta$-weighted average of FB correlations do not show any saturation trend whereas for particles form core are perfectly exhibiting the trend. It may be due to the dominance of the gluon-saturation effect at such higher center-of-mass energies.

In addition to the minimum-bias study of EPOS3 simulated events, the multiplicity-dependent summed-p_T FB correlation shows significant changes in different multiplicity ranges. FB summed-p_T correlation decreases as event multiplicity increases at a fixed η_{gap} and becomes lowest in high-multiplicity events. Our observation on multiplicity-dependent $b_{corr}(\sum p_T)$ in pp and pPb collisions provides valuable insights and further encourages experimental measurements.

The observed larger FB multiplicity and momentum correlation strength in pPb collisions with respect to pp collisions could be due to the fact that the initial asymmetry of the pPb collisions and the large system size with respect to the pp collisions may enhance the event-by-event fluctuations which in turn may increase the FB correlation.

We have also presented the behavior of a sophisticated correlation observable, $\Sigma[N_f, N_b]$ based on the charged particle multiplicities using EPOS3 simulated pp evets at $\sqrt{s}$ = 13 TeV and pPb events at $\sqrt{s_{NN}}$ = 5.02 TeV. Our study reveals that with the increase of multiplicity bin width, the values of $\Sigma[N_f, N_b]$ remain almost unchanged and with the increase of η_{sep} values, $\Sigma[N_f, N_b]$ values increase for both pp and pPb events. The property of independence of $\Sigma[N_f, N_b]$ variable with multiplicity bin width indeed reveals that $\Sigma[N_f, N_b]$ is insensitive to dynamical fluctuations of the system and also emphasize on the robustness of Σ observable as a strongly intensive quantity.

References

[1] M. Aaboud *et al.* (ATLAS Collaboration), Phys. Rev. C **95**, 064914 (2017).

[2] A. Capella and A. Krzywicki, Phys. Rev. D **18**, 4120 (1978).

[3] K. Alpgard *et al.* (UA5 Collaboration), Phys. Lett. **123** B, 361 (1983).

[4] S. L. Lim, Y. K. Lim, C. H. Oh, and K. K. Phua, Z. Phys. C **43**, 621 (1989).

[5] G. J. Alner *et al.* (UA5 Collaboration), Phys. Rep. **154**, 247 (1987).

[6] R. Ansorge *et al.* (UA5 Collaboration), Z. Phys. C **37**, 191 (1988).

[7] G. Aad *et al.* (ATLAS Collaboration), J. High Energy Phys. **07** (2012) 019.

[8] W. Braunschweig *et al.* (TASSO Collaboration), Z. Phys. C **45**, 193 (1989).

[9] P. Abreu *et al.* (DELPHI Collaboration), Z. Phys. C **50**, 185 (1991).

[10] M. Derrick *et al.* (HRS Collaboration), Phys. Rev. D **34**, 3304 (1986); Z. Phys. C **35**, 323 (1987).

[11] R. Akers *et al.* (OPAL Collaboration), Phys. Lett. B **320**, 417 (1994).

[12] T. Alexopoulos *et al.* (E735 Collaboration), Phys. Lett. B **353**, 155 (1995).

[13] B. B. Back *et al.* (PHOBOS Collaboration), Phys. Rev. C **74**, 011901 (2006).

[14] B. I. Abelev *et al.* (STAR Collaboration), Phys. Rev. Lett. **103**, 172301 (2009).

[15] J. Adam *et al.* (ALICE Collaboration), J. High Energy Phys. **05** (2015) 097.

[16] M. Mondal *et al.*, Phys. Part. Nucl. Lett. **14**, 459-464 (2017).

[17] A. Capella, U. Sukhatme, C.-I. Tan, and J. T. T. Van, Phys. Rep. **236**, 225 (1994).

[18] A. Capella and J. T. T. Van, Z. Phys. C **18**, 85 (1983).

[19] A. B. Kaidalov, Phys. Lett. **116** B, 459 (1982); Phys. At. Nucl. **66**, 1994 (2003).

[20] L. V. Bravina, J. Bleibel, and E. E. Zabrodin, Phys. Lett. B **787**, 146 (2018).

[21] N. S. Amelin, N. Armesto, M. A. Braun, E. G. Ferreiro, and C. Pajares, Phys. Rev. Lett. **73**, 2813 (1994).

[22] S. N. Belokurova and V. V. Vechernin, Phys. Part. Nucl. **51**, 319 (2020).

[23] V. Kovalenko and V. Vechernin, Proc. Sci., Baldin ISHEPP XXI (2012) 077.

[24] V. Kovalenko and V. Vechernin, DESY Conf. Proc. **82**, 691 (2014).

[25] P. Brogueira, J. Dias de Deus, and C. Pajares, Phys. Lett. B **675**, 308 (2009).

[26] L. McLerran, Nucl. Phys. **A699**, 73 (2002).

[27] Y. V. Kovchegov, E. Levin, and L. McLerran, Phys. Rev. C **63**, 024903 (2001).

[28] T. Lappi and L. McLerran, Nucl. Phys. **A832**, 330 (2010).

[29] N. Armesto, L. McLerran, and C. Pajares, Nucl. Phys. **A781**, 201 (2007).

[30] K. Werner, B. Guiot, Iu. Karpenko, and T. Pierog, Phys. Rev. C **89**, 064903 (2014).

[31] K. Werner, M. Bleicher, B. Guiot, Iu. Karpenko, and T. Pierog, Phys. Rev. Lett. **112**, 232301 (2014).

[32] B. Abelev *et al.* (ALICE Collaboration), Phys. Lett. B **726**, 164 (2013).

[33] B. Alessandro *et al.* (ALICE Collaboration), J. Phys. G **32**, 1295 (2006).

[34] M. A. Braun, R. S. Kolevatov, C. Pajares, and V. V. Vechernin, Eur. Phys. J. C **32**, 535 (2004).

[35] V. Vechernin, Nucl. Phys. **A939**, 21 (2015); Proc. Sci. QFTHEP2013 (**2013**) 055.

[36] Yi-An Li *et al.*, Phys. Rev. C 104, 044906 (2021).

[37] N. Armesto, M. A. Braun, and C. Pajares, Phys. Rev. C **75**, 054902 (2007).

[38] J. Aichelin and K. Werner, J. Phys. G **37**, 094006 (2010).

[39] V. Kovalenko, G. Feofilov, A. Puchkov, and F. Valiev, Universe **8**, 246 (2022).

[40] Larry McLerran, arXiv:0804.1736v1.

[41] F. Gelis, J. Phys. G **34**, S421 (2007).

[42] J. Adam *et al.* (ALICE Collaboration), Phys. Rev. Lett. **116**, 222302 (2016).

[43] A. Bzdak, Phys. Rev. C **80**, 024906 (2009).

[44] V. P. Konchakovski *et al.*, Phys. Rev. C **79**, 034910 (2009).

[45] M. A. Braun, C. Pajares, Phys. Rev. Lett. **85**, 4864 (2000).

[46] V. V. Vechernin, Theor. Math. Phys. **190**, 251 (2017).

[47] M. I. Gorenstein, Phys. Rev. C **84**, 014904 (2011).

[48] I. Sputowska (ALICE Collaboration), Proc. of MDPI, **10**, 14 (2019).

[49] V. Vechernin, Eur. Phys. J. Web Conf. 191 04011 (2018).

[50] B. Andersson, G. Gustafson, G. Ingelman, and T. Sjöstrand, Phys. Rep. **97**, 31 (1983).

Chapter – 4

Fractal Characteristic Studies in High Energy Collisions

4.1 Introduction

The study of fluctuations in the multiplicity and spatial distribution of produced particles in high energy collisions provides valuable information about the underlying dynamics of particle production mechanism. Among these, event-by-event fluctuations, which examine each collision individually rather than in aggregate, are especially significant, as they may reveal evidence of critical phenomena, phase transitions and possible formation of exotic states of matter such as the QGP.

It has been revealed by several studies that self-similarity and scale invariance might govern the dynamics of multiparticle production. The presence of self-similar fluctuations often hints at a deeper fractal structure embedded within the data, suggesting that the hadronization process may follow a cascading mechanism. Early studies by Białas and Peschanski [1, 2] introduced the concept of intermittency to describe power law scaling in factorial moments, leading to the interpretation of such fluctuations as fractal in nature. Following these foundational ideas, various methods such as G_q [3] and T_q [4] moments, Detrended Fluctuation Analysis (DFA) [5], Multifractal DFA (MF-DFA) [6] and diffusion entropy-based approaches [7- 12] have been employed to explore the multifractal properties of these events.

However, many of these methods face limitations, especially when applied to short time series, non-stationarity signals or finite-size datasets, which are common constraints in experimental high energy physics. In this context, the visibility graph (VG) method, a relatively recent and innovative approach grounded in complex network theory, emerges as a powerful alternative [13]. VG algorithm transforms a time series into a network that preserves essential structural features of the original data. Statistical and dynamical properties of the series, such as correlations, trends and fractality, are reflected in the resulting network structure, which enables the extraction of valuable knowledge about the underlying dynamics through the tools of complex network analysis. Above all, fractal time series can be transformed into scale-free networks [13-16], providing a direct bridge between time-series analysis and the language of complex systems.

The VG method has proven effective in a wide range of applications from turbulence [17] and traffic flow [18] to physiological signals [19-21] and financial markets [22]. In high energy physics, this method has been employed in earlier studies to analyze event-averaged distributions such as pseudorapidity spectra and void probabilities [23-26]. Subsequent studies have extended this approach to event-wise analyses [27], offering a more detailed understanding of the fluctuating behavior inherent in individual collisions. Yet to date, little attention has been given to apply the natural visibility graph (NVG) algorithm [13] for an event-by-event analysis of high energy heavy-ion collisions. The present study aims to address that gap.

In this chapter, we investigate the centrality dependence of fractal characteristics in multipion production process using nuclear emulsion data of ^{16}O-AgBr interactions at 60 AGeV and the transverse momentum dependence of fractal behavior using EPOS3 simulated pp events at $\sqrt{s}$ = 7 TeV.

4.2 Data Details

4.2.1 Emulsion data

The data used in this study were obtained from Illford G5 emulsion stacks exposed to ^{16}O beam of energy 60 A GeV from CERN SPS [28]. The nuclear emulsion technique, an age-old method for detecting charged particles, offers several advantages, as discussed in Chapter 2A. The details of the scanning and measurement procedures and sample size are provided in the same chapter.

4.2.2 EPOS3 events

The pQCD-inspired hybrid Monte Carlo event generator EPOS3 [29] uses Gribov-Regge multiple scattering framework for particle productions in high energy collisions. It effectively simulates both soft and hard processes in proton-proton and heavy-ion collisions. The details of the particle production mechanism are discussed in Chapter 2B.2.

For this study, we used 3×10^6 minimum-bias EPOS3 generated pp events at $\sqrt{s} = 7$ TeV, with hydrodynamical evolution of particles. Further, events were selected with at least three charged particles within the kinematic range $p_T > 0.1$ GeV/c and $|\eta| < 2.5$, ensuring the inclusion of charged particles from both soft and hard processes.

4.3 Visibility Graph Technique

The visibility graph (VG) algorithm maps a time series X into a complex network, where each data point X_i (i^{th} point of the time series) is treated as a node [13]. Two nodes are connected if they can see each other, namely, a straight visibility line exists between them.

Formally, two arbitrary data points (t_a, X_a) and (t_b, X_b) are said to be visible to each other if every intermediate point (t_c, X_c) satisfies the following condition:

$$X_c \leq X_b + \frac{(X_a - X_b)}{(t_b - t_a)}(t_b - t_c) \tag{4.1}$$

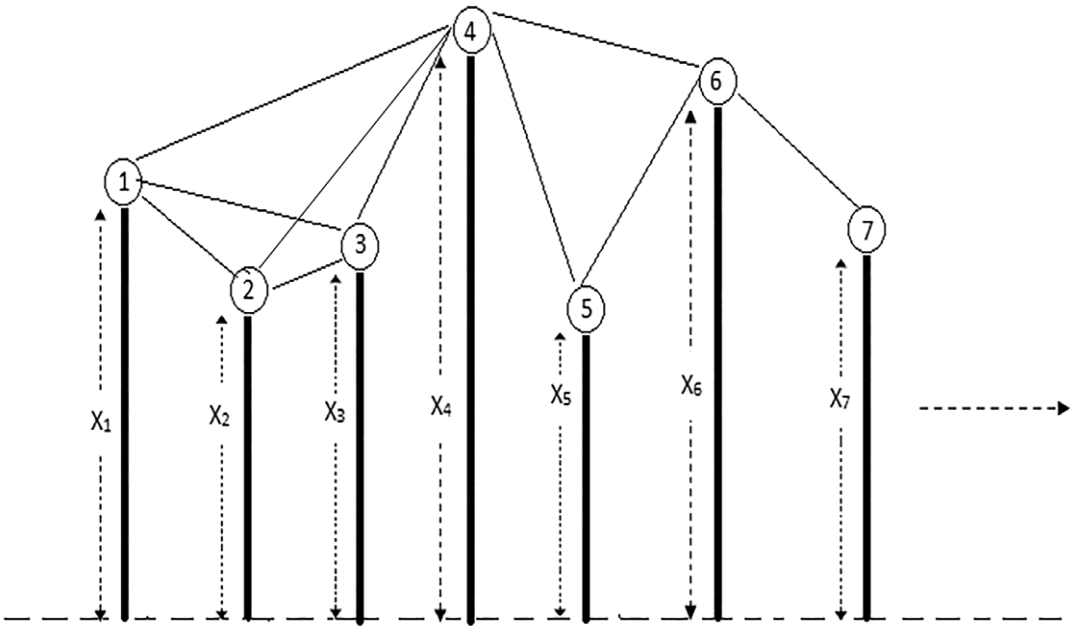

Fig. 4.1: Schematic representation of visibility graph constructed from a time series X.

Figure 4.1 illustrates the visibility algorithm. The numbers within the circles denote the nodes of the graph and the lines between them represent connections based on the

visibility condition. The degree of a node refers to the number of edges or connections it has with other nodes. In the figure, node 4 is connected to nodes 1, 2, 3, 5 and 6, giving it a degree of 5. It is evident that consecutive data points in the series always maintain visibility; hence, all sequential nodes are connected. The resulting network is undirected, as no direction is assigned to the links. Notably, the visibility criterion given by Eq. (4.1) is invariant under rescaling of both horizontal and vertical axes, as well as under horizontal and vertical translations [13].

4.3.1 Power of scale-freeness of visibility graph – PSVG

For a network constructed from a time series, the degree distribution $P(k)$ represents the fraction of nodes with degree k. If a network contains n nodes in total and n_k of them have degree k, then the degree distribution is defined as:

$$P(k) = \frac{n_k}{n}$$

The scale-freeness property of Visibility Graph implies that the degree distribution of its nodes follows a power law behavior:

$$P(k) \sim k^{-\lambda_p} \tag{4.2}$$

Here, λ_p is a constant known as the Power of Scale-Freeness of Visibility Graph, PSVG. This exponent reflects the complexity and fractal nature of the underlying time series [13, 15-16].

Furthermore, the Hurst exponent H, which characterizes the autocorrelation in a time series, can be estimated from PSVG. Recent studies [30] have confirmed that the Hurst exponent is an effective indicator of phase transitions in magnetization time series.

According to Lacasa et al. [15], the relationship between λ_p and H depends on the type of process that generated the time series.

- For fractional Brownian motion (fBm):

$$\lambda_p = 3 - 2H \tag{4.3}$$

- For fractional Gaussian noise (fGn), which consists of the increments of fBm:

$$\lambda_p = 5 - 2H \tag{4.4}$$

The Hurst exponent H lies in the interval $0 < H < 1$. A value of $H = 0.5$ indicates an uncorrelated (random) process. When $H > 0.5$, the time series exhibits persistence (positive correlations), while $H < 0.5$ indicates anti-persistence (negative correlations or anti-correlated behavior).

4.3.2 Network average clustering coefficient

In a visibility graph, nodes may exhibit a tendency to form clusters, indicating a local interconnectedness within the network. This behavior is quantified by a metric known as the network clustering coefficient.

Watts and Strogatz [31] proposed a method to compute this coefficient. Consider a node i with degree v, meaning node i has v neighbors. The maximum number of possible connections among these v neighbors is given by

$$\frac{v(v-1)}{2} .$$

This represents the case where each neighbor of node i is connected to every other neighbor. Let C_i denote the local clustering coefficient of node i, defined as the ratio of the actual number of connections among its neighbors to the maximum possible number.

The average clustering coefficient for a network of n nodes is then given by

$$C = \frac{1}{n}\sum_{i=1}^{n} C_i. \tag{4.5}$$

4.4 Study of Fractal Characteristics in Nuclear Emulsion Data

4.4.1 Centrality selection

Target recoil protons, referred to as grey particles in nuclear emulsion terminology, represent the low-energy component of the intra-nuclear cascade in high energy interactions. Consequently, the number of grey particles (n_g) produced in such

interactions is considered an indirect measure of collision centrality [32]. A higher number of grey particles generally correspond to a more central collision. To investigate the centrality dependence of fluctuation phenomena, the experimental data of ^{16}O-AgBr interactions at 60 A GeV were divided into two sub-samples based on the number of grey particles produced in each event. The details of this classification are presented in Table 4.1.

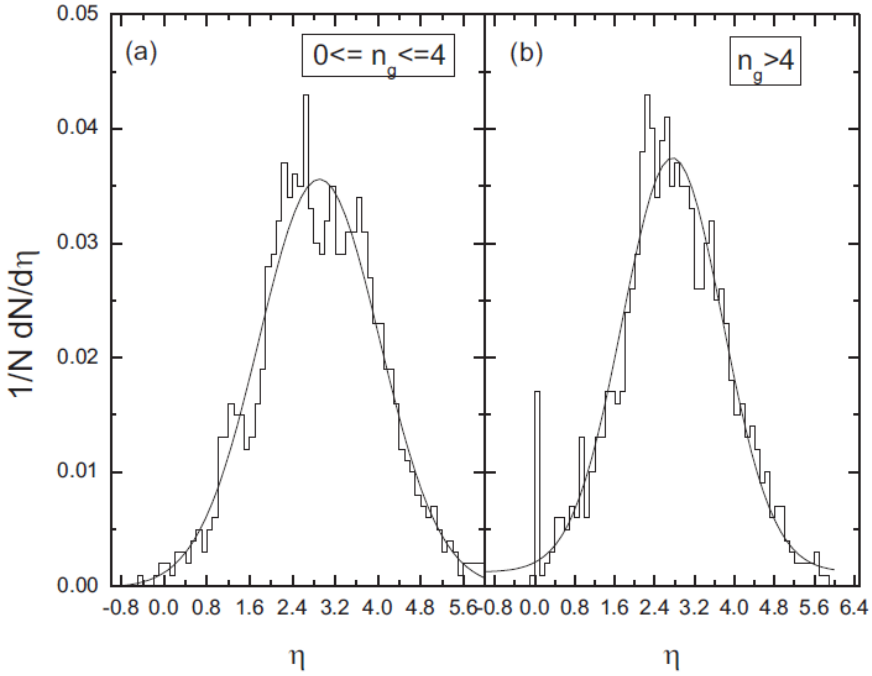

Fig. 4.2: Pseudorapidity distribution of the ^{16}O-AgBr interactions at 60 A GeV for (a) Sub-sample-I and (b) Sub-sample-II. The smooth lines in the diagrams represent the Gaussian fits to the corresponding distribution.

4.4.2 Pseudorapidity distributions

The overall pseudorapidity distributions for Sub-sample-I ($0 \leq n_g \leq 4$) and Sub-sample-II ($n_g > 4$) of ^{16}O-AgBr interactions at 60 A GeV are shown in Fig. 4.2(a) and Fig. 4.2(b) respectively. In both cases, the distributions are smooth and resemble a Gaussian shape. The central value of pseudorapidity (η_{centre}) is observed to be around 3 units. For the present analysis, a pseudorapidity window of width $\Delta\eta = 4$ centered at η_{centre} has been considered.

4.4.3 Single event pseudorapidity distributions and detrending

The single event η-distributions are presented in Fig. 4.3(a) and Fig. 4.4(a) for an arbitrarily selected event from each sub-sample. Both distributions exhibit significant fluctuations. However, these fluctuations tend to vanish when the single event distribution functions are averaged over many events. To effectively capture such fluctuations, the single event pion distribution functions must be transformed into their corresponding visibility graphs on an event-by-event basis. It is important to note that the average trend, often regarded as the background, can undesirably hinder the visibility between η-bins (nodes in the VG). Specifically, η-bins on one side of the peak may obscure those on the opposite side, thereby affecting the construction of the graph.

To address this issue, we apply the method of successive differences to the bin counts:

$$y(\eta_i) = dn(\eta_{i+1}) - dn(\eta_i)$$

As required by the visibility graph (VG) technique, the modified distribution is then projected onto the positive (y, η) plane. Fig. 4.3(b) and Fig. 4.4(b) show the modified forms of the distributions corresponding to the pseudorapidity distributions presented in Fig. 4.3(a) and Fig. 4.4(a) respectively. It is evident that this modification effectively detrends the background, while preserving the relative fluctuations present in single events.

Table 4.1: Details of sub-samples of data for ^{16}O-AgBr interactions at 60 A GeV and linear fit parameters corresponding to the plots of Fig. 4.5 and sample average of average clustering coefficients for both the sub-samples.

Sub-samples	n_g range	λ_p	R^2	Sample Avg. of Avg. clustering coefficient
Sub-sample-I	$0 \leq n_g \leq 4$	3.0 ± 0.2	0.96	0.83
Sub-sample-II	$n_g > 4$	2.6 ± 0.2	0.98	0.80

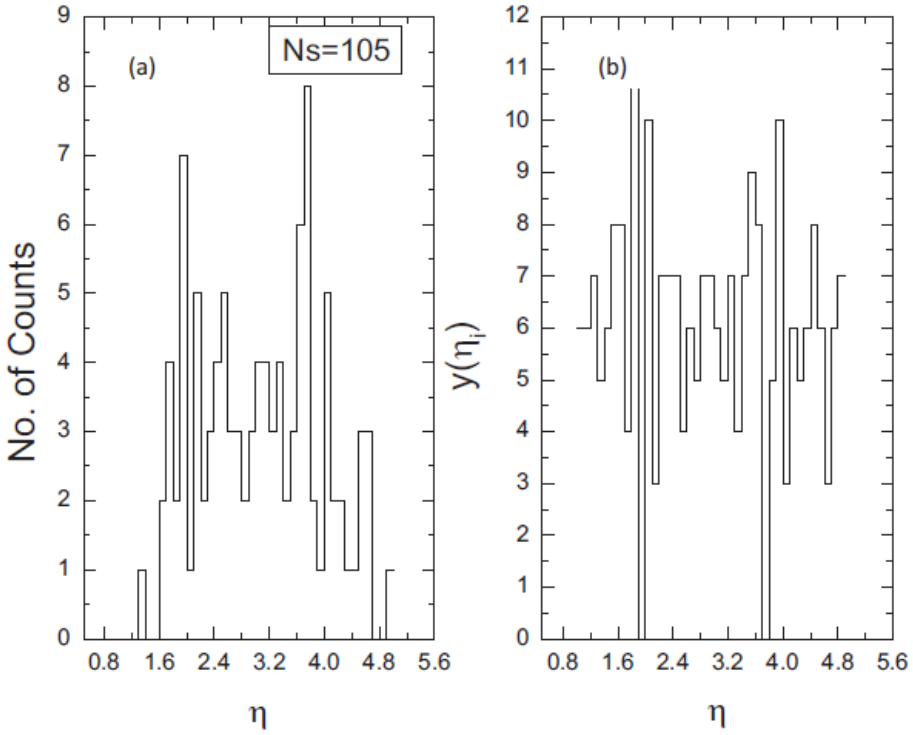

Fig. 4.3: The single event (pion multiplicity, N_s = 105) (a) pseudorapidity distribution and (b) modified pseudorapidity distribution of Sub-sample-I of ^{16}O-AgBr interactions at 60 A GeV.

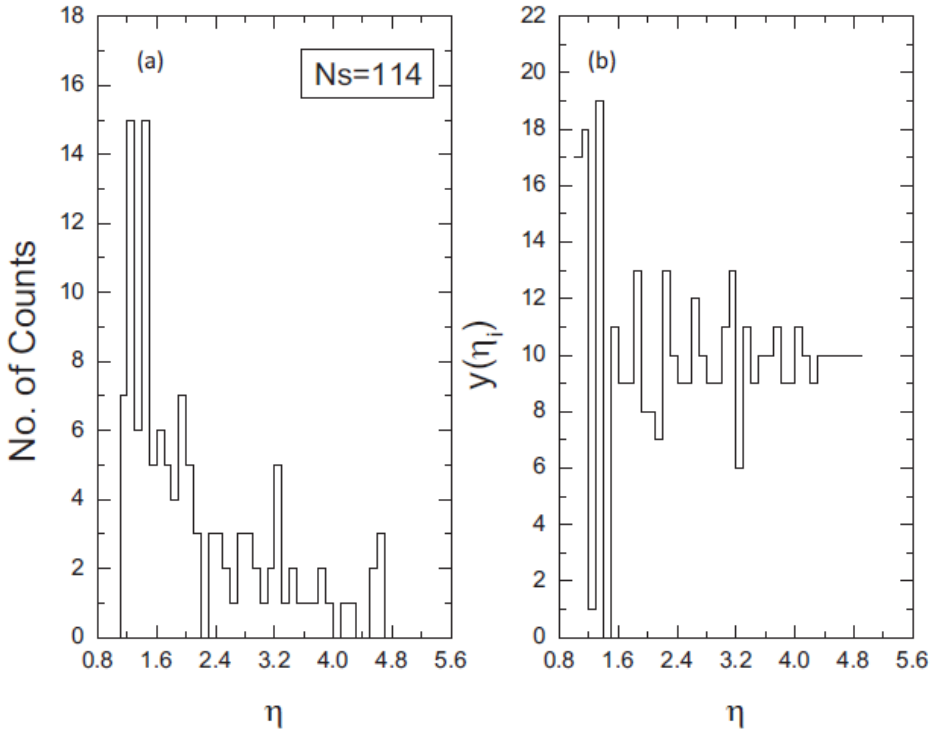

Fig. 4.4: The single event (pion multiplicity, N_s = 114) (a) pseudorapidity distribution and (b) modified pseudorapidity distribution of Sub-sample-II of ^{16}O-AgBr interactions at 60 A GeV.

4.4.4 Visibility graph and its power of scale-freeness property

On an event-by-event basis, these modified η-distributions are converted into the corresponding VGs. The degree denoted by k represents the number of connections a given node has with other nodes in the VG of a single event. An overall degree distribution $P(k)$ for the entire event sample is then constructed by combining the single event distributions together. We have plotted $\ln P(k)$ versus $\ln(1/k)$ in Fig. 4.5(a) and Fig. 4.5(b) respectively for Sub-sample-I and Sub-sample-II of ^{16}O-AgBr interactions at 60 A GeV. It is evident from these plots that the power law relationship described by Eq. (4.2) is satisfied by our experimental data. This result provides strong evidence for the fractal nature of fluctuation patterns in multipion production in ^{16}O-AgBr interactions at 60 A GeV.

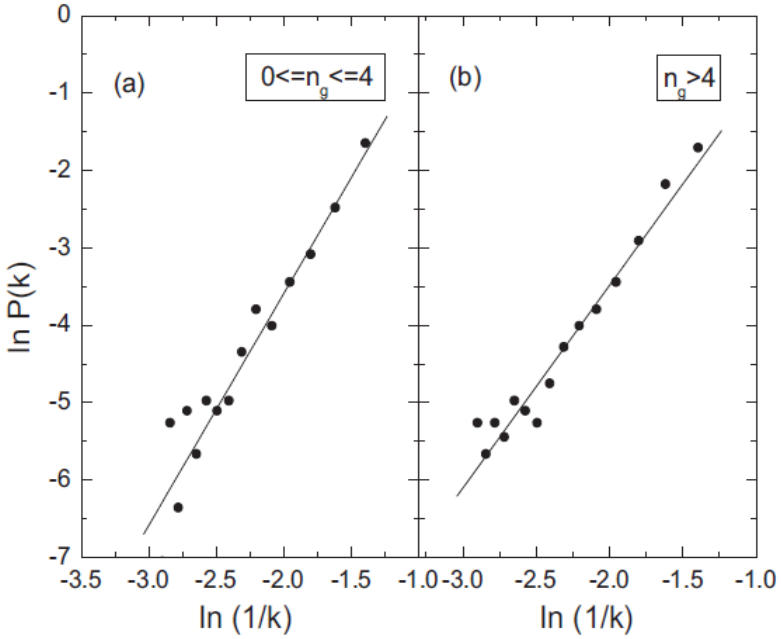

Fig. 4.5: Variation of $\ln P(k)$ versus $\ln(1/k)$ for (a) Sub-sample-I and (b) Sub-sample-II in case of ^{16}O-AgBr interactions at 60 A GeV. Solid lines correspond to linear fits.

To determine the Power of Scale-freeness of Visibility Graph (PSVG), denoted as λ_p, we performed best linear fits to the plots presented in Fig. 4.5. The slope of each linear fit corresponds to the value of λ_p and the associated fitting parameters are summarized in Table 4.1. Since PSVG is an indicator of fractality, the values listed in Table 4.1 suggest that the degree of fractal behavior decreases with the increase of centrality in ^{16}O-AgBr

interactions at 60 A GeV. It may be worth mentioning that similar centrality-dependent trends were previously reported by Bhaduri *et al.* [33] in the case of $\pi^- - AgBr$ interactions at 350 GeV/c.

4.4.5 Clustering coefficient and its centrality dependence

To extract the physical parameter associated with the dynamics of particle production, we have computed the average clustering coefficient C for each event using Eq. (4.5), following the method proposed by Watts and Strogatz [31]. This calculation was performed on visibility graphs constructed from two event samples representing different centralities. The event-by-event variation of the average clustering coefficient is shown in Fig. 4.6(a) and Fig. 4.6(b) for Sub-sample-I and Sub-sample-II respectively. It

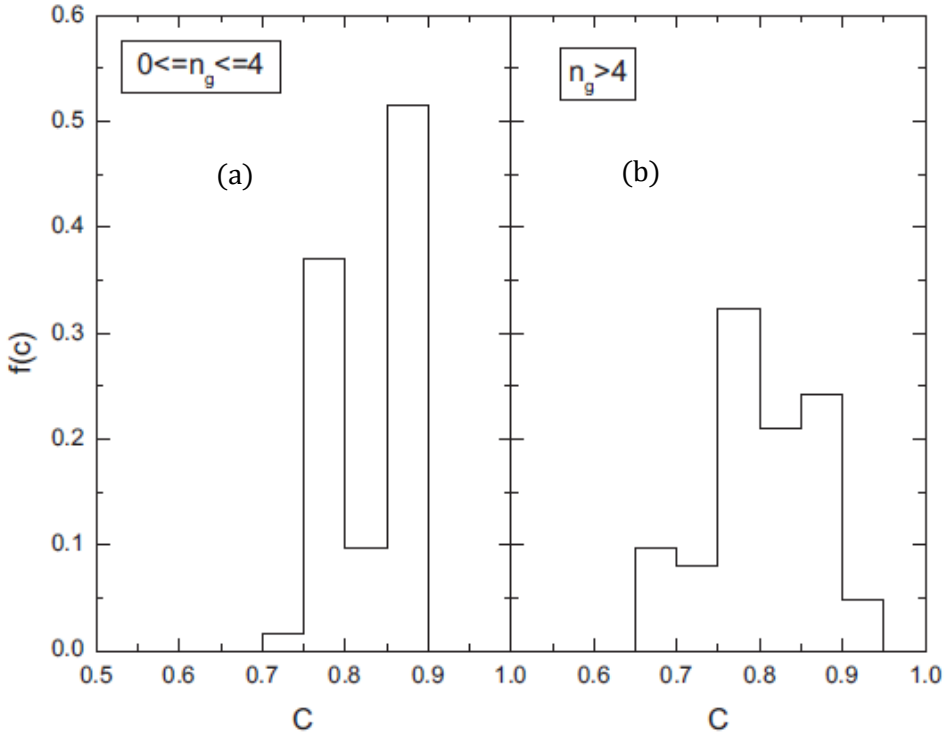

Fig. 4.6: Event-by-event variation of average clustering coefficient for (a) Sub-sample-I and (b) Sub-sample-II in case of ^{16}O-AgBr interactions at 60 A GeV.

is evident from Fig. 4.6 that the average clustering coefficient varies from event-to-event. However, the fluctuations are more pronounced in case of Sub-sample-II than in Sub-sample-I. This observation suggests that in events corresponding to lower target excitation (Sub-sample-I), the produced pions tend to cluster in a relatively

consistent manner. In contrast, for higher target excitation (Sub-sample-II), the clustering behavior varies widely from event-to-event. The event-averaged values of the average clustering coefficient for both sub-samples have been calculated and listed in Table 4.1. These mean values of the average clustering coefficient further indicate that the mechanisms underlying multipion production differ between the two centrality classes.

4.4.6 Hurst exponent and identification of source

The Hurst exponent (H) has been estimated from the PSVG (λ_p) values using the approach proposed by Lacasa *et al.* [15], along with the known theoretical range of H ($0 \leq H \leq 1$). For Sub-sample-I, the λ_p value suggests the applicability of Eq. (4.4) for determining H, and the corresponding results are presented in Table 4.2. In contrast, for Sub-sample-II, Eq. (4.3) has been employed for the same purpose and the estimated H value is included in Table 4.2. According to the framework outlined by Lacasa *et al.* [15], the event-by-event fluctuations in Sub-sample-I are attributed to fractional Gaussian noise (fGn), which is composed by the increments of a fractional Brownian motion (fBm). On the other hand, the fluctuations in Sub-sample-II are directly characterized by fractional Brownian motion (fBm) itself. As shown in Table 4.2, the Hurst exponent for Sub-sample-I exceeds 0.5, indicating a persistent or positively correlated process. In contrast, the H value for Sub-sample-II is less than 0.5, which reflects an anti-persistent or negatively correlated process.

Table 4.2: Values of Hurst exponent and probable sources for different centrality events.

Sub-samples	n_g range	H	Probable source
Sub-sample-I	$0 \leq n_g \leq 4$	1	fGn
Sub-sample-II	$n_g > 4$	0.2	fBn

4.5 Study of Fractal Characteristics in EPOS3 simulated *pp* events at $\sqrt{s}$ = 7 TeV

In order to capture event-by-event fluctuations in pp collisions at $\sqrt{s}$ = 7 TeV, the single event pseudorapidity distribution is transformed into its corresponding visibility graph. Following the same procedure as before, we applied the method of successive differences to the bin counts in order to modify the single-event η-distribution. This was done to detrend the background while preserving the relative fluctuations present in individual events. Figure 4.7 (a) and Fig. 4.7 (b) respectively show the original and modified pseudorapidity distribution of an arbitrarily selected event.

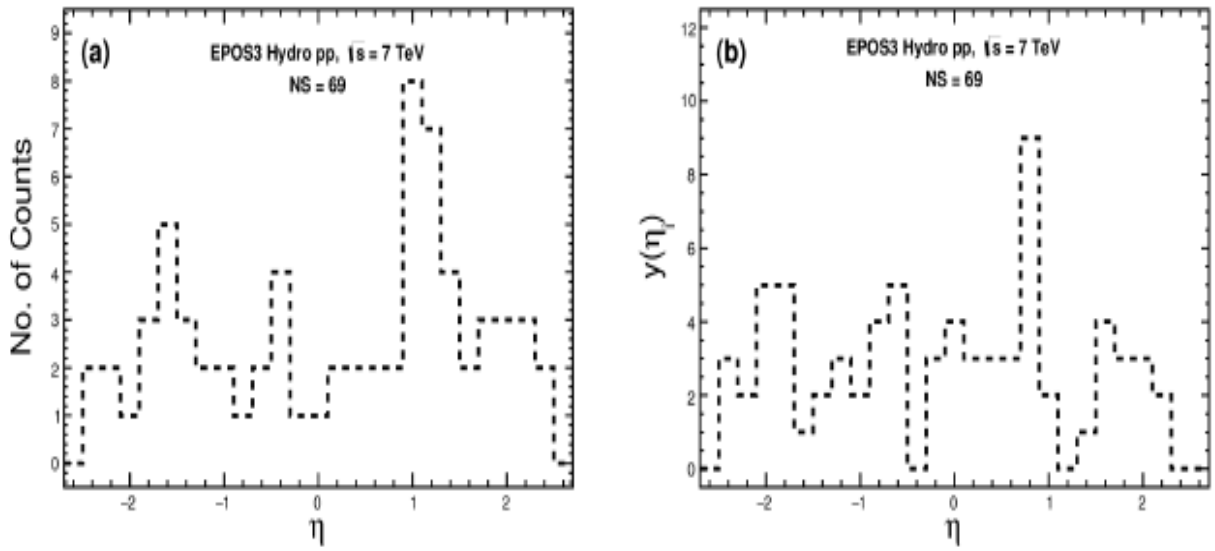

Fig. 4.7: (a) Pseudorapidity distribution (charged particle multiplicity, NS = 69) and (b) modified pseudorapidity distribution of an arbitrarily chosen event from EPOS3 simulated with hydro pp events at $\sqrt{s}$ = 7 TeV.

The modified η-distributions for the entire event sample are then converted into the corresponding visibility graphs on an event-by-event basis. The overall degree distribution $P(k)$ for the full event sample is constructed by aggregating the degree distributions obtained from individual events.

We have presented $p(k)$ versus k plot for $p_{Tmin} > 0.1$ GeV/c in Fig. 4.8. It is clear from this figure that the degree distributions for the chosen p_{Tmin} value follow a power law behavior consistent with Eq. (4.2). This observation supports the presence of fractal

characteristics in the fluctuation patterns of multiparticle production within small collision systems. In high energy collisions, an increase in particle transverse momentum typically indicates a gradual transition from soft processes to hard processes. To study the variation in fractality or complexity in particle production with the transverse momentum of produced particles, we have analyzed fractal characteristics for three additional thresholds for the charged-particle transverse momentum (p_{Tmin}), i.e., p_{Tmin}= 0.3, 0.5 and 0.7 GeV/c. The $p(k)$ versus k plots corresponding to different p_{Tmin} values are presented in Fig. 4.8. To enhance visual clarity, $p(k)$ values are added with multiple of a constant (α = 0.01) for different p_{Tmin} values. Figure 4.8 clearly demonstrates that the power law behavior described by Eq. (4.2) holds consistently for all transverse momentum (p_{Tmin}) thresholds, which confirms that the EPOS3 simulated pp events at $\sqrt{s}$ = 7 TeV exhibit fractal characteristics in the fluctuation patterns of multiparticle production.

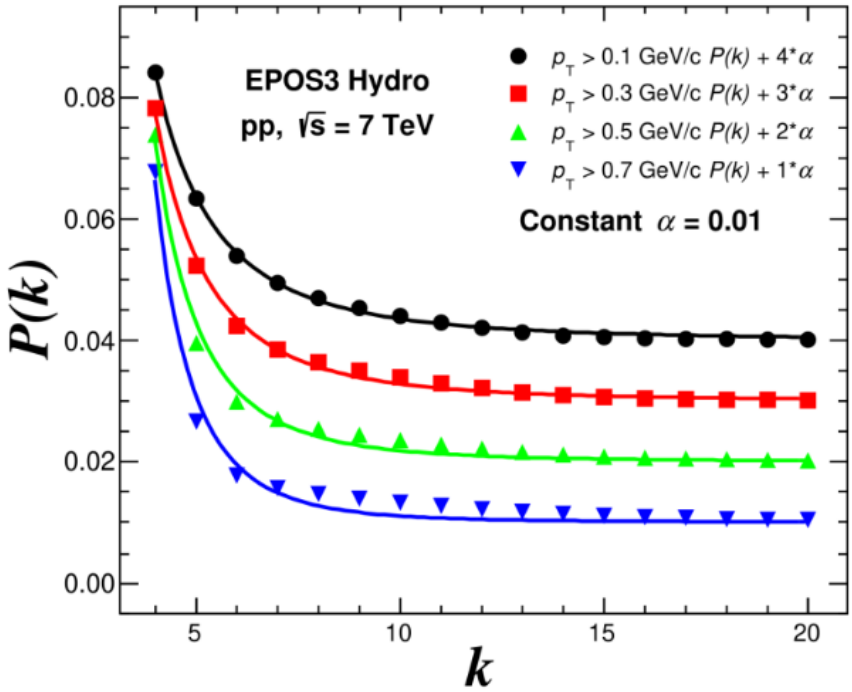

Fig. 4.8: Degree distribution of visibility graph for EPOS3 simulated with hydro pp events at $\sqrt{s}$ = 7 TeV for four different p_{Tmin}values. Solid lines correspond to nonlinear fits.

To determine the values of PSVG, we have fitted each degree distribution [$p(k)$ vs. k] with a nonlinear function based on Eq. (4.2) using the MINUIT program within the

ROOT data analysis framework [34], as shown in the figure by the solid line. The corresponding PSVG values for four different p_T thresholds, extracted from the fit of each graph along with χ^2/NDF (which suggests acceptable goodness of fit) are tabulated in Table 4.3.

Table 4.3: Values of PSVG parameter and χ^2/NDF for different p_{Tmin} values for EPOS3 simulated pp events at $\sqrt{s}$ = 7 TeV.

p_{Tmin} (GeV/c)	λ_p	χ^2/NDF
0.1	2.75 ± 0.05	2.605×10^{-7}
0.3	3.08 ± 0.06	5.955×10^{-7}
0.5	3.7 ± 0.1	2.073×10^{-6}
0.7	4.4 ± 0.1	3.537×10^{-6}

From Table 4.3 we can notice that the PSVG values show an increasing trend with the increase of minimum transverse momentum (p_{Tmin}). This suggests that as the system gradually transits from soft processes to hard processes, the complexity of particle production also increases.

4.6 Summary

We have investigated the fractal nature of multiparticle production in nucleus–nucleus collisions at SPS energy using a robust non-linear method known as the Visibility Graph technique.

Our findings are:

- Pion fluctuations on an event-by-event basis exhibit fractal characteristic. Moreover, the Power of Scale-freeness of the Visibility Graph (PSVG) is observed to decrease with increasing event centrality, indicating a centrality-dependent fractal behavior in ^{16}O-AgBr interactions at 60 A GeV.

- To further explore the underlying dynamics, the average clustering coefficient C have been estimated from the visibility graphs corresponding to two different

centrality classes. The mean values of this coefficient highlight that the dynamics of particle production is different for different centrality event-samples.

- The study of the Hurst exponent (H) provides additional insight into the nature of these fluctuations. Results indicate that the origin of event-by-event fluctuations differs between centrality classes. According to the model proposed by Lacasa et al. [15], lower-centrality events are likely governed by fractional Gaussian noise (fGn), a process derived from the increments of fractional Brownian motion (fBm), while higher-centrality events are more directly characterized by fBm itself.

- The estimated Hurst exponent values suggest that lower-centrality events reflect a persistent (positively correlated) process, whereas higher-centrality events exhibit anti-persistent (negatively correlated) behavior. These findings suggest the presence of distinct dynamical regimes in pion production for the two centrality classes considered in high energy collisions.

This analysis contributes new insights into multipion production in nucleus–nucleus collisions at SPS energy.

Additionally, the event-by-event analysis of EPOS3 generated pp events at $\sqrt{s}$ = 7 TeV reveals that the fluctuations in charged-particle production also follow a fractal pattern. The study of transverse momentum dependence of this fractal nature also indicates that with the gradual transition from soft processes to hard processes, particle production becomes more complex in nature.

References

[1] R. Peschanski, A. Bialas, Nucl. Phys. B **273**, 703 (1986).

[2] R. Peschanski, A. Bialas, Nucl. Phys. B **308**, 857 (1988).

[3] R. C. Hwa, Phys. Rev. D **41**, 1456 (1990).

[4] F. Takagi, Phys. Rev. Lett. **72**, 32 (1994).

[5] C. K. Peng *et al*., Phys. Rev. E **49**, 1685 (1994).

[6] J. W. Kantelhardt *et al*., Physica A **316**, 87 (2002).

[7] N. Scafetta *et al*., Phys. Rev. E **66**, 036130 (2002).

[8] J. Qi *et al*., Phys. Rev. E **84**, 066114 (2011). doi: 10.1103/PhysRevE.84.066114.

[9] W. Zhang *et al*., Phys. Rev. E **86**, 056107 (2012). doi: 10.1103/PhysRevE.86.056107.

[10] X. Pan *et al*., Phys. Lett. A **378**, 2591 (2014).

[11] X. Pan *et al*., PLoS One **9**(12), e116128 (2014). doi: 10.1371/journal.pone.0116128.

[12] Y. Yang *et al*., Chin. J. Phys. **55**, 2325 (2017).

[13] L. Lacasa *et al*., Proc. Natl. Acad. Sci. USA **105**(13), 4972 (2008).

[14] A. L. Barabási *et al*., Science **286**(5439), 509 (1999).

[15] L. Lacasa *et al*., Europhys. Lett. **86**(3), 30001 (2009).

[16] M. Ahmadlou *et al*., Physica A **391**(20), 4720 (2012).

[17] C. Liu *et al*., Physica A **389** (13), 2675 (2010). doi:10.1016/j.physa.2010.02.043

[18] M. Andjelković *et al*., Phys. Rev. E **91**(5), 052817 (2015).

[19] S. Jiang *et al*., Appl. Phys. Lett. **102**(25), 253702 (2013). doi:10.1063/1.4812645

[20] A. Bhaduri, D. Ghosh, Front. Physiol. **7**, 44 (2016). doi:10.3389/fphys.2016.00044

[21] A. Bhaduri *et al*., Physica A **482**, 786 (2017). doi:10.1016/j.physa.2017.04.091

[22] Y. Yang *et al.*, Physica A **388**(20), 4431 (2009). doi:10.1016/j.physa.2009.07.016

[23] S. Bhaduri and D. Ghosh, Mod. Phys. Lett. A **31** (27), 1650158 (2016).

[24] A. Bhaduri and D. Ghosh, Int. J. Mod. Phys. A **31** (35), 1650185 (2016).

[25] S. Bhaduri et al., Eur. Phys. J. A 53, 135 (2017). doi:10.1140/epja/i2017-12332-4

[26] A. Bhaduri, S. Bhaduri, and D. Ghosh, Phys. Part. Nucl. Lett. **14**(4), 576 (2017).

[27] P. Mali *et al.,* Mod. Phys. Lett. A **32**(8), 1750024 (2017).

[28] D. Ghosh *et al*., Nucl. Phys. A **707**, 213-223 (2002).

[29] K. Werner, B. Guiot, Iu. Karpenko, and T. Pierog, Phys. Rev. C **89**, 064903 (2014).

[30] L. Zhao *et al*., PLoS One **12**(1), e0170467 (2017).

[31] D. J. Watts, S. H. Strogatz, Nature **393**, 440-442 (1998).

[32] J. Babecki *et al*., Acta Phys. Pol. B **9**, 401 (1978).

[33] S. Bhaduri and D. Ghosh, Acta Phys. Pol. B **48** (4), 741 (2017).

[34] F. James and M. Roos, Comput. Phys. Commun. 10, 343–367 (1975).

Chapter – 5

Evidence of Chaos in Multiparticle Production

5.1 Introduction

In high energy collisions, a large number of particles are generated and distributed throughout the available phase space in various ways. These collisions exhibit key features such as two particle, three particle and multiparticle correlations, multifractality and intermittency, suggesting that large fluctuations arise primarily from dynamic processes governing particle production [1-2]. The genuine multiparticle correlations originating from collective effects may lead to high multiplicity events with specific features, e.g., ring-like, pencil-like (jet) structures [3-5]. However, to reveal complete information about particle production mechanism, it is essential to analyze event-by-event fluctuations in addition to the fluctuations averaged over event sample. In previous intermittency analysis [6], vertically averaged horizontal moments were used to study only spatial fluctuations. In contrast, horizontally averaged vertical moments capture only event-space fluctuations, that is, the variations from event-to-event.

Hwa introduced a novel approach, known as erraticity analysis, to explore the fluctuation patterns of the produced particles in high energy heavy-ion collisions [7-9]. This method simultaneously incorporates both spatial and event-space fluctuations providing deeper understanding of the underlying production dynamics. The Erraticity analysis is especially helpful in identifying chaoticity in production dynamics and clarifying the origin of intermittency. It has been applied in many different fields, such as multiparticle production in high energy interactions [7-9, 11-18], classical chaos theory [10], phase transitions[19] and even physiological studies like heartbeat analysis [20].

In this chapter, we aim to investigate the chaotic nature of particle production in ^{16}O-AgBr interactions at 60 A GeV using the method of erraticity analysis. The study is also extended to explore the system-size and energy dependence of chaotic behavior through erraticity analysis in EPOS3 simulated pp events at $\sqrt{s}$ = 13 TeV and pPb events at $\sqrt{s_{NN}}$ = 5.02 TeV.

5.2 Experimental Data Details

Tha data used for erraticity analysis are taken from Illford G5 emulsion plates exposed to ^{16}O beam of energy 60 A GeV from CERN SPS [21]. Nuclear emulsion detector [22] has several advantages such as it offers extremely high spatial resolution allowing precise tracking of charged particles. Also this detector records and permanently stores the information of charged particles over the 4π geometry which enables long-term observation and analysis of particle interactions in finer phase space bins. The details of scanning, measurement technique and data description are given in Chapter 2A.

5.3 Details of Simulated Events

- **IEH events**

We have generated Monte Carlo events according to the independent emission hypothesis (IEH), based on the following assumptions:

i. Pseudorapidity values are generated randomly for each shower track. As a result, all particles are independent of each other.

ii. The multiplicity distribution and pseudorapidity distribution of Monte Carlo events reproduce those of the experimental ensemble**.**

We have simulated 2500 events of ^{16}O-AgBr interactions at 60 A GeV using IEH MC method.

- **UrQMD events**

The Ultra-Relativistic Quantum Molecular Dynamics (UrQMD) [23] is based on microscopic transport approach, where particles propagate through space and interact with each other according to probabilistic rules governing particle scattering, decay and resonance formation. A detailed description of the model, the data used in this study and its validation are provided in Chapter 2B.3.

- **EPOS3 events**

The EPOS3 [24] event generator is based on a hybrid approach that combines microscopic parton-based multiple scattering with a hydrodynamic evolution,

where particles interact through flux-tube fragmentation, collective flow and hadronic cascade dynamics. The details of the event generator are porvided in Chapter 2B.2.

For our study, we have used 1×10^5 minimum-bias EPOS3 generated pp events at $\sqrt{s} = 13$ TeV and pPb events at $\sqrt{s_{NN}} = 5.02$ TeV with hydrodynamical evolution of particles.

5.4 Method of Erraticity Analysis

The single particle density distribution in pseudorapidity space is non-flat. As the shape of this distribution influences the scaling behavior of the factorial moments, we have used the 'cumulative' variable [25] X_η instead of η. The cumulative variable X_η is given by

$$X_\eta = \int_{\eta_1}^{\eta} \rho(\eta')\, \partial\, \eta' / \int_{\eta_1}^{\eta_2} \rho(\eta')\, \partial\eta', \tag{5.1}$$

where η_1 and η_2 are two extreme points in the distribution $\rho(\eta)$. The corresponding region of investigation for X_η then becomes (0, 1).

Dividing X_η space into M bins, the horizontal factorial moments for each event are calculated according to the following formula:

$$f_q^e(M) = \frac{1}{M} \sum_{i=1}^{M} n_i\, (n_i - 1) \dots\dots\dots\dots\dots (n_i - q + 1), \tag{5.2}$$

where n_i is the number of particles in the i^{th} bin for e^{th} event and q is the order for spatial fluctuation. The normalized factorial moments for the e^{th}event are then defined as

$$F_q^e(M) = f_q^e(M) / (f_1^e(M))^q. \tag{5.3}$$

Since $F_q^e(M)$ fluctuates from event-to-event, one obtains a distribution $P\left(F_q^e\right)$ for the whole event sample. Let the average of $F_q^e(M)$ determined from $P\left(F_q^e\right)$ be denoted by $\langle F_q^e(M)\rangle$ and $\Phi_q(M) = F_q^e(M) / \langle F_q^e(M)\rangle$.

In order to quantify the degree of that fluctuation, a new normalized moment is defined as [7, 8]

$$C_{p,q}(M) = \langle \Phi_q^p(M) \rangle, \tag{5.4}$$

where p is a positive real number. If $C_{p,q}(M)$ has a power law behavior as the division number M goes to infinity

$$C_{p,q}(M) \propto M^{\psi_q(p)}, \; M \to \infty, \tag{5.5}$$

then the behavior is referred to as erraticity and $\psi_q(p)$ is referred to as the erraticity exponent.

The moments $C_{p,q}(M)$ capture the event-to-event fluctuations of F_q^e, which describe spatial patterns that vary with bin size. If these fluctuations scale with bin size, the erraticity exponent $\psi_q(p)$ provides a measure of the self-similar dynamics and their fluctuations [26]. A constant spatial pattern across events would result in $\psi_q(p) = 0$, while larger values indicate more erratic fluctuations.

Erraticity is characterized by the slope of $\psi_q(p)$ at $p = 1$, called the entropy index μ_q, which is defined as [7, 8]:

$$\mu_q = \frac{d}{dp} \psi_q(p)|_{p=1}. \tag{5.6}$$

Entropy index μ_q describes the width of fluctuations and is related to entropy in event space as $S_q = \ln N M^{-\mu_q}$ where one can think of the event space as a one-dimensional space with N sites. Since S_q is defined in event space; one may call it "eventropy" [7, 8]. A high eventropy ($= \ln N$) corresponds to uniform distributions of F_q^e implying non-chaotic behavior and a vanishing μ_q. Conversely, a low eventropy ($= 0$) corresponds to highly ordered distributions in the event space with large fluctuations in F_q^e leading to chaotic dynamics. Thus, a larger μ_q indicates greater chaos in the system.

If the power law behavior of Eq. (5.5) is not satisfied by the experimental data and since the general behaviors of $C_{p,q}(M)$ are rather similar in shape, one can regard $C_{2,2}(M)$ as the reference that carries the typical dependence on M and examine $C_{p,q}(M)$

versus $C_{2,2}(M)$ when M is varied as an implicit variable [9]. If $C_{p,q}(M)$ follows the scaling behavior with $C_{2,2}(M)$ as

$$C_{p,q}(M) \propto C_{2,2}^{\chi(p,q)}(M), \tag{5.7}$$

then the exponent $\chi(p,q)$ measures the erraticity.

Since $\chi(p,q)$ is an increasing function of p with increasing slope, an efficient way to characterize erraticity with one number is simply to use the slope at $p = 1$, i.e.,

$$\chi'_q = \frac{d}{dp}\chi(p,q)|_{p=1}. \tag{5.8}$$

Again, if the moments $C_{p,q}(M)$ do not show scaling behavior with M but have similar non-linear dependence on M, one can consider a generalized form of scaling

$$C_{p,q}(M) \propto g(M)^{\psi'_q(p)}, \tag{5.9}$$

$$\text{where } \ln g(M) = (\ln M)^a, \tag{5.10}$$

and $\psi'_q(p)$ is the newly defined erraticity exponent.

If Eq. (5.9) is approximately valid for a common $g(M)$ for all p and q, it follows from Eq. (5.7) that

$$\chi(p,q) = \psi'_q(p)/\psi'_2(2) \tag{5.11}$$

and the newly defined entropy index

$$\mu'_q = \frac{d}{dp}\psi'_q(p)|_{p=1}. \tag{5.12}$$

Using Eqs. (5.8), (5.11) and (5.12), one can have

$$\mu'_q = \psi'_2(2)\chi'_q. \tag{5.13}$$

These values of μ'_q are distinctly different from $\mu_q$and should not be compared to one another unless $g(M) = M$.

5.5 Erraticity Analysis across Data Sets

We have studied chaotic behavior of produced particles in ^{16}O-AgBr interactions at SPS energy (for experimental data and compared our results with those of IEH events and UrQMD simulated evnets) and in EPOS3 simulated events at LHC energies using the method of erraticity analysis.

5.5.1 Erraticity analysis in experimental data

The method of erraticity analysis described in Section 5.4 is applied to nuclear emulsion data of ^{16}O-AgBr interactions at 60 A GeV in one-dimensional cumulative pseudorapidity (X_η) space. We have divided X_η space of experimental data into M bins, where M is varied from 1 to 10 in steps of 1.

We have calculated the moment of factorial moment $C_{p,q}(M)$ to probe the event-to-event fluctuation of $F_q^e(M)$ using Eq. (5.4). Here p is the order for event-to-event fluctuation and q is the order for spatial fluctuation. For each q value ($2\ and\ 3$) we have calculated the values of $C_{p,q}(M)$ for $p = 2, 3\ and\ 4$. To check whether $C_{p,q}(M)$ follows scaling behavior with M, $\ln C_{p,q}(M)$ is plotted against $\ln M$ for ^{16}O-AgBr collisions in Fig. 5.1. These plots are not linear, so the power law behavior in Eq. (5.5) is not well satisfied. As all $C_{p,q}(M)$ follow similar trend, we consider $C_{2,2}(M)$ as the reference and plot $\ln C_{p,q}(M)$ versus $\ln C_{2,2}(M)$ for $p = 2, 3\ and\ 4$ for each q in Fig. 5.2. Now it is evident that the power law behavior of Eq. (5.7) is well satisfied. The linear best fits of $\ln C_{p,q}(M)$ versus $\ln C_{2,2}(M)$ are performed. The slopes $\chi(p,q)$ of the linear best fits against p values ($2, 3\ and\ 4$) for different q values ($2\ and\ 3$) are plotted in Fig. 5.3. It can be seen from Fig. 5.3 that $\chi(p,q)$ is an increasing function of p with varying slope for both q values. We have to determine the slopes of these plots at $p = 1$. To this end, we first calculate $\ln C_{p,q}(M)$ for $p = 0.9\ and\ 1.1$ for each q value ($2\ and\ 3$) and plot them in Fig. 5.4. These plots show good linear behavior. The values of $\chi(p,q)$ for p = 0.9 and 1.1 for both the q values are listed in Table 5.1. Using Eq. (5.8) we have calculated χ'_q, which are also included in Table 5.1.

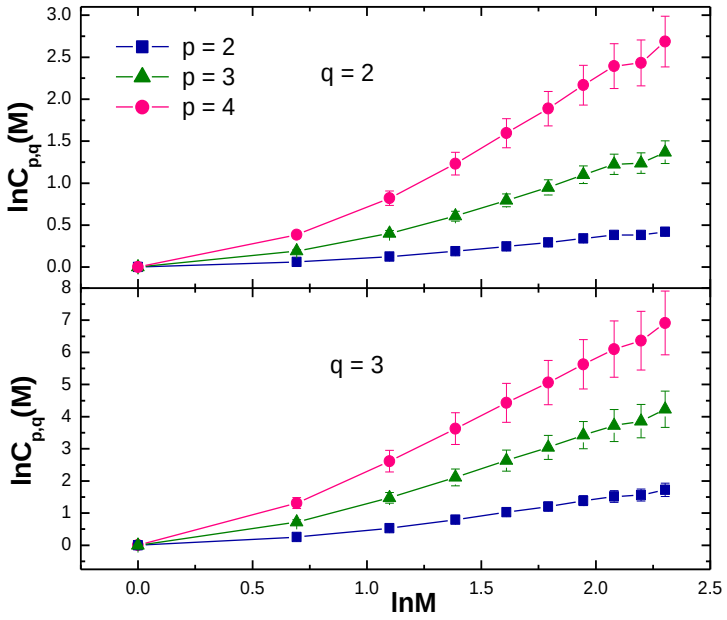

Fig. 5.1: The dependence of $\ln C_{p,q}(M)$ on $\ln M$ (see Eq. (5.5)) for $p = 2, 3$ *and* 4 for $q = 2$ (upper) and 3 (lower) for ^{16}O-AgBr interactions in the pseudorapidity space. The error bars represent statistical errors only.

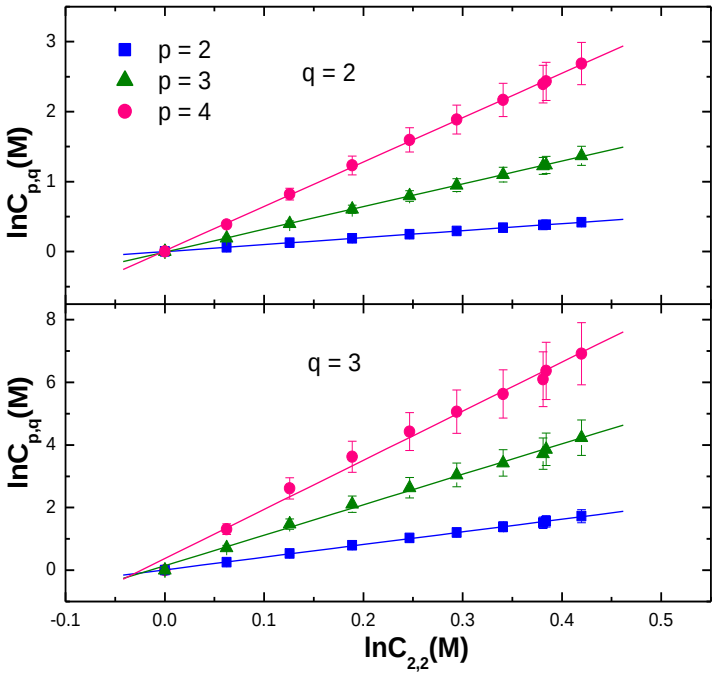

Fig. 5.2: The dependence of $\ln C_{p,q}(M)$ on $\ln C_{2,2}(M)$ (see Eq. (5.7)) for p = 2, 3, 4 for q = 2 (upper), 3 (lower) for ^{16}O-AgBr interactions. Solid lines correspond to linear fits. The error bars represent statistical errors only.

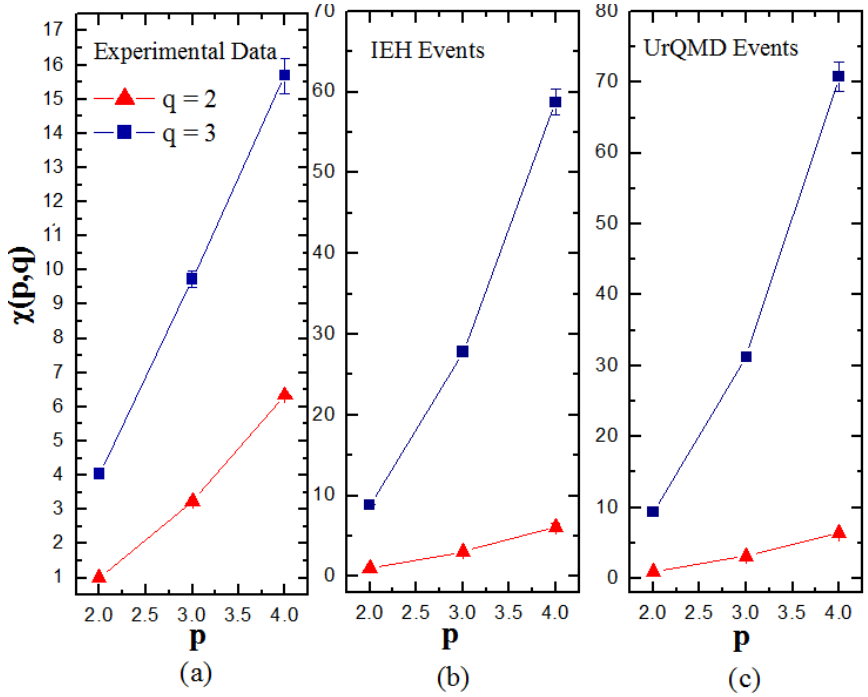

Fig. 5.3: The dependence of $\chi(p,q)$ on p (see Eq. (5.11)) for $q = 2$ and 3 for (a) experimental data (b) IEH events and (c) UrQMD events of ^{16}O-AgBr interactions at 60 A GeV. The error bars represent statistical errors only.

Since $C_{p,q}(M)$ does not show power law behavior with M, as it is also evident from Fig. 5.1 we search for a more general form as in Eq. (5.9). To obtain a good linear behavior of $\ln C_{2,2}(M)$ versus $\ln g(M)$ plot we vary 'a' (see Equation (5.10)). The values of 'a' corresponding to the best-fitted plots of $\ln C_{2,2}(M)$ versus $\ln g(M)$ are tabulated in Table 5.2 and shown in Fig. 5.5 for experimental data of ^{16}O-AgBr interactions at 60 A GeV. The slope of the plot gives $\psi'_2(2)$ value, which is also included in Table 5.2. Using Eqs. (5.8)–(5.13) we quantify the event-to-event fluctuation of factorial moments by calculating the newly defined entropy index μ'_q and tabulate in Table 5.1. The variation of μ'_q against q for ^{16}O-AgBr interactions are shown in Fig. 5.6.

The error bars displayed in the figures are only statistical errors that were computed using the event-wise erraticity moments' standard deviation. The existence of spurious background tracks can cause systematic error in nuclear emulsion detectors, just like it does in other detectors. Some of these tracks may be produced by cosmic radiation during the exposure of the plates, while other tracks may result from the radioactive contamination of the emulsion plates and their glass backings. Most of these background tracks do not originate from an interaction vertex, it can easily be eliminated during the scanning of the emulsion plates under a microscope. In rare

occasion such a track may originate from the interaction vertex and may be measured as an interaction track. However, the interaction vertices' volume is insignificant in relation to the emulsion plate's overall volume. Therefore, there is very little chance that the background tracks and those coming from the interaction vertex will mix together in these respects. Another possible source of systematic error is the electron pairs produced by Dalitz decay or photon-conversion which may also be counted as shower particles. However, a scanner with experienced eye can distinguish them from shower particles since electron pair will be produced not exactly from the interaction vertex. Apart from these background contaminations, systematic error may also be caused by the fading of tracks and variation of shrinkage factor with temperature. However, these errors are also negligible [27].

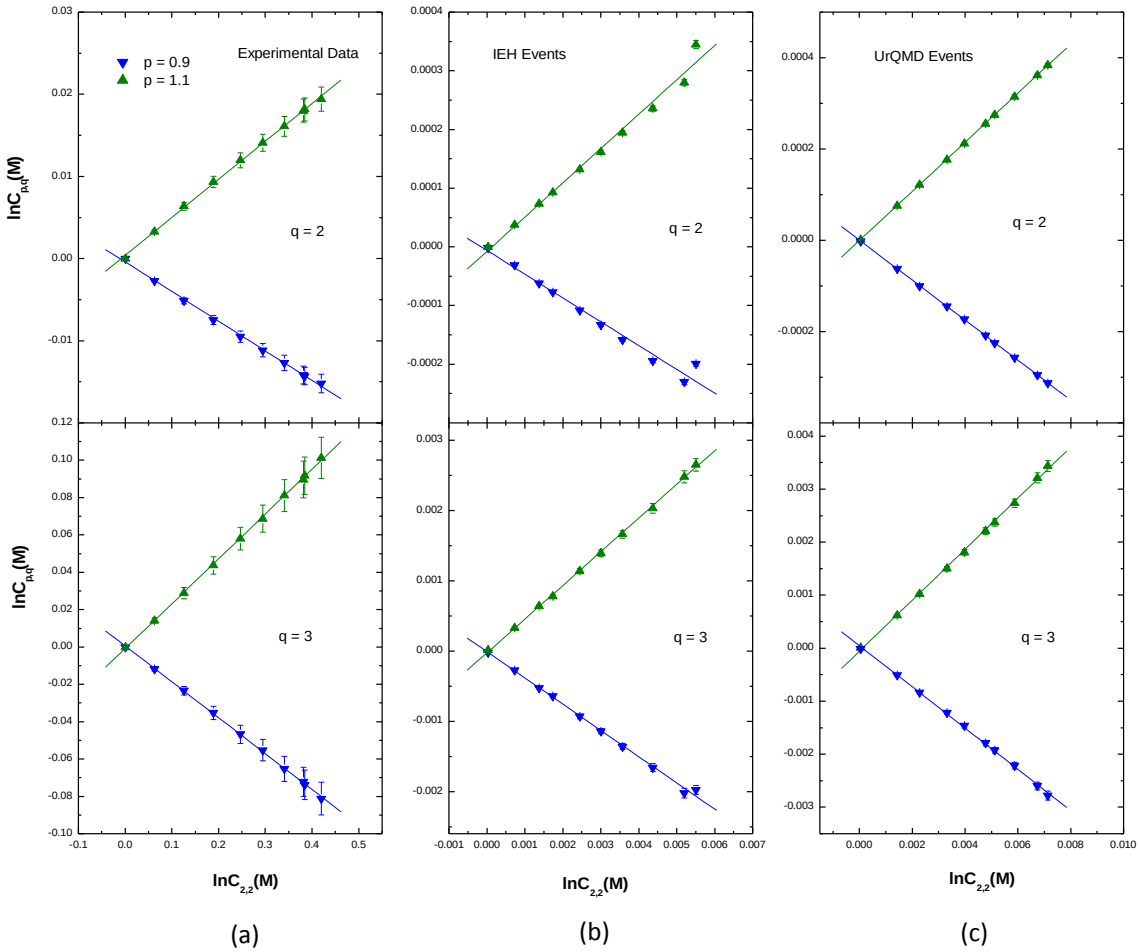

Fig. 5.4: The dependence of $\ln C_{p,q}(M)$ on $\ln C_{2,2}(M)$ for p = 0.9 and 1.1 for q = 2 (upper), 3 (lower) for (a) experimental data (b) IEH events and (c) UrQMD events of ^{16}O-AgBr interactions at 60 A GeV. Solid lines correspond to linear fits. The error bars represent statistical errors only.

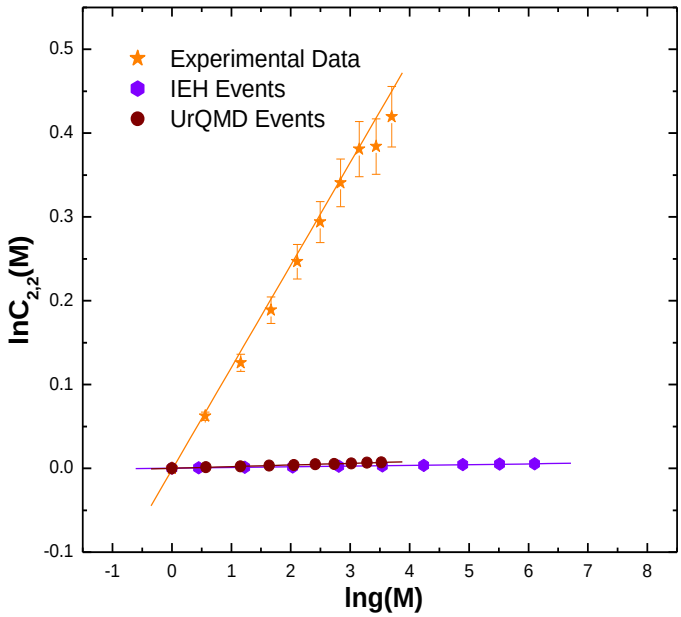

Fig. 5.5: The plots of $\ln C_{2,2}(M)$ versus $\ln g(M)$ for ^{16}O-AgBr interactions. Solid lines correspond to linear fits. The error bars represent statistical errors only.

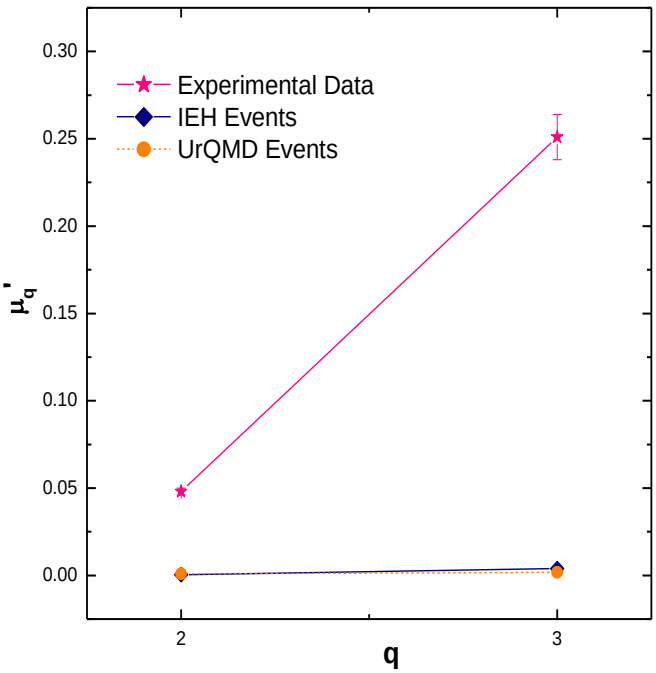

Fig. 5.6: Dependence of μ_q' on q for ^{16}O-AgBr interactions. The error bars represent statistical errors only.

Table 5.1: The values of $\chi(p,q)$ (see Eq. (5.11)), χ'_q (see Eq. (5.8)) and μ'_q (see Eq. (5.12)) for experimental data (values are in bold), IEH events and UrQMD events (values are in parenthesis) for $p = 0.9\ and\ 1.1$ and $q = 2\ and\ 3$ of ^{16}O- AgBr interactions at 60 A GeV. The errors represent statistical errors only.

Event	q	p	$\chi(p,q)$	χ'_q	μ'_q
Experi-mental data	2	0.9	$\mathbf{-0.0360 \pm 0.0005}$	$\mathbf{0.410 \pm 0.004}$	$\mathbf{0.048 \pm 0.002}$
			-0.041 ± 0.002	0.495 ± 0.014	0.00045 ± 0.00005
			(0.04382 ± 0.00008)	(0.4882 ± 0.0001)	(0.00098 ± 0.00002)
		1.1	$\mathbf{0.0460 \pm 0.0005}$		
			0.058 ± 0.002		
			(0.05381 ± 0.00008)		
IEH Events (UrQMD Events)	3	0.9	$\mathbf{-0.1920 \pm 0.0004}$	$\mathbf{2.16 \pm 0.01}$	$\mathbf{0.251 \pm 0.013}$
			-0.374 ± 0.007	4.27 ± 0.04	0.0038 ± 0.0005
			(-0.389 ± 0.005)	(4.355 ± 0.039)	(0.0017 ± 0.0002)
		1.1	$\mathbf{0.240 \pm 0.002}$		
			0.480 ± 0.004		
			(0.482 ± 0.006)		

Table 5.2: Fit parameters (values are in bold for experimental data and values are in parentheses for UrQMD events) corresponding to the plot of Fig. 5.5 for ^{16}O-AgBr interactions. The errors represent statistical errors only.

Events	a	$\psi'_2(2)$
Experimental data	$\mathbf{1.568 \pm 0.067}$	$\mathbf{0.116 \pm 0.006}$
IEH Events	2.169 ± 0.147	0.0009 ± 0.0001
(UrQMD Events)	(1.511 ± 0.074)	(0.00195 ± 0.00005)

5.5.2 Erraticity analysis for IEH events

Monte Carlo events are generated according to the independent emission hypothesis (IEH) to examine whether the observation is non-statistical in nature.

We have performed the whole analyses for the IEH MC events and included the corresponding plots in Figs. 5.3, 5.4, 5.5 and 5.6 and erraticity parameters $\chi(p,q)$, χ'_q, μ'_q, a and $\psi'_2(2)$ values in Table 5.1 and Table 5.2 correspondingly. It is evident from the Fig. 5.6 and Table 5.1 that the values of newly defined entropy index μ'_q for IEH MC events are much less than experimental values, which signifies that our experimental findings are dynamically important.

5.5.3 Erraticity analysis for UrQMD events

To explore the origin of chaos in multiparticle production for experimental data we have compared our results with those of UrQMD generated events.

We have repeated the whole analyses for the UrQMD generated events and included the corresponding plots in Figs. 5.3, 5.4, 5.5 and 5.6 and erraticity parameters $\chi(p,q)$, χ'_q, μ'_q, a and $\psi'_2(2)$ values in Table 5.1 and Table 5.2 correspondingly. It is clear from the Fig. 5.6 and Table 5.1 that similar to the IEH MC events, the values of newly defined entropy index μ'_q for UrQMD generated events are much less than those of experimental values, which shows that UrQMD fails to explain our experimental findings.

5.5.4 Target excitation dependence of erraticity

In nuclear emulsion terminology, grey tracks refer to the tracks made by target recoil protons. These protons are typically the low-energy part of the intranuclear cascade formed during high energy interactions. The number of grey particles is considered as a measure of the violence of target excitation [28]. Thus to study the target excitation dependence of erratic behavior we have divided the whole experimental data set into two sub-samples depending on the number of grey particle (n_g) produced as Sub-sample-I ($0 \leq n_g \leq 4$) and Sub-sample-II ($n_g > 4$). The details of data sets are included in Table 5.3. We have carried out thoroughly the above analyses for both the sub-samples.

The non-linear dependence of $\ln C_{p,q}(M)$ on $\ln M$ for both Sub-sample-I and Sub-sample-II is clear from Fig. 5.7. Hence, similar to the previous analyses we consider $C_{2,2}(M)$ as the reference and plot $\ln C_{p,q}(M)$ versus $\ln C_{2,2}(M)$ in Fig. 5.8 for both the sub-samples. Now we can see that $\ln C_{p,q}(M)$ values are linearly related with $\ln C_{2,2}(M)$ values for both the sub-samples. Data points are fitted using a linear function and also shown in Fig. 5.8. The slopes of the linear best fits, $\chi(p,q)$ are plotted against p (2, 3 and 4) for different q values (2 and 3) in Fig. 5.9. $\chi(p,q)$values increase with p with different slope for both sub-samples. To determine the erraticity measure we plotted $\ln C_{p,q}(M)$ as a function of $\ln C_{2,2}(M)$ for $p = 0.9$ and 1.1 for each q value (2 and 3) for both the sub-samples in Fig. 5.10. The corresponding $\chi(p,q)$ values for p = 0.9 and 1.1 are listed in Table 5.4. Using Eq. (5.8) we have calculated χ'_q, which are also included in Table 5.4. The best linear fits of $\ln C_{2,2}(M)$ versus $\ln g(M)$ have been displayed in Fig. 5.11. The values of 'a' corresponding to the best fitted plots and the slopes of the plots i.e. $\psi'_2(2)$ values are tabulated in Table 5.5. Entropy index μ'_q for both Sub-samples are calculated and included in Table 5.4.

The variation of μ'_q with q for both Sub-sample-I and Sub-sample-II are shown in Fig. 5.12. It is clear from Fig. 5.12 that similar to the whole data set the values of μ'_q increase with q for both sub-samples indicating high chaotic behavior of event-to-event fluctuations with the increase of q for both the sub-samples. The values of μ'_q is higher in case of Sub-sample-I having lower target excitation than those of Sub-sample-II having higher target excitation. It indicates that multiparticle production becomes less chaotic with the increase of target excitation.

Table 5.3: Details of Sub-samples of data for ^{16}O-AgBr interactions at 60 A GeV.

Sub-samples	n_g range	No. of events	Average multiplicity
Sub-sample-I	$0 \leq n_g \leq 4$	125	56.81 ± 2.59
Sub-sample-II	$n_g > 4$	125	69.60 ± 2.65

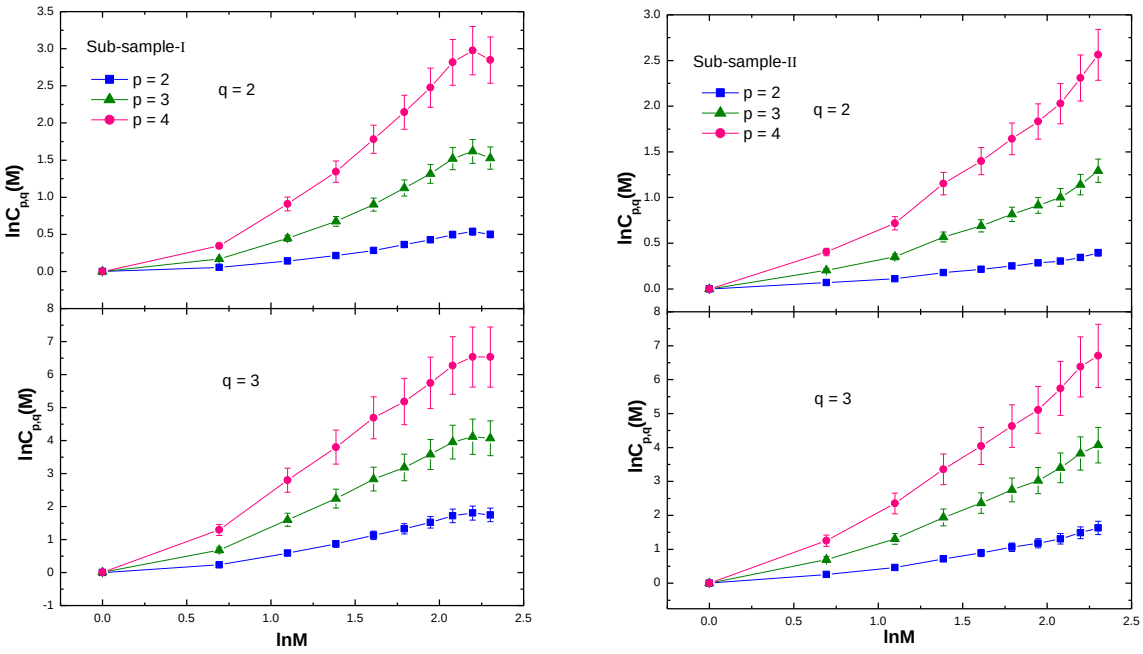

Fig. 5.7: The dependence of $\ln C_{p,q}(M)$ on $\ln M$ for $p = 2, 3$ *and* 4 for $q = 2$ (upper) and 3 (lower) for (left) Sub-sample-I and (right) Sub-sample-II. The error bars represent statistical errors only.

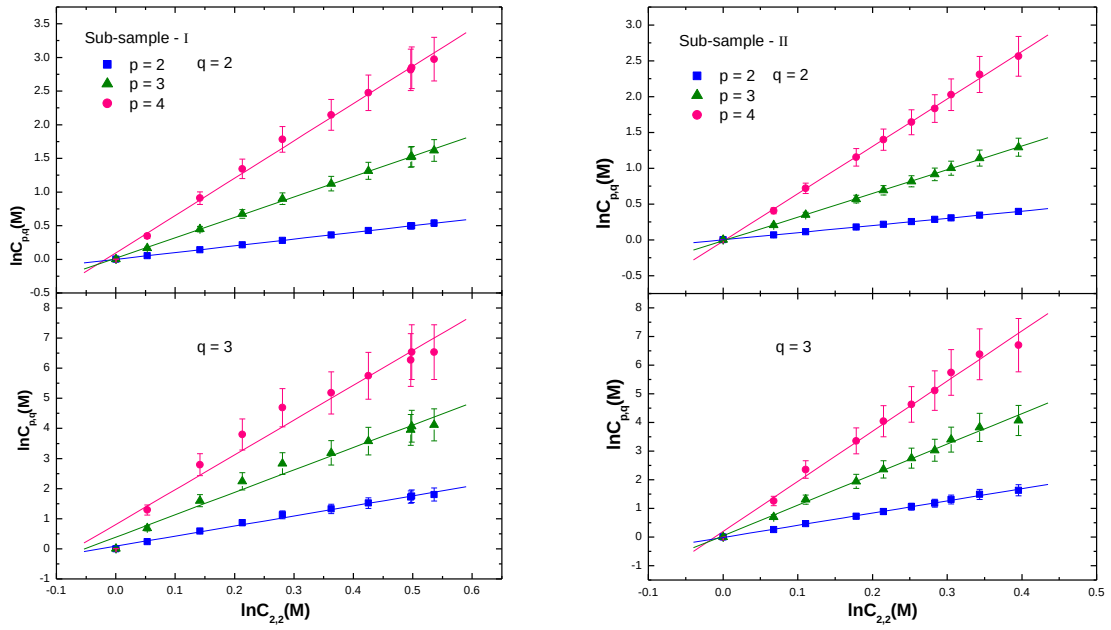

Fig. 5.8: The dependence of $\ln C_{p,q}(M)$ on $\ln C_{2,2}(M)$ for $p = 2, 3$ *and* 4 for $q = 2$ (upper) and 3 (lower) for (left) Sub-sample-I and (right) Sub-sample-II. Solid lines correspond to linear fits. The error bars represent statistical errors only.

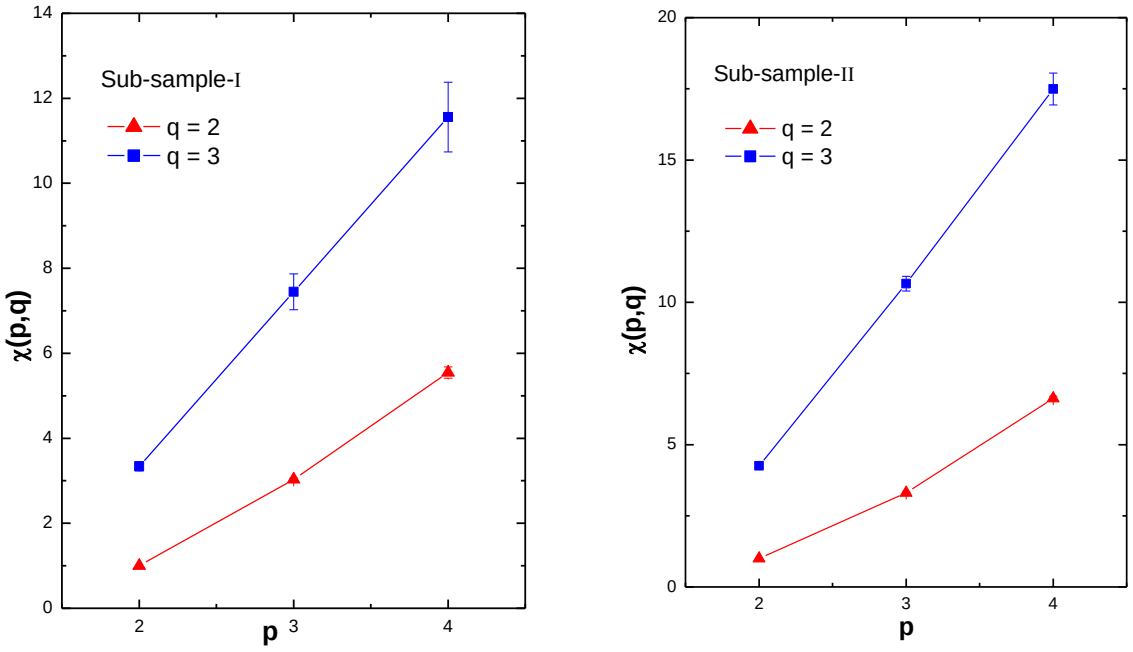

Fig. 5.9: The dependence of $\chi(p,q)$ on p for $q = 2$ and 3 for (left) Sub-sample-I and (right) Sub-sample-II. The error bars represent statistical errors only.

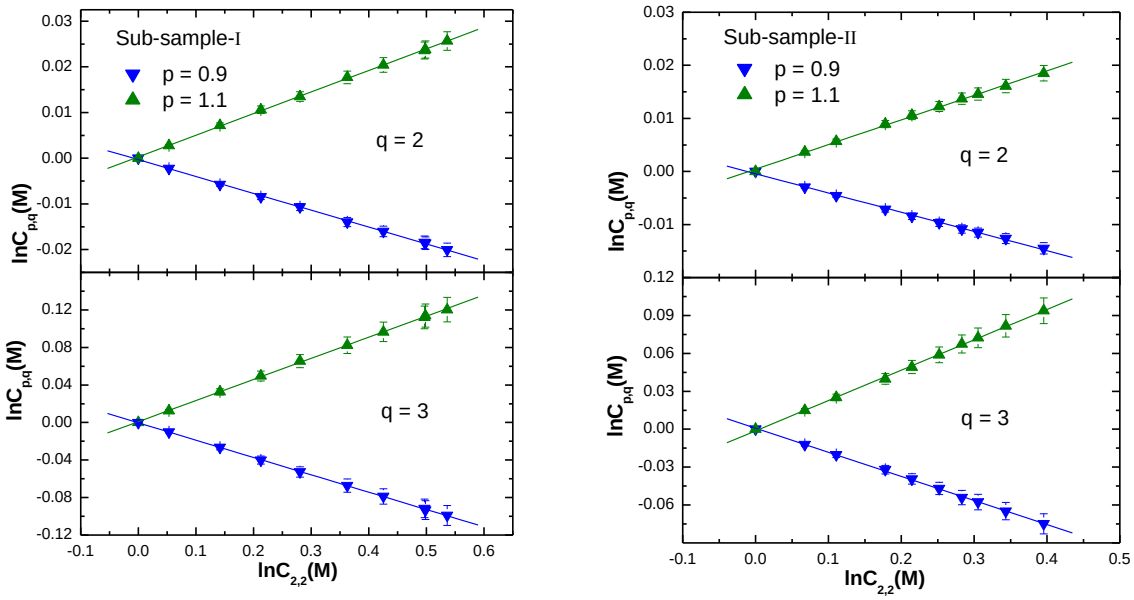

Fig. 5.10: The dependence of $\ln C_{p,q}(M)$ on $\ln C_{2,2}(M)$ for $p = 0.9$ and 1.1 for $q = 2$ (upper) and 3 (lower) for (left) Sub-sample-I and (right) Sub-sample-II. Solid lines correspond to linear fits. The error bars represent statistical errors only.

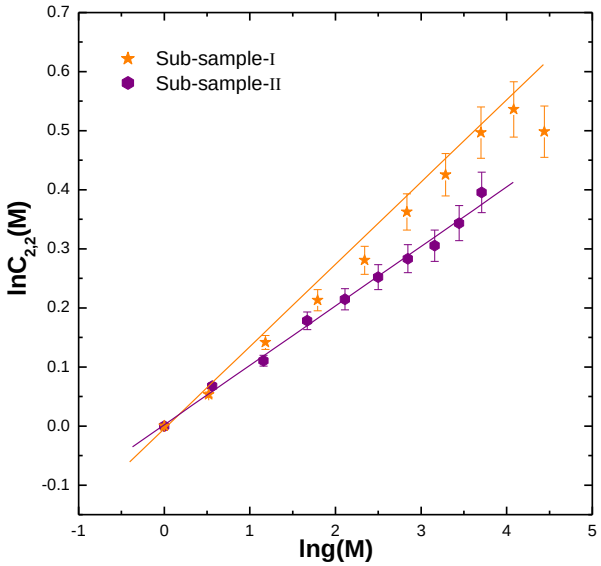

Fig. 5.11: The plots of $\ln C_{2,2}(M)$ versus $\ln g(M)$ for Sub-sample-I and Sub-sample-II. Solid lines correspond to linear fits. The error bars represent statistical errors only.

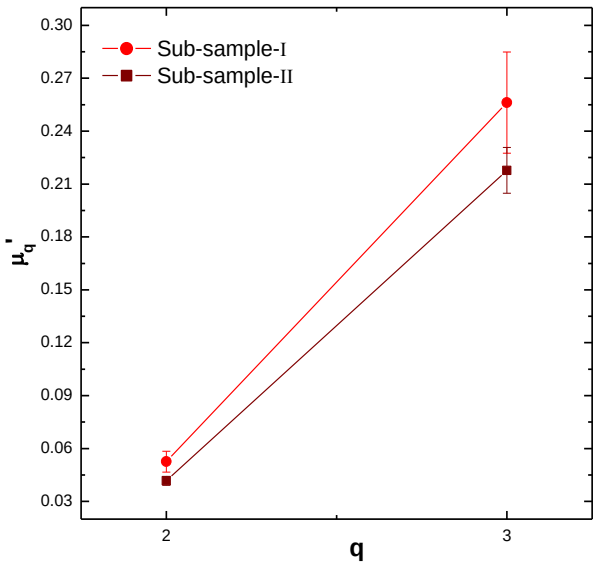

Fig. 5.12: Dependence of μ'_q on q for Sub-sample-I and Sub-sample-II. The error bars represent statistical errors only.

Table 5.4: The values of $\chi(p,q)$ (see Eq. (5.11)), χ'_q (see Eq. (5.8)) and μ'_q (see Eq. (5.12)) for Sub-sample-I and Sub-sample-II for $p = 0.9\ and\ 1.1$ and $q = 2\ and\ 3$ of ^{16}O-AgBr interactions at 60 A GeV. The errors represent statistical errors only.

Event	q	p	$\chi(p,q)$	χ'_q	μ'_q
Sub-sample-I	2	0.9	-0.0369 ± 0.0003	0.421 ± 0.002	0.053 ± 0.006
		1.1	0.0473 ± 0.0003		
	3	0.9	-0.1850 ± 0.0008	2.05 ± 0.006	0.256 ± 0.029
		1.1	0.225 ± 0.001		
Sub-sample-II	2	0.9	-0.0362 ± 0.0006	0.413 ± 0.004	0.042 ± 0.003
		1.1	0.463 ± 0.0006		
	3	0.9	-0.191 ± 0.0002	2.150 ± 0.014	0.217 ± 0.013
		1.1	0.240 ± 0.002		

Table 5.5: Fit parameters corresponding to the plot of Fig. 5.11 for ^{16}O-AgBr interactions. The errors represent statistical errors only.

Events	a	$\psi'_2(2)$
Sub-sample-I	1.79 ± 0.16	0.125 ± 0.014
Sub-sample-II	1.57 ± 0.08	0.101 ± 0.006

5.5.5 Erraticity analysis in EPOS3 simulated events at LHC energies

To probe the scaling behaviors and event-to-event fluctuations of factorial moments more clearly, we have extended our erraticity analysis from SPS energy to the higher energies accessible at the LHC. Specifically, we have revisited and expanded the entire analysis using EPOS3 simulated events for both pp collisions at $\sqrt{s}$ = 13 TeV and pPb collisions at $\sqrt{s_{NN}}$ = 5.02 TeV. This allowed us to systematically examine the dependence of erraticity behavior on both the energy scale and the size of the colliding systems.

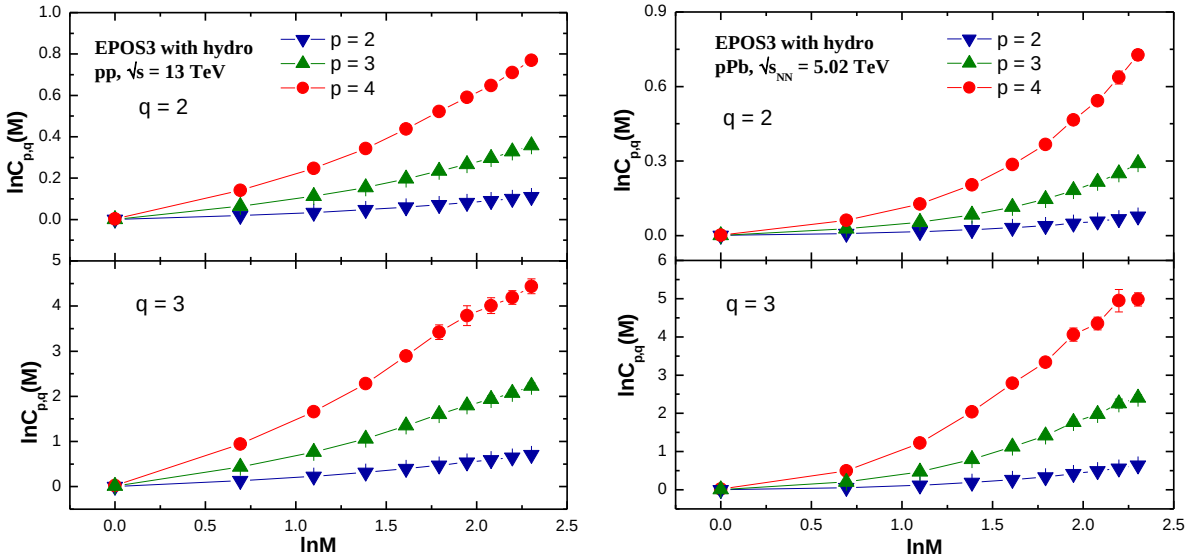

Fig. 5.13: Plot of $\ln C_{p,q}(M)$ versus $\ln M$ for $p = 2, 3$ *and* 4 for $q = 2$ (upper) and 3 (lower), for EPOS3 simulated pp events at $\sqrt{s}$ = 13 TeV (left) and pPb events at $\sqrt{s_{NN}}$ = 5.02 TeV (right). Error bars indicate statistical uncertainties only.

The non-linear dependence of $\ln C_{p,q}(M)$ on $\ln M$ for both pp ($\sqrt{s}$ = 13 TeV) and pPb ($\sqrt{s_{NN}}$ = 5.02 TeV) events is clearly observed in Fig. 5.13. Following the same approach as in the earlier analysis in experimental data, we consider $C_{2,2}(M)$ as the reference and plot $\ln C_{p,q}(M)$ versus $\ln C_{2,2}(M)$ in Fig. 5.14 for both pp and pPb events. It can be seen that $\ln C_{p,q}(M)$ values exhibit a linear relationship with $\ln C_{2,2}(M)$ values for both the systems. Linear fits to the data points are also displayed in Fig. 5.14. The slopes of the linear best fits, $\chi(p,q)$ are plotted as a function p (2, 3 and 4) for different q values (2 and 3) in Fig. 5.15. The $\chi(p,q)$ values show an increasing trend with p for both pp and

pPb events, but with different rates of increase, similar to the behavior observed in previous analysis.

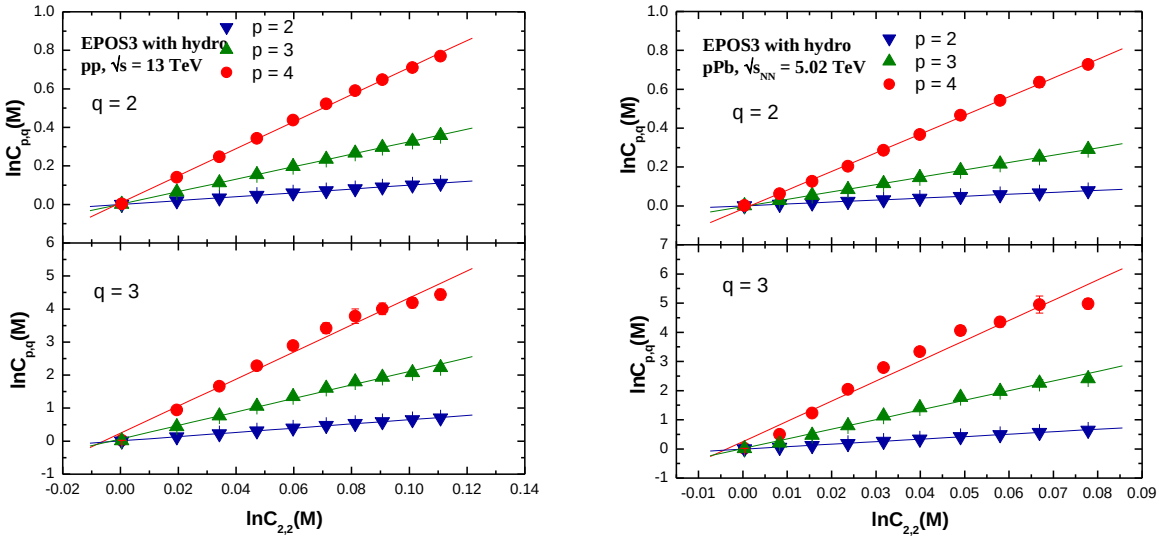

Fig. 5.14: Plot of $\ln C_{p,q}(M)$ versus $\ln C_{2,2}(M)$ for $p = 2, 3\ and\ 4$, for $q = 2$ (upper) and 3 (lower), for EPOS3 simulated pp events at $\sqrt{s}$ = 13 TeV (left) and pPb events at $\sqrt{s_{NN}}$ = 5.02 TeV (right). Solid lines correspond to linear fits. Error bars indicate statistical uncertainties only.

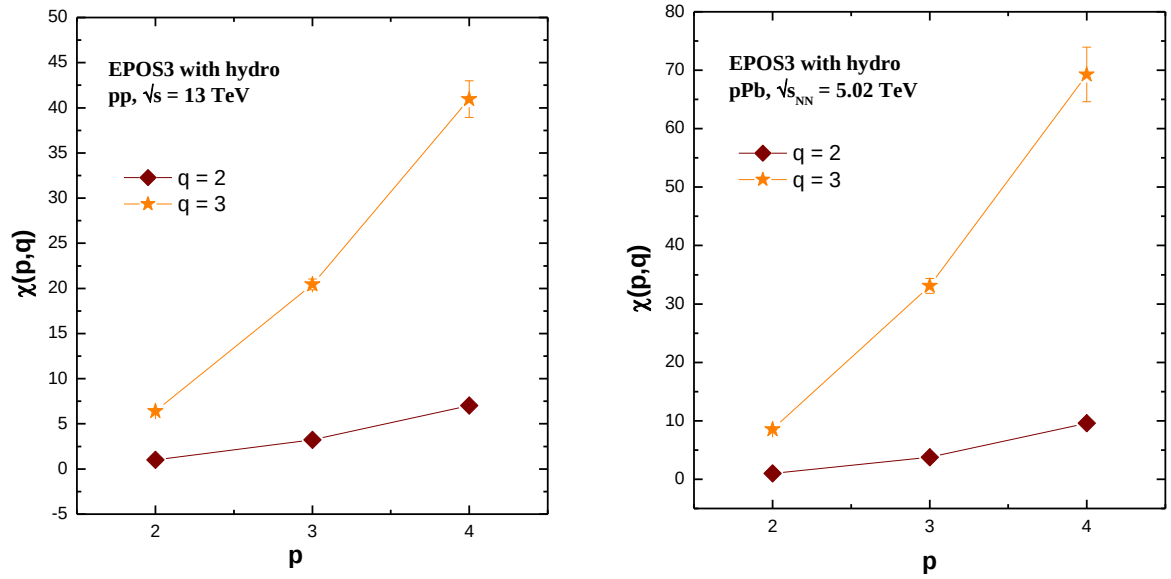

Fig. 5.15: Variation of $\chi(p,q)$ with p for $q = 2$ and 3 for EPOS3 simulated pp events at $\sqrt{s}$ = 13 TeV (left) and pPb events at $\sqrt{s_{NN}}$ = 5.02 TeV (right). Error bars indicate statistical uncertainties only.

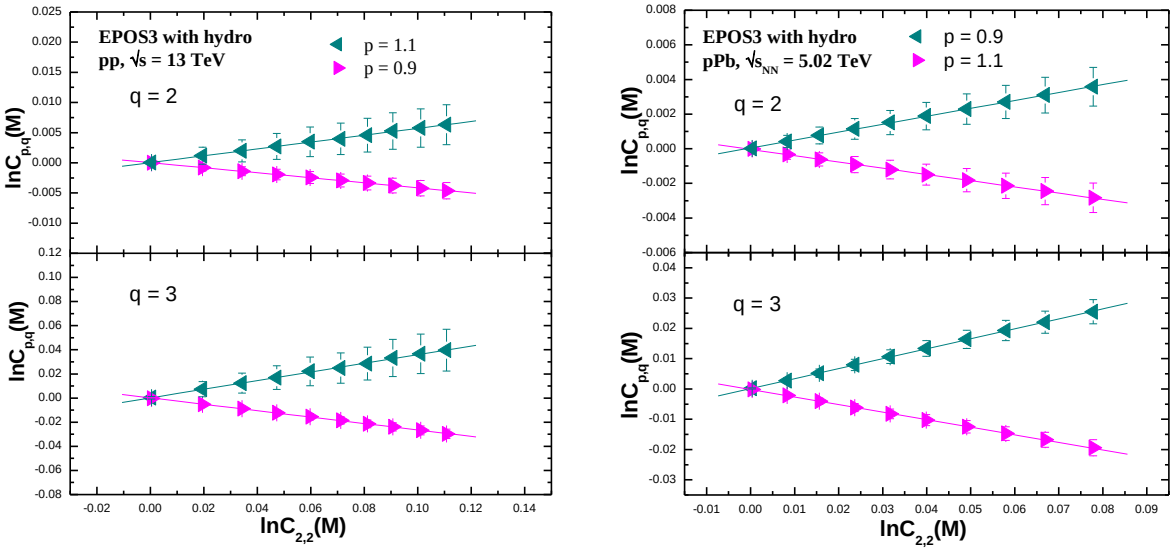

Fig. 5.16: Plot of $\ln C_{p,q}(M)$ versus $\ln C_{2,2}(M)$ for $p = 0.9$ *and* 1.1, for $q = 2$ (upper) and 3 (lower), for EPOS3 simulated pp events at $\sqrt{s}$ = 13 TeV (left) and pPb events at $\sqrt{s_{NN}}$ = 5.02 TeV (right). Solid lines correspond to linear fits. Error bars indicate statistical uncertainties only.

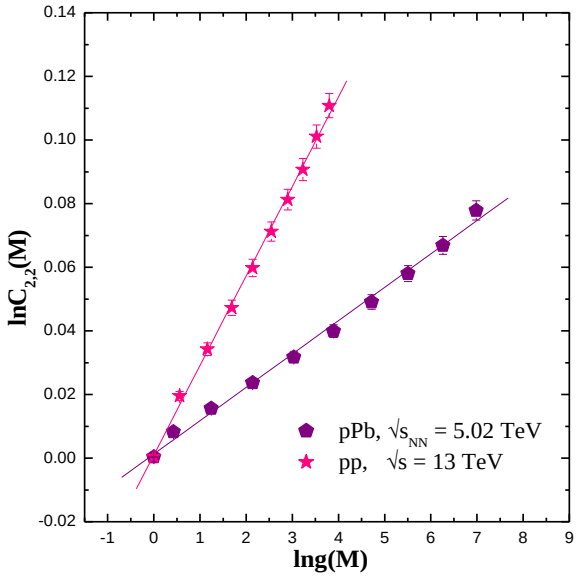

Fig. 5.17: Plots of $\ln C_{2,2}(M)$ against $\ln g(M)$ for EPOS3 simulated pp events at $\sqrt{s}$ = 13 TeV and pPb events at $\sqrt{s_{NN}}$ = 5.02 TeV. Linear fits are shown by solid lines. Error bars represent only statistical uncertainties.

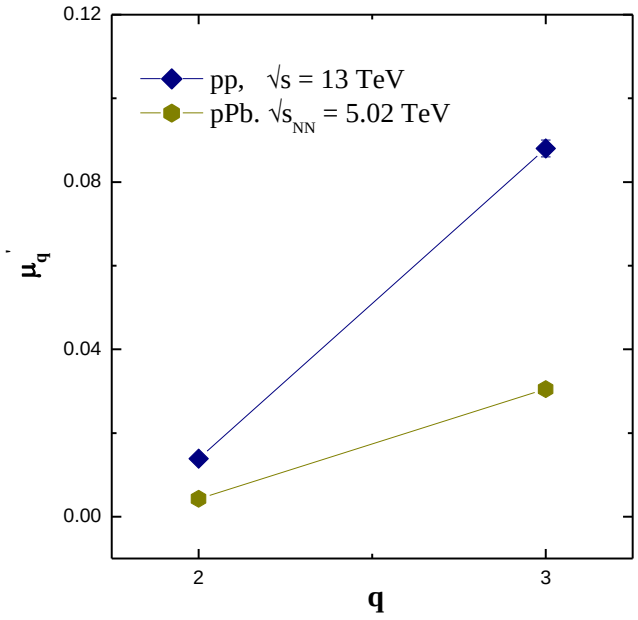

Fig. 5.18: Variation of μ'_q with q for EPOS3 simulated pp events at $\sqrt{s}$ = 13 TeV and pPb events at $\sqrt{s_{NN}}$ = 5.02 TeV. The error bars represent statistical errors only.

In order to determine the erraticity measures, we further plot $\ln C_{p,q}(M)$ versus $\ln C_{2,2}(M)$ for $p = 0.9\ and\ 1.1$ for each q value (2 and 3) for both pp and pPb events, shown in Fig. 5.16. The corresponding values of χ(p,q) and χ'_q are presented in Table 5.6. The best linear fits of $\ln g(M)$ versus $\ln C_{2,2}(M)$ are displayed in Fig. 5.17. The 'a' values obtained from the best-fit plots along with the slopes $\psi'_2(2)$ are listed in Table 5.7. Entropy index μ'_q have been calculated and included in Table 5.6.

The variation of μ'_q with q for both pp and pPb events is shown in Fig. 5.18. It is evident from Fig. 5.18 that μ'_q increases with q for both the systems, indicating that the chaotic nature of event-to-event fluctuations becomes more pronounced with the increase of q. However, within the LHC energy scale, it is found that the values of μ'_q are relatively higher for pp events, while pPb events show comparatively lower μ'_q values. This suggests that pp collisions exhibit relatively stronger chaotic fluctuations compared to pPb collisions within the present analysis framework. It may be due to the fact that pPb collision involves a number of participants in contrast to pp collisions as

well as spectator quarks in pp collisions can take part in particle production but spectator nucleons in pPb collision are unable to participate in particle production.

Table 5.6: The values of $\chi(p,q)$, χ'_q and μ'_q for EPOS3 simulated pp events at $\sqrt{s}$ = 13 TeV and pPb events at $\sqrt{s_{NN}}$ = 5.02 TeV corresponding to $p = 0.9\ and\ 1.1$ and $q = 2\ and\ 3$. The errors reflect statistical uncertainties only.

EPOS3 With hydro Event	q	p	$\chi(p,q)$	χ'_q	μ'_q
pp $\sqrt{s}$ = 13 TeV	2	0.9	-0.0417 ± 0.0002	0.493 ± 0.003	0.0139 ± 0.0002
		1.1	0.0568 ± 0.0006		
	3	0.9	-0.266 ± 0.002	3.12 ± 0.03	0.088 ± 0.002
		1.1	0.358 ± 0.005		
pPb $\sqrt{s_{NN}}$ = 5.02 TeV	2	0.9	-0.0361 ± 0.0003	0.4095 ± 0.0004	0.0043 ± 0.0001
		1.1	0.0458 ± 0.0003		
	3	0.9	-0.250 ± 0.002	2.90 ± 0.01	0.0305 ± 0.0009
		1.1	0.329 ± 0.002		

Table 5.7: Fit parameters corresponding to the plot of Fig. 5.17 for EPOS3 simulated pp events at $\sqrt{s}$ = 13 TeV and pPb events at $\sqrt{s_{NN}}$ = 5.02 TeV. The errors represent statistical errors only.

EPOS3 With hydro Events	a	$\psi'_2(2)$
pp $\sqrt{s}$ = 13 TeV	1.60 ± 0.03	0.0281 ± 0.0004
pPb $\sqrt{s_{NN}}$ = 5.02 TeV	2.3 ± 0.1	0.0105 ± 0.0003

Furthermore, comparing results across energies, we observe from Table 5.1 and Table 5.6 that μ_q' values are smaller at LHC energies than at SPS energies. This indicates a reduction in the chaotic behavior of event-to-event fluctuations at higher collision energies.

5.6 Summary

We have investigated chaotic behavior of produced particles in ^{16}O-AgBr interactions at 60 A GeV using the method of erraticity analysis. The non-zero values of new measure of chaotic behavior indicate chaos in multiparticle production process in ^{16}O-AgBr interactions at 60 A GeV. Our results have been compared with those of IEH events and UrQMD events.

Our major findings are:

- The moment of factorial moment $C_{p,q}(M)$ follows the scaling behavior with $C_{2,2}(M)$ signifying erratic behavior in fluctuation pattern of produced particles. The erraticity measure $\chi(p,q)$, the slopes of the linear best fits of $\ln C_{p,q}(M)$ versus $\ln C_{2,2}(M)$, increases with the order for event-to-event fluctuation.

- The values of erraticity exponent $\psi_2'(2)$, the slopes of the best fitted plots of $\ln C_{2,2}(M)$ versus $\ln g(M)$, are much smaller for both the simulated events than those of experimental data.

- The study reveals chaotic multiparticle production in ^{16}O-AgBr interactions at 60 A GeV as indicated by the values of entropy index μ_q'. The values of entropy indices, μ_q' for experimental data are much greater than those of IEH events, which signify that our observation is dynamically significant. On the other hand, the smaller μ_q' values for UrQMD events compared to experimental values suggest that the UrQMD dynamics is unable to reveal the true fluctuation picture of ^{16}O-AgBr interactions at 60 A GeV.

- The target excitation dependence of chaos has also been investigated by dividing the whole data set into two sub-samples of different target

excitation. Erraticity study on both the sub-samples resembles all the above findings. However, the values of μ_q' is more in case of Sub-sample-I having lower target excitation than those of Sub-sample-II having higher target excitation. It is worth mentioning that multiparticle production process becomes less chaotic with the increase of target excitation.

In addition, erraticity analysis has been performed for EPOS3 simulated pp events at $\sqrt{s}$ = 13 TeV and pPb events at $\sqrt{s_{NN}}$ = 5.02 TeV to investigate the system-size and energy dependence of chaotic behavior. The variation of the erraticity index μ_q' with q shows an increasing trend for both systems, indicating enhanced chaoticity at higher q values. Moreover, the analysis reveals that pp events exhibit relatively stronger chaotic fluctuations compared to pPb events, as indicated by the higher values of the entropy index μ_q'. This suggests that the system size and complexity influence the strength of chaotic behavior in multiparticle production processes. A comparison with results at SPS energies reveals that μ_q' values are smaller at LHC energies, which implies a reduction in the degree of chaoticity with increasing collision energy.

These findings on the system-size and energy dependence chaotic behavior highlight the importance of future experimental studies for better understanding of erratic behavior of even-to-event fluctuations in multiparticle production.

References

[1] P. Bozek, M. Ploszajczak, R. Botet, Phys. Rept. **252**(3), 101–176 (1995).

[2] E. A. De Wolf, I. M. Dremin, W. Kittel, Phys. Rept. **270**(3), 1–141 (1996).

[3] M. I. Adamovich *et al.*, J. Phys. G **19**(12), 2035 (1993).

[4] I. M. Dremin *et al.*, JETP Lett. **30**, 140-144 (1979).

[5] I. M. Dremin *et al.*, Sov. J. Part. Nucl. **18**, 31 (1987).

[6] A. Bialas, R. Peschanski, Nucl. Phys. B **273**(3–4), 703–718 (1986).

[7] Z. Cao, R. C. Hwa, Phys. Rev. Lett. **75**(7), 1268 (1995).

[8] Z. Cao, R. C. Hwa, Phys. Rev. D **53**(11), 6608-6618 (1996).

[9] Z. Cao, R. C. Hwa, Phys. Rev. D **61**, 074011 (2000).

[10] Z. Cao, R. C. Hwa, Phys. Rev. E **56**(1), 326–333 (1997).

[11] W. Shaoshun *et al.*, Phys. Lett. B **416**(1–2), 216–219 (1998).

[12] W. Shaoshun, W. Zhaomin, Phys. Rev. D **57**(5), 3036–3039 (1998).

[13] S. Wang, C. Wu, Z. Wang, Phys. Lett. B **458**(4), 505–510 (1999).

[14] D. Ghosh, A. Deb, M. Mondal, J. Ghosh, Phys. Rev. C **68**(2), 024908 (2003).

[15] D. Ghosh, A. Deb, M. Mondal, K. K. Patra, J. Ghosh, J. Phys. G: Nucl. Part. Phys. **31**(9), 1083 (2005).

[16] D. Ghosh, A. Deb, M. Mondal, *et al.*, J. Phys. G: Nucl. Part. Phys. **35**(12), 125005 (2008).

[17] D. Chanda, M. K. Ghosh *et al.*, Phys. Rev. C **71**(3), 034904 (2005).

[18] S. Ahmad, M. M. Khan, N. Ahmad, A. Ahmad, J. Phys. G: Nucl. Part. Phys. **30**(9), 1145 (2004).

[19] R. C. Hwa, Y. Wu, Phys. Rev. C **60**(5), 054904 (1999).

[20] R. C. Hwa, Nonlinear Phenom. Complex Syst. **3**(1), 93-98 (2000).

[21] D. Ghosh, A. Deb, S. R. Sahoo, P. K. Haldar, Md. A. K. Jafry, Nucl. Phys. A **707**(1–2), 213–223 (2002).

[22] A. Ariga, T. Ariga, G. De Lellis, A. Ereditato, K. Niwa. Nuclear Emulsions. In: C. W. Fabjan, H. Schopper (eds.), Particle Physics Reference Library. Volume 2: Detectors for Particles and Radiation, Springer International Publishing, Cham, 383-438 (2020). https://doi.org/10.1007/978-3-030-35318-6_9

[23] M. Bleicher *et al.*, J. Phys. G: Nucl. Part. Phys. **25**(9), 1859–1896 (1999).

[24] K. Werner, B. Guiot, Iu. Karpenko and T. Pierog, Phys. Rev. C **89**, 064903 (2014).

[25] W. Ochs, Z. Phys. C: Particles and Fields **50**, 339–344 (1991).

[26] R. C. Hwa, Acta Phys. Pol. B **27**, 1789 (1996).

[27] G. Bhoumik, S. Bhattacharyya, A. Deb, and D. Ghosh, Eur. Phys. J. A **52**, 196 (2016).

[28] J. Babecki and G. Nowak, Acta Phys. Pol. B **9**(5), 401–417 (1978).

Chapter 6

Concluding Remarks

Conclusion

This thesis presents a comprehensive investigation into the complex dynamics of multiparticle production in high energy hadronic and heavy-ion collisions through the lens of correlation and fluctuation observables. A series of detailed studies using both experimental data and simulated events based on two different Monte Carlo models have been performed. The main objective was to understand the underlying mechanisms governing particle production by studying fluctuations and correlations and the impact of event characteristics such as centrality, multiplicity, system size and collision energy on these phenomena. The results obtained from this work significantly contribute to the ongoing discussion in high energy nuclear physics and open new avenues for deeper exploration of QCD phenomena in extreme conditions.

The study of forward-backward multiplicity and momentum correlations in EPOS3 simulated pp and pPb collisions at LHC energies enhances our understanding of both long-range and short-range correlations among the produced particles. By varying the separation between FB windows, window width and transverse momentum thresholds, the analysis revealed how the correlation strength evolves with these parameters, reflecting the influence of short-range and long-range components in the observed FB correlation. It is indeed interesting to observe that the $\delta\eta$-weighted average of both FB correlation strengths increase with center-of-mass energy up to 7 TeV and then tend to saturate at very high energies. This saturation phenomenon at high energies is exhibited by particles originating from the core component in the EPOS3 model. This could indicate the dominance of the gluon-saturation effect or other collective phenomena in the high energy regime. Moreover, the behavior of the strongly intensive observable $\Sigma(N_f, N_b)$ was analyzed, which is insensitive to multiplicity bin width, and a strong dependence of $\Sigma(N_f, N_b)$ on η-separation was also observed. Thus, this variable proved valuable in probing the intrinsic dynamical fluctuations of the system independent of volume effects.

The fractal analysis using the Visibility Graph technique revealed scale-invariant features in multiparticle production across both experimental and simulated data. A clear centrality-dependent trend in fractality was observed in pion distributions of ^{16}O-AgBr interactions at 60 A GeV, with the Power of Scale-freeness decreasing toward

more central events. The mean values of average clustering coefficient computed from the visibility graphs reflect that the dynamics of particle production is different for different centrality event-samples. Additionally, the Hurst exponent analysis reveals that the origin of event-by-event fluctuations differs with centrality, with lower-centrality events governed by persistent behavior and fractional Gaussian noise (fGn) and higher-centrality events exhibiting anti-persistent behavior and is characterized by fractional Brownian motion (fBm). These findings collectively point to the presence of distinct dynamical regimes in pion production at different collision centralities. Event-by-event VG analysis of EPOS3 simulated pp collisions at $\sqrt{s}$ = 7 TeV further demonstrates that fluctuations in charged particle production exhibit a fractal nature. Moreover, the transverse momentum dependence of this fractality suggests that particle production becomes increasingly complex as the system evolves from soft to hard processes.

The study of chaotic behavior in multiparticle production through erraticity analysis of ^{16}O-AgBr interactions at 60 A GeV revealed additional layers of complexity in the observed fluctuations. The non-zero values of entropy indices and scaling exponents confirmed the presence of chaos in multiparticle production. Comparisons with the UrQMD model revealed that it failed to capture the true nature of fluctuation patterns present in the data. A significant dependence on target excitation was also observed, with lower-excitation events exhibiting greater chaoticity, reflecting that chaotic behavior is suppressed as target excitation increases. EPOS3 simulated pp and pPb events also displayed chaotic patterns, with pp events exhibiting stronger chaoticity than pPb events. This indicates that system size and complexity influence the strength of chaotic behavior in multiparticle production processes. Interestingly, a reduction in the degree of chaoticity in multiparticle production is observed at higher (LHC) energies compared to SPS energies.

Thus, this thesis advances our understanding of multiparticle production by revealing the interplay of soft and hard processes, the emergence of collective behavior in small systems and the signatures of chaos and fractality in hadron-hadron, hadron-nucleus and nucleus-nucleus collisions at SPS and LHC energies.

Future Directions

By far, this study has focused on forward-backward correlations along the longitudinal direction, specifically in pseudorapidity (η). While this provides important insights into the longitudinal dynamics, a more comprehensive understanding of the origins of these correlations can be achieved by extending the analysis to include the azimuthal angle (φ). Studying correlations in both η and φ would allow for the investigation of azimuthal anisotropies and possible connections to collective flow phenomena, as well as the disentanglement of short-range and long-range correlation sources.

Additionally, this work has primarily concentrated on a particular FB correlation variable, b_{corr}, which serves as a quantitative measure of the correlation strength. Some preliminary investigations have also been carried out using an intensive variable, Σ. Since b_{corr} is extensive in nature, it is inherently sensitive to the overall particle multiplicity in an event. To address this, future studies could incorporate event-mixing techniques to help disentangle non-dynamical correlations arising from trivial multiplicity fluctuations. Such methods would reduce the dependence on multiplicity and enable more reliable comparisons across different collision systems and beam energies.

Furthermore, the variable Σ, being intensive, offers a promising alternative that is less affected by multiplicity fluctuations. It would be beneficial to explore the full potential of Σ by performing multi-differential analyses in rapidity, azimuthal angle, and transverse momentum, spanning a wide range of collision energies. This approach could provide deeper insights into the nature and origins of forward-backward correlations and their connection to the underlying dynamics of the collision system.

Annexure 1

Front pages of published papers

Chaos, Solitons and Fractals 113 (2018) 230–237

Contents lists available at ScienceDirect

Chaos, Solitons and Fractals

Nonlinear Science, and Nonequilibrium and Complex Phenomena

journal homepage: www.elsevier.com/locate/chaos

Evidence of centrality dependent fractal behavior in high energy heavy ion interactions: Hint of two different sources

Mitali Mondal[a,*], Arindam Mondal[b], Joyati Mondal[a], Kanchan Kumar Patra[b], Argha Deb[a], Dipak Ghosh[a]

[a] Nuclear and Particle Physics Research Centre, Department of Physics, Jadavpur University, Kolkata – 700032, India
[b] RCC Institute of Information Technology, Beliaghata, Kolkata – 700015, India

ARTICLE INFO

Article history:
Received 23 February 2018
Revised 6 June 2018
Accepted 8 June 2018
Available online 23 June 2018

Keywords:
High energy nucleus-nucleus collision
Event-by-event fluctuation
Fractal behaviour
Clustering property
Centrality dependence
Visibility graph analysis

ABSTRACT

Studies on large density fluctuations in produced particle spectra in high energy interactions provide enough information regarding the dynamics of the process of particle production. Various analyses have revealed self-similarity in particle production process. The concept of self-similarity is indicative of fractal geometry. The present analysis reports an exhaustive study on centrality dependence of event-by-event fluctuation of pions produced in ^{16}O-AgBr interactions at 60 A GeV using a non conventional tool based on complex network analysis, viz. visibility graph method. The analysis reveals different fractal behaviour as well as different clustering property for different centrality events and the amount of fractality and average clustering coefficient decrease with the increase of centrality. Estimation of Hurst exponent hints towards two different sources of fluctuation, fractional Brownian motion (fBm) and fractional Gaussian noises (fGn) for two different centrality classes.

© 2018 Elsevier Ltd. All rights reserved.

1. Introduction

Complex network and time series are two generic ways to describe complex systems. Dynamical properties of time series can usually be preserved in network topological structures. Lots of methods have been developed to capture the geometrical structure of time series from complex network aspect such as cycle network [1], correlation network [2], visibility graph [3], recurrence network [4] and isometric network [5] as well as to monitor evolutionary behaviors of complex systems stored in different time series [6-9].

Visibility graph maps a time series into a network. This network inherits several properties of the time series, and the study of the network reveals nontrivial information about the series itself. It has been reported that the periodic time series can be transformed into regular graphs and random series corresponding to random graphs [10] and fractal series into scale-free graphs [3,11-14].

The visibility graph method has a wide range of applicability. It has been applied in searching for the hidden geometry of traffic jamming [15], in studying energy dissipation rates in three-dimensional fully developed turbulence [16], in analyzing exchange rate series [17], in searching for fluctuation and geometrical structure of magnetisation time series of two-dimensional Ising model around critical point [18], in investigating human heartbeat dynamics [19-21], in searching for multifractal nature of multiparticle production in high energy collisions [22-27].

Over the last few decades, the physics of high energy collisions has been in the frontier of the Basic Science research activities throughout the world. According to the acceptable theory, the tiny Universe of high energy-density and temperature, immediately after the Big Bang, evolved through a state of an exotic phase of partonic (comprises of quarks and gluons - the elementary particles) matter, called the Quark-Gluon Plasma (QGP) [28], that survived for some microseconds only. It was predicted that QGP - the plasma state in quantum chromodynamics (QCD) can be created also in the laboratory [29].

However, since the QGP phase is very short lived, it is not possible to detect its direct signal. Physicists have to depend on indirect signals. Existence of large dynamical fluctuation in produced particle spectra is one of the signals of QGP.

To search for the dynamical fluctuation Bialas and Peschanski [30,31] coined a method named intermittency, which refers to the power-law behaviour of factorial moments with respect to the size of phase-space interval in the process of multipion production in heavy-ion interaction. This indicates self-similar fluctuation in this process and self-similarity indicates fractal behaviour. From this analysis, a conjecture has been raised that multipion production process might show fractal behaviour and also there might be a relationship between intermittency and fractality. Multipion produc-

* Corresponding author.
E-mail address: mitalimon@gmail.com (M. Mondal).

https://doi.org/10.1016/j.chaos.2018.06.006
0960-0779/© 2018 Elsevier Ltd. All rights reserved.

Forward-backward multiplicity and momentum correlations in *pp* collisions at LHC energies

Mitali Mondal,[1,2,*] Joyati Mondal,[1] Somnath Kar,[1] Argha Deb,[1,2] and Premomoy Ghosh[3]

[1]*Nuclear and Particle Physics Research Centre, Department of Physics, Jadavpur University, Kolkata 700032, India*

[2]*School of Studies in Environmental Radiation and Archaeological Sciences, Jadavpur University, Kolkata 700032, India*

[3]*Variable Energy Cyclotron Centre, HBNI, 1/AF Bidhan Nagar, Kolkata 700064, India*

(Received 7 June 2020; accepted 1 July 2020; published 21 July 2020)

Charged-particle multiplicity and summed values of the transverse momentum (p_T) have been utilized for estimating forward-backward (FB) correlation strength for EPOS3 simulated proton-proton (pp) events with and without hydrodynamical evolution of particles at center-of-mass energies $\sqrt{s} = 0.9$, 2.76, and 7 TeV for different pseudorapidity window width ($\delta\eta$) and gap between the FB windows (η_{gap}). We have studied the variation of FB correlation strength with η_{gap}, $\delta\eta$, $\sqrt{s}$, different p_T cuts, and multiplicity classes. Results are compared with the corresponding ALICE and ATLAS data. EPOS3 model qualitatively reproduces the overall variation of correlation strength of the LHC data. However, quantitative agreement is better for pp events, generated using EPOS3 with hydrodynamical evolution of particles, with ATLAS data.

DOI: 10.1103/PhysRevD.102.014033

I. INTRODUCTION

In ultrarelativistic high-energy collisions, the study of correlations between produced particles in different pseudorapidity (η) regions gives us an opportunity to understand the dynamics of multiparticle interactions and their hadronization. In general, these correlations are of two types: short-range correlations (SRCs) and long-range correlations (LRCs) [1–4]. Particles with lower transverse momentum (p_T) are generated via soft processes [5] and are believed to be correlated weakly over large η range (LRC). The particles in the high-p_T regime, which are produced via harder perturbative processes, are strongly correlated over short pseudorapidity distances (SRC) [6]. With the gradual increase of particle momentum from soft regime to hard, the correlations strength is found to be weakened over large η separations [7,8]. In different experiments and theoretical models, short-range correlations are considered to be localized over $|\eta| \sim 1$ units of pseudorapidity whereas long-range correlations extend over a wider range of pseudorapidity ($|\eta| > 1$) [9].

Forward-backward (FB) correlation, a robust tool to explore both the SRC and the LRC, plays important role in understanding initial state fluctuations in different collision systems like hadronic or nuclear. Pairs of pseudorapidity intervals equal in size and symmetrically located in the forward (beam direction) and backward (opposite to the beam direction) direction with respect to the collision vertex are considered as forward and backward windows, respectively. Event-by-event variations of different observables in FB windows can be used to construct FB correlation coefficients [3,6,10].

Several experimental studies on FB correlations had been previously carried out for different collision systems including electron-positron (e^+e^-), proton-proton (pp), proton-antiproton ($p\bar{p}$), proton-nucleus (pA), and nucleus-nucleus (AA) [1–3,7,11–19]. Though, there was no FB multiplicity correlation found in e^+e^- annihilation [13], but in hadronic collisions ($pp/p\bar{p}$) or in heavy-ion collisions with higher energies at the Super Proton Synchrotron [1–3], the Tevatron [15], the Relativistic Heavy Ion Collider (RHIC) [16,17], and the Large Hadron Collider (LHC) [7,18,19], a considerable correlation strength was observed. All these experimental observations offer a cornucopia of scopes to testify various theoretical and/or phenomenological models for a possible explanation of the FB correlation exploiting different correlation coefficients between the multiplicities ($n - n$), the transverse momentums ($p_T - p_T$), and the transverse momentum and the multiplicity of charged particles ($p_T - n$).

*mitalimon@gmail.com

Published by the American Physical Society under the terms of the Creative Commons Attribution 4.0 International license. Further distribution of this work must maintain attribution to the author(s) and the published article's title, journal citation, and DOI. Funded by SCOAP[3].

Forward-backward multiplicity and momentum correlations in *pp* and *p*Pb collisions at the LHC energies

Joyati Mondal,[1,*] Hirak Koley,[1] Somnath Kar,[2,1,†] Premomoy Ghosh,[1] Argha Deb,[1,3] and Mitali Mondal[1,3,‡]

[1]*Department of Physics, Nuclear and Particle Physics Research Centre, Jadavpur University, Kolkata—700032, India*

[2]*University Department of Physics, Kolhan University, Chaibasa—833201, India*

[3]*School of Studies in Environmental Radiation and Archaeological Sciences, Jadavpur University, Kolkata—700032, India*

(Received 6 January 2023; accepted 11 May 2023; published 13 June 2023)

Correlations and fluctuations between produced particles in an ultrarelativistic nuclear collisions remain one of the key observables to understand the fundamentals of the particle production mechanism. More differential tools like forward-backward (FB) correlations between particles from two different phase spaces further strengthened our understanding. We study the strength of FB correlations in terms of charged-particle multiplicity and summed transverse momentum for proton-proton (pp) and proton-lead (pPb) collisions at center-of-mass energies $\sqrt{s} = 13$ TeV and $\sqrt{s_{\rm NN}} = 5.02$ TeV, respectively, for the EPOS3 simulated events with hydrodynamical evolution of produced particles. Furthermore, the correlation strengths are separately obtained for the particles coming from the core and the corona. FB correlation strengths are examined as a function of the pseudorapidity gap ($\eta_{\rm gap}$), pseudorapidity window width ($\delta\eta$), center-of-mass energy ($\sqrt{s}$), minimum transverse momentum ($p_{T_{\rm min}}$), and different multiplicity classes following standard kinematical cuts used by the ALICE and ATLAS experiments at the LHC for all three EPOS3 event samples. The EPOS3 model shows a similar trend of FB multiplicity and momentum correlation strengths for both pp and pPb systems, though the correlation strengths are found to be larger for the pPb system than for the pp system. Moreover, the $\delta\eta$-weighted average of FB correlation strengths as a function of different center-of-mass energies for pp collisions delineates a tendency of saturation at very high energies.

DOI: 10.1103/PhysRevD.107.114016

I. INTRODUCTION

The formation of a hot dense medium of quasifree quarks and gluons, known as the quark-gluon plasma (QGP), in relativistic heavy-ion collisions at the Relativistic Heavy Ion Collider (RHIC) and the Large Hadron Collider (LHC) provides a unique opportunity to explore the early Universe and validate the theory of strong interactions between quarks mediated by gluons [1–3]. The relativistic viscous hydrodynamic calculations [4,5] have been found to be most successful in explaining the properties of the produced hot and dense matter in heavy-ion collisions and demonstrate the space-time evolution of the medium through observables such as harmonic flow (v_n) [6–8], which represent the translation of initial-state spatial inhomogeneities to the final-state momentum anisotropies.

In heavy-ion collisions, the initial energy density fluctuates strongly event to event which leads to the fluctuations of the space-time evolution of the produced medium in the final state. Owing to the viscous hydrodynamics, such density fluctuations are manifested as anisotropic harmonic flow. The large initial-state fluctuations effectuate the observed long-range correlations (LRCs) between final-state particles which are observed as a correlation between multiplicity densities in different pseudorapidity (η)-windows [9]. Another aspect of longitudinal multiplicity correlations is the short-range correlations (SRCs) localized over a smaller range of η, manifested in the single jet, minijets, resonance decays, etc. Forward-backward (FB) correlations between charged-particle multiplicities or transverse momenta in two symmetrically separated η-windows about the collision vertex motivate us to differentiate between LRC and SRC components [10] and to study the dynamics of the particle production mechanism in high-energy hadron or nuclear collisions.

Positive FB multiplicity correlation strength was first observed in $p\bar{p}$ collisions at $\sqrt{s} = 540$ GeV at the CERN

*joyati254@gmail.com
†somnathkar11@gmail.com
‡mitalimon@gmail.com

Published by the American Physical Society under the terms of the Creative Commons Attribution 4.0 International license. Further distribution of this work must maintain attribution to the author(s) and the published article's title, journal citation, and DOI. Funded by SCOAP[3].

Eur. Phys. J. Plus (2024) 139:960
https://doi.org/10.1140/epjp/s13360-024-05753-4

THE EUROPEAN PHYSICAL JOURNAL PLUS

Regular Article

Chaos in multiparticle production in ^{16}O–AgBr interactions at 60 A GeV and its target excitation dependence

Joyati Mondal[1], **Hirak Kumar Koley**[1], **Jessica Ghatak**[1], **Argha Deb**[1,2], **Mitali Mondal**[1,2,a]

[1] Nuclear and Particle Physics Research Centre, Department of Physics, Jadavpur University, Kolkata 700032, India
[2] School of Studies in Environmental Radiation and Archaeological Sciences, Jadavpur University, Kolkata 700032, India

Received: 24 July 2024 / Accepted: 16 October 2024
© The Author(s), under exclusive licence to Società Italiana di Fisica and Springer-Verlag GmbH Germany, part of Springer Nature 2024

Abstract We study the chaotic behavior of produced particles in ^{16}O–AgBr interactions at 60 A GeV using the method of erraticity analysis. The non-zero values of new measure of chaotic behavior indicate chaos in multiparticle production process in ^{16}O–AgBr interactions at 60 A GeV. The dynamical origin of such behavior is indicated by the comparison of the present result with the results of Monte-Carlo event generator, based on independent emission hypothesis. Furthermore, UrQMD event generator is unable to reproduce the true chaotic nature of multiparticle production in the same interaction. The target excitation dependence of chaos have also been investigated by dividing the whole data set into two sub-samples of different target excitation. Interestingly, the multiparticle production process becomes less chaotic as the target excitation increases.

1 Introduction

Large number of particles are created and distributed in different ways throughout the available phase space volume in every high energy collision. It is possible to see important features such as correlation and intermittency effect, as an indication that large fluctuations resulting from dynamical causes predominate in particle formation [1, 2]. The genuine multiparticle correlation originating from collective effects may lead to high multiplicity events with specific features, e.g., ring-like, pencil-like (jet) structures [3–5].

However, to reveal complete information about particle production mechanism, the fluctuations per event to be studied in addition to the fluctuations averaged over event sample. Previously in intermittency analysis [6] when considering vertically averaged horizontal moments, only spatial fluctuation was included. Conversely, only the event space fluctuations, that is, the variations from event to event are measured by horizontally averaged vertical moments. Hwa proposed a novel method, the method of erraticity analysis, to obtain further details about the fluctuation patterns of the produced particles in high energy heavy ion collisions [7–9] which captures both spatial as well as event space fluctuations simultaneously. Erraticity is therefore a technique that can identify chaoticity in production dynamics, clarifying on the intermittency origin. The erraticity analysis has been applied in multiparticle production in high energy interactions [7–9, 11–18], in classical chaos theory [10], phase transitions [19], heartbeats [20].

In this paper we intend to study chaotic behavior of produced particles in ^{16}O–AgBr interactions at 60 A GeV using the method of erraticity analysis. This paper is organised as follows. Details of experimental data and simulated events are given in Sects. 2 and 3 respectively. In Sect. 4, we described the method of erraticity analysis in detail. Results of the analysis are discussed in Sect. 5. Finally, Conclusions Sect. 6 highlights the findings.

2 Experimental data details

Tha data used here are taken from Illford G5 emulsion plates exposed to ^{16}O beam of energy 60 A GeV from CERN SPS [21]. Nuclear emulsion detector [22] has several advantages such as it offers extremely high spatial resolution allowing precise tracking of charged-particles. Also this detector records and permanently stores the information of charged-particles over the 4Π geometry which enables long-term observation and analysis of particle interactions in finer phase space bins. The details of scanning and measurement technique are given in [21].

For current analysis 250 events of ^{16}O–AgBr interactions at 60 A GeV have been chosen according to the following selection criteria:

[a] e-mail: mitalimon@gmail.com (corresponding author)

Published online: 01 November 2024

Study of Forward Backward Correlations in Small Collision Systems at the LHC Energies Using a Strongly Intensive Observable

Joyati Mondal[1],* Hirak Koley[1], Somnath Kar[1,2],† Argha Deb[1,3], and Mitali Mondal[1,3]
[1] *Nuclear and Particle Physics research centre, Department of Physics, Jadavpur University, Kolkata-700032, INDIA*
[2] *Department of Physics, Kolhan University, Chaibasa-833201, INDIA and*
[3] *School of Studies in Environmental Radiation & Archaeological Sciences, Department of Physics, Jadavpur University, Kolkata-700032, INDIA*

Introduction

Forward-backward (FB) correlation are considered to be powerful tool to study correlations and fluctuations between produced particles in high energy nuclear collisions carrying important information regarding the basics of particle production mechanism. Most challenging part of FB correlation study is to avoid volume fluctuations, i.e., event-by-event fluctuations of the number of the participating nucleons [1]. Though considering intensive observable like the sum of the absolute transverse momentum of particles within the observation windows reduces such contribution of volume fluctuations [2], our multiplicity-dependent summed-p_T correlation study [3] manifested that FB momentum correlation coefficient depends on the total number of charged particle produced in a pseudorapidity (η) bin. In our present work, hence, we have explored more sophisticated correlation observable Σ [4] to suppress the contribution of volume fluctuations. It has been confirmed [5] that the strongly intensive observable Σ does not depend on system volume nor system volume fluctuations and carries more clear information on the early dynamics of the high energy hadronic interactions compared to FB multiplicity and momentum correlations. The so-called strongly intensive quantity $\Sigma[N_f, N_b]$ based on the charged-particle multiplicities in forward (N_f) and backward (N_b) η windows is defined by the following formula:

$$\Sigma[N_f, N_b] = \frac{W_b\langle N_f\rangle + W_f\langle N_b\rangle - 2(\langle N_f N_b\rangle - \langle N_f\rangle\langle N_b\rangle)}{\langle N_f\rangle + \langle N_b\rangle}$$

Here, Forward (backward) scaled variance $W_{f(b)}$ is defined as:

$$W_{f(b)} = \frac{\langle {N_{f(b)}}^2\rangle - \langle N_{f(b)}\rangle^2}{\langle N_{f(b)}\rangle}$$

We have studied the behaviour of $\Sigma[N_f, N_b]$ as a function multiplicity bin width and distance between F and B window centers (η_{sep}) using EPOS3 [6] simulated pp events at $\sqrt{s} = 13$ TeV and pPb events at $\sqrt{s_{\rm NN}} = 5.02$ TeV with hydrodynamical evolution of particles.

Results and Discussions

Fig. 1 represents $\Sigma[N_f, N_b]$ variable as a function of multiplicity bin width i.e. Δ multiplicity for EPOS3 simulated pp events at $\sqrt{s} = 13$ TeV and pPb events at $\sqrt{s_{\rm NN}} = 5.02$ TeV. Identifying sharp multiplicity cuts we have converted pp and pPb events multiplicity distributions into percentile classes following ALICE centrality class determination method. We focused mainly on most central collisions i.e. high multiplicity events (0-10%). We increased multiplicity bin width from 2% to 10% around 5% for both pp and pPb event multiplicity classes. It is clear from the figure that with the increase of multiplicity bin width, $\Sigma[N_f, N_b]$ values remain almost unaffected for both pp and pPb events though the values of Σ are higher in case of pp events.
Fig. 2 exhibits the variation of $\Sigma[N_f, N_b]$ with η_{sep} for EPOS3 simulated pp events at $\sqrt{s} = 13$ TeV and pPb events at $\sqrt{s_{\rm NN}} = 5.02$ TeV. It is clearly visible that $\Sigma[N_f, N_b]$ values increase with the increase of η_{sep} for both pp

*Electronic address: joyati254@gmail.com
†Electronic address: somnathkar11@gmail.com